Population and single-cell based quantitative analysis of Protein Kinase D-mediated regulation of the cell cycle

Vorgelegt von

Sebastian Räth

aus Immenstadt

I hereby assure that I performed the present study independently without further help or other materials than stated.

Sebastian Räth

Stuttgart, 28th of June 2014

Table of contents

Abbreviations

°C	Degree Celsius
Aur-A	Aurorakinase A
BFA	Brefeldin A
BM	bone marrow
Cdc2	cell division cycle 2
CDK	cyclin-dependent Kinases
Cdt1	Chromatin licensing and DNA replication factor 1
CFU-F	colony-forming unit-fibroblast
CHK1	Checkpoint kinase 1
CtBP/BARS	C-terminal binding protein/brefeldin A adenosine diphosphate–ribosylated substrate
CXCR4	C-X-C chemokine receptor type 4
DAPI	4',6-diamidino-2-phenylindole
DLK1	delta-like 1 homolog
DMEM	Dulbecco's modified Eagle's medium
DMSO	dimethyl sulfoxide
DNA	deoxyribonucleic acid
ECL	enhanced chemiluminescence
EDTA	ethylene diamine tetraacetic acid
EGFP	enhanced green fluorescent protein
EGFR	epidermal growth factor receptor
ERK	extracellular signal-regulated kinase
EtOH	ethanol
Fabp	fatty-acid-binding protein
FBS	fetal bovine serum
FCS	fetal calf serum
FL	fluorescence
Fucci	Fluorescent ubiquitination-based cell cycle indicator
GAPDH	glyceraldehyde 3-phosphate dehydrogenase
GD2	ganglioside
GFP	green fluorescent protein
GM130	cis-Golgi matrix protein 130
GPCR	G-Protein coupled receptor
GPCR	G protein-coupled receptor
GRASP	Golgi reassembly and stacking protein
HA/TCP	hydroxyapatite/tricalcium phosphate
HLA	human leukocyte antigen
HSC	hematopoietic stem cell
IBMX	3-isobutyl-1-methylxanthine
Ibsp	Integrin-binding sialoprotein
IF	immunofluorescence
Ig	immunoglobulin
M	Mitosis
mAG	monomeric Azami Green
MAPK	mitogen-activated protein kinases
MAPK	mitogen- activated protein kinase
mBMSC	mouse bone marrow stromal cell

MEK	mitogen-activated protein kinase kinase
mg	milligram
MHC	Major Histocompatibility Complex
min	minutes
mKO	monomeric Kusabira Orange
ml	milliliter
mM	millimolar
mm	millimeter
mMSC	mouse mesenchymal stromal cells
MSC	Mesenchymal stromal cells
Myt1	Myelin transcription factor 1
N	normal
ng	nanogram
nM	Nanomolar
NOD-SCID	Non-Obese Diabetic-Severe Combined Immunodeficiency
NRK	normal rat kidney
P	passage
PBST	phosphate buffered saline tween
PD	population doubling
PDBU	phorbol 12,13-dibutyrate
PDGFR	platelet-derived growth factor receptor
Pen/Strep	Penicillin/Streptomycin
PFA	paraformaldehyde
PI	propidium iodide
PKC	Protein Kinase C
PKD	Protein Kinase D
PLK	polo-like kinase
PMA	phorbol 12-myristate 13-acetate
POD	peroxidase
qPCR	quantitative Polymerase Chain Reaction
RIN1	Ras-interacting protein
RNA	ribonucleic acid
ROS	reactive oxygen species
RSK	ribosomal s6 kinase
SDS	sodium dodecyl sulfate
SDS-PAGE	SDS polyacrylamide gel electrophoresis
SEM	standard error of the mean
Ser	Serine
siRNA	small-interfering RNA
s-phase	synthesis phase
TAE	Tris-Acetat-EDTA
TGF-β	transforming growth factor β
UC	Umbilical Cord
VRK1	vaccinia-related kinase
WB	Western Blot
WT	wild type
α-MEM	Alpha Minimum Essential Medium Eagle

Summary

The cell cycle consists of G1, G2, S, and M phase and is a tightly regulated process with various checkpoints to control order and length of the separate phases. A multitude of signal molecules and pathways are involved in this process. In cancer, cell cycle control is often changed and understanding of these changes may result in new therapeutic targets in the treatment of patients. Additionally, cell cycle control is of special interest in stem cells as important decisions of cell fate – to proliferate or to differentiate - are part of cell cycle control. The success of adult stem cell therapeutic applications is thus dependent on in-depth understanding of this regulation.

The Fluorescent ubiquitination-based cell cycle indicator (Fucci) is a sophisticated technology, which can easily determine G1 and/or S/G2/M phases of the cell cycle. The technology analyzes living cells in a spatio-temporal manner using fusion proteins consisting of two distinct cell cycle proteins fused to two fluorophores - a dual color scheme of orange and green. The aim of this thesis was to characterize the influence of Protein kinase D (PKD) using this technology in cells with adult stem cell characteristics and an established human cancer cell line.

At first, a characterization of primary human mesenchymal stromal cells (MSC) derived from umbilical cord (UC) and bone marrow (BM) was performed. Furthermore, murine bone marrow stromal cells (mBMSCs) were isolated and osteogenic differentiation was investigated in tissue culture and in vivo. Three out of seven independent cell isolates showed the ability to differentiate into osteocytes, adipocytes, and chondrocytes in vitro. In vitro multipotency of an established mBMSC line was maintained over 45 passages. The osteogenic differentiation of this cell line was confirmed by quantitative polymerase chain reaction (qPCR) analysis of specific markers such as osteocalcin and shown to be Runx2 dependent. Notably, the cell line, when transplanted subcutaneously into mice, possesses full skeletal stem cell characteristics in vivo in early and late passages, evident from bone tissue formation, induction of vascularization, and host derived hematopoiesis. This cell line provides, thus, a versatile tool to unravel the molecular mechanisms governing osteogenesis in vivo thereby aiding to improve current strategies in bone regenerative therapy. Consequently, multipotent mBMSC lines were established from transgenic Fucci mice.

Single cell analysis of cell cycle progression was performed in these Fucci-mBMSCs and Fucci transgenic human HeLa cells. Specifically, the influence of protein kinase D (PKD) and the RAF/MEK/ERK pathway on progression through S/G2/M phase was investigated in detail. Inhibition of PKD but not of MEK resulted in a delay in progression through S/G2/M phase in HeLa cells and mBMSCs. Furthermore, MAPK pathway activation was quantitatively assessed during the synchronous progression of HeLa cells through S/G2/M and successfully used to develop a quantitative mathematical model describing this pathway.

Taken together this study demonstrates the benefit of quantitative and single cell analysis in cells with stem cell characteristics and an established cell line to enlighten the role of PKD in cell cycle control and, on top of that, support the notion that PKD is a potential new target for cancer therapy.

Zusammenfassung

Der Zellzyklus ist ein streng regulierter Prozess, der aus vier verschiedenen Phasen, G1, S, G2 und M, besteht. Die Dauer und Abfolge dieser Phasen unterliegen verschiedenen Kontrollmechanismen. Eine Deregulation des Zellzyklus durch Verlust dieser Kontrollmechanismen kann zu einer unkontrollierten Zell-Vermehrung führen und damit grundlegend für eine maligne Transformation von Zellen sein. Die Identifizierung dieser Veränderungen in der Zellzyklusregulation von Tumorzellen kann daher neue Strategien für Therapieansätze in betroffenen Patienten aufzeigen. Die Zellzyklus-Regulation ist auch in der Stammzellforschung von besonderem Interesse, da der Erfolg von Therapieanwendungen mit adulten Stammzellen von einem grundlegenden Verständnis der Mechanismen, die über Proliferation und Differenzierung von Stammzellen entscheiden, abhängt. Das fluoreszierende, auf Ubiquitinierung basierende Zellzyklus Indikator System (Fucci) ist eine elegante Methode, mit deren Hilfe G1 und/oder S/G2/M Phasen des Zellzyklus mikroskopisch bestimmt werden können. Durch genetische Konstruktion von Fusionsproteinen bestehend aus zwei verschiedenen, spezifischen Zellzyklusproteinen und zwei fluoreszierenden Reporterproteinen – orange und grün- ist es möglich lebende Zellen kontinuierlich über einen längeren Zeitraum zu analysieren. In dieser Arbeit sollte die Funktion der Proteinkinase D (PKD) in der Zellzykluskontrolle mit Hilfe dieses Systems untersucht werden. Zur Untersuchung wurden zum einen Zellen mit adulten Stammzelleigenschaften und zum anderen eine etablierte humane Krebszelllinie verwendet.

Zu Beginn wurde in dieser Arbeit eine Charakterisierung von primären humanen mesenchymalen Stromazellen (MSC), die aus der Nabelschnur (UC) und dem Knochenmark (BM) gewonnen wurden, durchgeführt. Des Weiteren wurden Stromazellen aus dem Knochenmark der Maus (mBMSC) isoliert und die osteogene Differenzierung in vitro und in vivo untersucht. Drei von sieben unabhängigen Zellisolaten differenzierten in vitro zu Osteozyten, Adipozyten und Chondrozyten. Diese in vitro Multipotenz konnte in einer in dieser Arbeit etablierten mBMSC Zelllinie über 45 Passagen erhalten werden. Die osteogene Differenzierung dieser Zelllinie wurde durch den Nachweis der Genexpression des spezifischen Markers Osteocalcin bestätigt. Weiterhin wurde gezeigt, dass diese osteogene Differenzierung vom Transkriptionsfaktor Runx2 abhängig verläuft. Besonders

interessant macht diese Zelllinie, dass sie in vivo die Eigenschaften von mesenchymalen Stammzellen in frühen sowie späten Passagen besitzt: Nach subkutaner Transplantation in Mäuse, konnte die Differenzierung zu Knochengewebe, die Induktion von Vaskularisierung und Hämatopoese gezeigt werden. Diese Zelllinie kann deshalb als vielseitiges Werkzeug eingesetzt werden um die molekularen Zusammenhänge, die die Osteogenese kontrollieren besser zu verstehen und aktuelle Strategien in der Knochen-Regenerationstherapie zu verbessern.

Einzelzellanalysen der Zellzyklus-Progression wurden in Fucci-mBMSCs, die aus transgenen Fucci-Mäusen isoliert wurden, und in Fucci-HeLa Zellen durchgeführt. Im Detail wurde besonders der Einfluss von PKD und des RAF/MEK/ERK Signalweges auf die Dauer der S/G2/M Phase untersucht. Die Inhibition von PKD aber nicht die von MEK führte zu einer Verlängerung der S/G2/M Phase in HeLa Zellen und mBMSC. Des Weiteren wurde die Aktivierung des MAPK Signalwegs während des synchronen Durchlaufs von HeLa Zellen durch die S/G2/M Phase bestimmt. Diese Daten wurden benutzt, um ein mathematisches Modell, das diesen Signalweg beschreibt, zu erstellen.

Zusammenfassend zeigt diese Studie den Nutzen von quantitativer und Einzelzellanalyse in Zellen mit Stammzellcharakteristiken und etablierten Zelllinien, um die Rolle von PKD in der Zellzyklusregulation aufzuklären. Die hier erhaltenen Ergebnisse legen eine detailliertere, präklinische Untersuchung von PKD-Inhibitoren nahe, um deren potentiellen Einsatz in der Krebstherapie zu prüfen.

Introduction

1.1.   Cell cycle progression and Checkpoints

In tissue cells are constantly exposed to signals that either favour division or cell death. In order to successfully duplicate, numerous processes have to be controlled in a tight spatio-temporal manner. Progression through the different phases of cell cycle is regulated by cyclin-dependent kinases (CDKs) (Morgan 1995). The activity of CDKs is controlled by cyclins and CDK inhibitors, by phosphorylation or ubiquitin-mediated degradation. To ensure that a cell only executes important steps in cell cycle if the preconditions are correct checkpoint pathways exist. The first checkpoint to be identified was the DNA damage checkpoint. Hartwell and Weinert found out, that radiation sensitive mutants of budding yeast stopped dividing until the damage was repaired. In contrast mutations in the cell cycle checkpoint gene *RAD9* permitted the radiation damaged cells to progress through division and cells consequently died (Hartwell & Weinert 1989). Later it was found that double-stranded breaks and blocked DNA replication, for example by thymidine dimers, are sensed by ATM and ATR kinases. These kinases phosphorylate a number of substrates that function in DNA repair, apoptotic death and cell cycle arrest, for example p53 (reviewed in Novák et al. 2003). The eukaryotic cell cycle is mainly controlled by three checkpoints at the G1/S boundary, the G2/M boundary and the metaphase/anaphase boundary (see Figure 1).
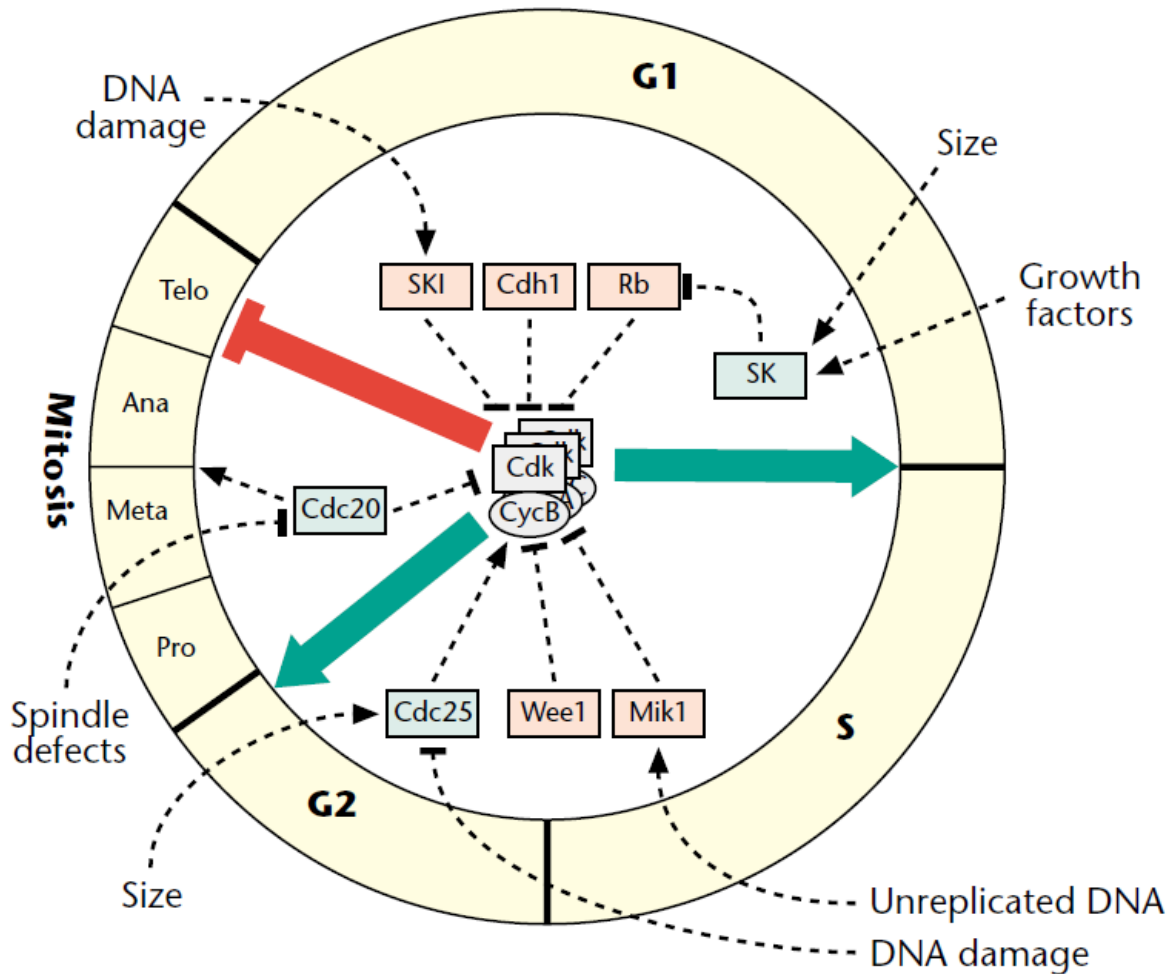
Figure 1 The cell cycle and its checkpoints
Accelerators (green) and brakes (red) of the cell cycle engine. Checkpoint pathways (dashed lines) modulate the activities of the accelerators and brakes. Pro, prophase; Meta, metaphase; Ana, anaphase; Telo, telophase; CKI, cyclin kinase inhibitor; DNA, deoxyribonucleic acid; Rb, retinoblastoma protein; Sk, starter kinase. Source: (Novák et al. 2003)

If the conditions for progression through these phases are not met, the cell cycle can be stopped at these checkpoints. During G1 the cells examine whether conditions are in favour of proliferation and their genome is ready to be replicated. At the G2/M boundary cells prove that the chromosome is fully replicated and undamaged. Metaphase to anaphase transition only starts when all chromosomes are attached to mitotic spindles securing successful separation of sister chromatids. Thus, to successfully divide, a cell needs to ensure DNA integrity, correct DNA duplication and segregation during anaphase. However, successful cell reproduction requires duplication and segregation (inheritance) of all cellular contents, including not only the genome but also intracellular organelles (Imoto et al. 2011). One organelle that is

in close relationship to nuclear functions is the Golgi apparatus. To successfully split it to the future daughter cells, the Golgi has to be fragmented in G2 phase. If this fragmentation does not take place progression through the cell cycle is halted comparably to the stop following incomplete DNA duplication (Sütterlin et al. 2002). This checkpoint was thus defined as Golgi mitotic checkpoint. Thus, additionally to checkpoint strategies to protect DNA integrity other control mechanisms exists in cells to protect integrity of intracellular organelles during cell division.

Several proteins play an important role in successful Golgi fragmentation and hence distribution of the Golgi stacks to the daughter cells. GRASP65, originally characterized as an adaptor protein capable of linking Golgi matrix proteins and transmembrane cargo proteins (Barr et al. 2001), is one of these proteins. Following microinjection of antibodies specific for GRASP65 into normal rat kidney (NRK) cells, a delay in Golgi fragmentation and subsequent entry into mitosis was observed (Sütterlin et al. 2002). GRASP65 is the major Golgi phosphoprotein in mitosis (Barr et al. 1997), and was found to be phosphorylated on multiple sites by Cdk1–cyclin B and the polo-like kinase 1 (Plk1) (Wang et al. 2003). More recently it was suggested that Cdk1–cyclin B is the major kinase phosphorylating GRASP65 in mitosis, and that phosphorylated GRASP65 interacts with the polo box domain of Plk1. Interestingly, expression of the wild type GRASP65 C-terminus but not the phosphorylation defective mutant, in which four consensus sites that are normally phosphorylated by Cdk1–cyclin B in mitosis were mutated to alanine, caused a delay. This led to the assumption that GRASP65 C-terminus ability to alter passage through mitosis may be a specific effect due to its influence on Plk1 function on mitotic Golgi fragments (Preisinger et al. 2005). In summary manipulating GRASP65 was shown to delay mitotic progression.

Another protein involved in Golgi fragmentation during mitosis is CtBP/BARS (C-terminal binding protein/brefeldin A adenosine diphosphate–ribosylated substrate). It was shown that CtBP/BARS (BARS) is required for G2/M transition by fission of interstack connecting tubules within the Golgi ribbon (Colanzi et al. 2007). Removing BARS resulted in a complete stop at the boarder of G2/M. Remarkably, cells without a Golgi ribbon are independent of BARS to complete Golgi fragmentation and mitotic entrance. Hence fibroblasts from BARS-knockout embryos possess a Golgi complex divided into isolated stacks at all cell-cycle stages, bypassing the need for BARS for Golgi fragmentation (Colanzi et al. 2007). In summary, during G2, the activity of

BARS, the GRASPs and MEK1 are required to convert the ribbon structure into isolated stacks, and the recruitment of Aur‑A to the centrosome gives the "green light" for entry into mitosis (see Figure 2A & B). Conversely, prevention of the severing of the ribbon in G2 inhibits Aur‑A recruitment and entry into mitosis. At the onset of mitosis (prophase), the isolated Golgi stacks undergo further disassembly (see Figure 2C). At metaphase, the Golgi membranes appear finely dispersed (as a "haze") through the action of Plk1 and Cdk1, which phosphorylate the golgins (GM130), and proteins involved in membrane fusion (p47); the mitotic spindle segregates proteins involved in ribbon formation (see Figure 2D) (reviewed in Corda et al. 2012).
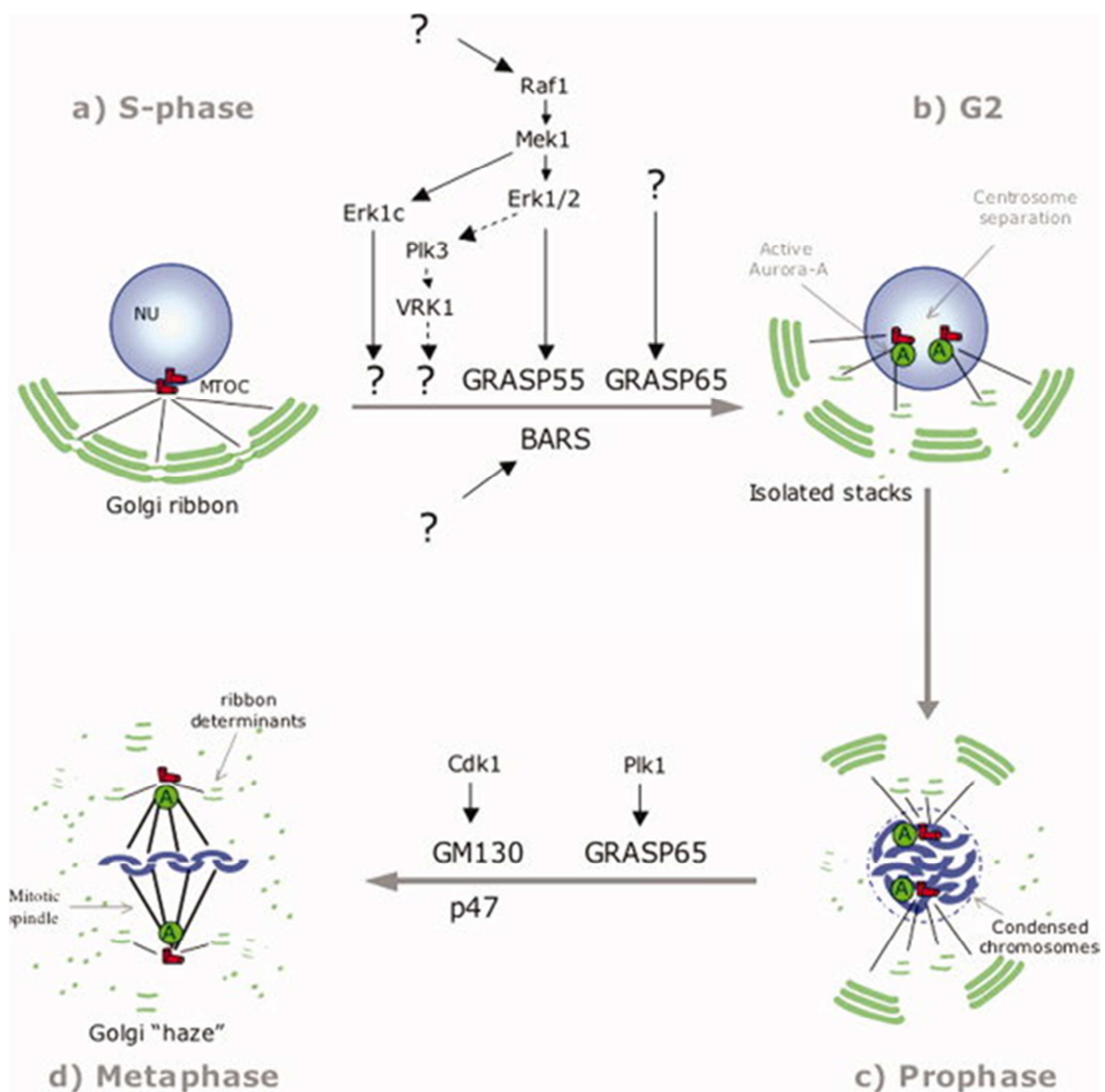
Figure 2 Sequential fragmentation of the Golgi ribbon during mitosis
Scheme of the partitioning of the Golgi complex during mitosis. For details see text (Corda et al. 2012).

Thus regulation of mitotic Golgi fragmentation seems to be a multi-step process starting with the fission of the interstack connecting tubules followed by the fragmentation of the Golgi stacks at later stages.

Upstream of MEK and RAF, progression through this checkpoint was also identified to be dependent on Protein Kinase D (PKD) (Kienzle et al. 2013).

1.2. Protein Kinase D and the MAPK pathway in cell cycle regulation

The Protein Kinase D (PKD) family of serine/threonine kinases consists of three isoforms, PKD1, PKD2, and PKD3. All three members exhibit high structure homologies among each other. PKD proteins are expressed in different cell types regulating various signalling pathways. PKD shows only low activity in basal state and thus PKD isoforms have to be activated to exert their function properly. PKD can be activated by different mechanisms with the most prominent being the PKC-PKD signalling cascade (Rozengurt et al. 2005). PKD signalling plays a role in multiple signal pathways involved in various biological functions such as proliferation, differentiation, apoptosis, immune responses, oxidative stress responses or secretion (see Figure 3).
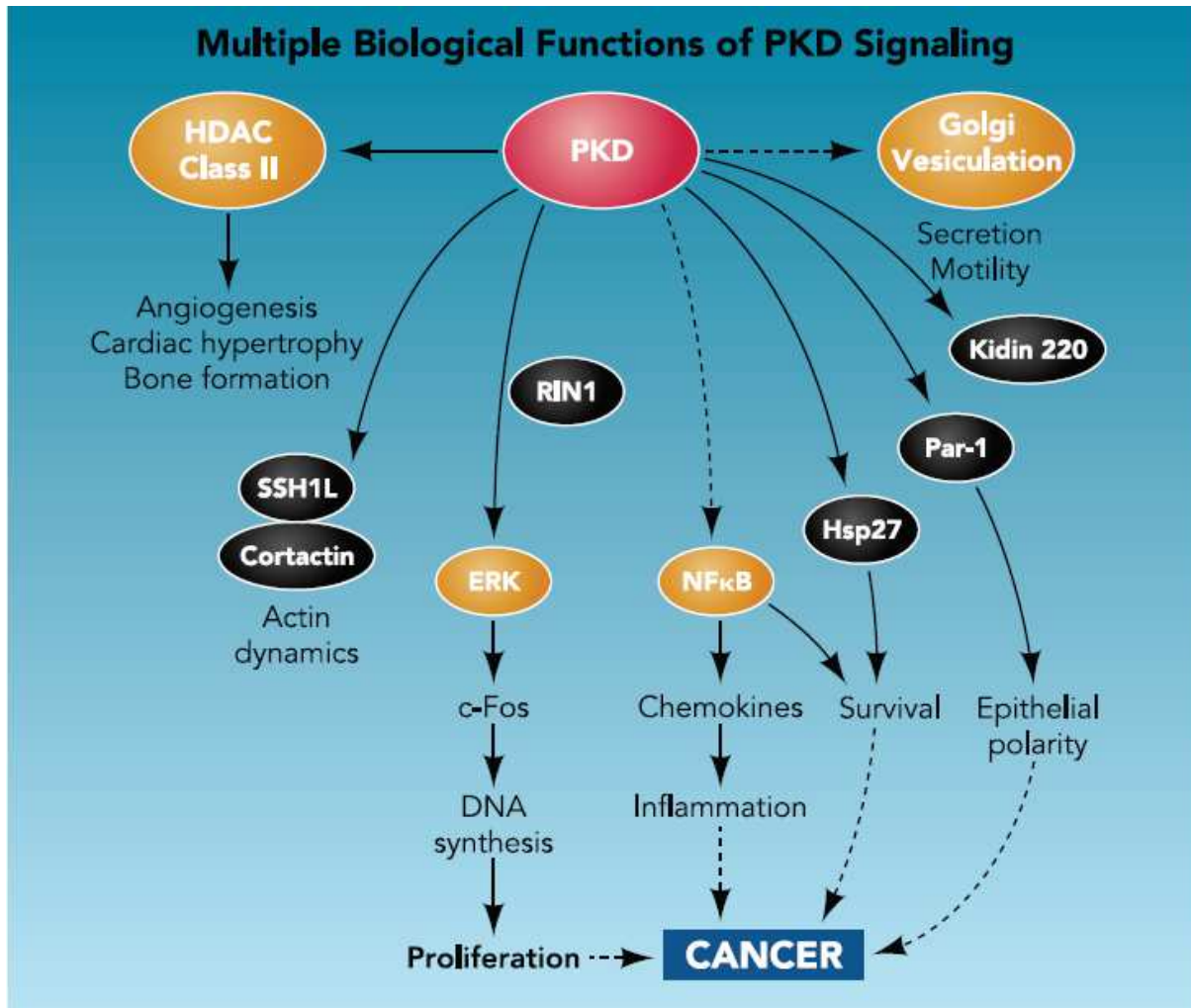
Figure 3 Multiple biological functions of PKD signalling
Active PKD phosphorylates a variety of cellular targets at specific sites, thereby regulating its subcellular localization (as in FIGURE 3) or activity (see Table 1 for examples of substrates and of the consensus sequence phosphorylated by PKD). Solid lines indicate direct phosphorylation of substrates (in light blue). Broken lines represent processes in which PKD is implicated but the sequence of molecular events has not been elucidated. Source: (Rozengurt 2011)

Several lines of evidence suggest a role for PKD in cell proliferation: In fibroblasts PKD1 was activated by multiple growth-promoting GPCR agonists that act through Gq, G12, and Gi, suggesting that PKD functions in mediating mitogenic signalling (Rozengurt 2011). Accordingly it was shown that overexpression of either PKD1 or PKD2 potentiated DNA synthesis and cell proliferation induced by Gq-coupled receptor agonists in Swiss 3T3 fibroblasts (Sinnett-Smith et al. 2009). In line with this, siRNA-mediated depletion of PKD1 markedly attenuated GPCR-induced mitogenesis (Sinnett-Smith et al. 2009). PKDs effect in mitogenic signalling may be explained by its ability to increase the duration of MEK/ERK/RSK signalling in fibroblasts (Sinnett-Smith et al. 2004) and keratinocytes (Jadali & Ghazizadeh 2010).

1.2.1.   PKD´s role in the Golgi mitotic checkpoint

The role of PKD in cell cycle control is only partially understood. PKD was shown to have an impact on MAPK pathway via RIN1, thereby regulating ERK activity (Sinnett-Smith et al. 2009). Moreover, it was shown that PKD isoforms are active during mitosis and located to the mitotic apparatus (Papazyan et al. 2008). Recently it was demonstrated, that PKD is crucial for the cleavage of the non-compact zones of Golgi membranes in G2. Depletion of PKD1 and PKD2 induced an accumulation of HeLa cells in G2. This accumulation was caused by the lack of Golgi fragmentation and hence a delay of the cells in the progression through the Golgi mitotic checkpoint. Importantly, the depletion of PKD1 and 2 blocked mitotic RAF and MEK activation, and as a consequence, mitotic Golgi fragmentation. This could be rescued by expression of active MEK1 (Kienzle et al. 2013).

1.2.2.   MAPK pathway in cell cycle regulation

The RAF/MEK/ERK cascade is a key pathway integrating diverse extracellular cues and is involved in mitogenic signalling. Upstream of MEK, RAF can activate very few partners other than MEK, and no other substrates for MEK than ERK have been found so far. Downstream of ERK, signalling cascades continue to flow, but no single downstream kinase can activate the wide variety of ERK substrates (Chambard et al. 2007). ERK and MEK are thus the key regulators because of their bottleneck function in this cascade. ERK activity needs to be elevated persistently during G1 phase to progress to S phase. Interestingly, not only ERK activity but also nuclear translocation of ERK is necessary. ERK activity and ERK-regulated transcription factors are in control of important requirements of cell cycle progression such as synthesis of pyrimidine, chromatin remodelling, ribosome synthesis, and protein translation (Chambard et al. 2007).

Additionally, ERK controls G1/S transition by regulating the transcriptional induction of cyclin D1 via Fos family members. ERK also regulates cyclin D1 transcription via myc and the assembly of cyclin/CDK complex (Chambard et al. 2007). At the transition of G2/M ERK participates in the nuclear translocation of cyclin B and blocks negative phosphorylation of Cdc2 by Myt1 via RSK kinase. However, the level of activation is critical, as a high activity of ERK was shown to negatively regulate G2-M transition via the kinases WEE1 and CHK1 (Yan et al. 2005). In conclusion ERK activity is a major regulator of G1-S transition and plays a dual role in G2-M transition.

The quantity of ERK activity is therefore important and may have opposing effects concerning cell cycle progression. Accordingly, inhibition of the EGFR reduced the frequency of ERK activity pulses, whereas inhibition of MEK resulted in a reduction of ERK activity amplitude. Remarkably, a reduction of the resulting ERK activity of over 90% is necessary to effectively silence proliferation in multiple cell lines (Albeck et al. 2013).

Apart from a critical function during G1, MEK was also shown to participate in the regulation of the Golgi mitotic checkpoint in G2. Loss of MEK1 activity prevented Golgi fragmentation in HeLa cells and caused a delay (Feinstein & Linstedt 2007). Of note, it was shown that MEK1b, an alternatively spliced form of MEK1, activates ERK1c, an alternatively spliced form of ERK1. These spliced forms were shown to be active during mitosis and enhanced Golgi fragmentation and mitotic rate (Shaul et al. 2009). Downstream of MEK, ERK1/2, the best characterized MEK1 substrate, controls mitotic Golgi breakdown through phosphorylation of GRASP55 (Feinstein & Linstedt 2008). Several other downstream effectors of MEK such as Plk3 via VRK1 have been proposed. Their targets and specific contributions to Golgi fragmentation remain to be determined (reviewed in (Colanzi & Sütterlin 2013).

1.3. Fucci – a tool to investigate the cell cycle in primary MSC

The dynamic nature of cell cycle progression and regulation requires an experimental system that allows the dynamic monitoring of cell cycle stages at a single cell level.

1.3.1. Fluorescent Ubiquitination-based Cell Cycle Indicator

The **F**luorescent **u**biquitination-based **c**ell **c**ycle **i**ndicator (Fucci) was first generated by Sakauwe-Sawano and colleagues (Sakaue-Sawano et al. 2008). The Fucci system exploits the regulation of cell cycle dependent ubiquitination. In the Fucci technique, cells are genetically modified to express the G1 marker Cdt1 and the S/G2/M marker Geminin fused to orange and green fluorescent tags, respectively. In the original version these tags were a fast-folding variant of mKO (monomeric version of Kusabira Orange) named mKO2 fused to Cdt1 and the monomeric version of Azami Green (mAG) fused to Geminin. As a result, actively replicating cell nuclei in

S/G2/M phases exhibit green fluorescence, nuclei directly after mitosis are non-fluorescent, while cells that enter G1 and not yet actively dividing display an orange fluorescence in the nucleus. Cells and transgenic mice constitutively expressing the cell cycle probes (Sakaue-Sawano et al. 2008), were successfully generated. Recently, the same group described a new Fucci derivative, Fucci2, in which red and yellowish green fluorescent tags, mCherry and mVenus, substituted for mKO2 and mAG in the original Fucci constructs to generate mCherry-hCdt1(30/120) and mVenus-hGem(1/110), respectively. The authors reasoned that this particular combination of fluorophores provides better colour contrast than that of Fucci. Additionally, they stated that the widely used fluorophore enhanced GFP (EGFP) can be spectrally separated from the Fucci2 fluorophores. This will facilitate imaging experiments in which cell cycle progression is monitored in parallel with protein subcellular localization and/or signalling events (Sakaue-Sawano et al. 2011). Using the Fucci2 system it is possible to generate time lapse imaging movies with continuous read-out on single cell level. Cell tracking provides in-depth information about the behaviour of heterogeneous cell population, single cells and allows characterization of subpopulations.

Possible applications of the Fucci system reach from drug testing in heterogeneous cancer cell populations to the identification of developmental processes and to the investigation of stem cell populations. In stem cells research single cell analysis already profoundly increased the understanding of cell fate choices and their molecular control in complex and dynamic cell systems. Eilken and colleagues could show for the first time that embryonic endothelial cells are the first hematopoietic cells in mammalian embryos by continuous long-term single-cell observation of mouse mesodermal cells (Eilken et al. 2009). By imaging hematopoietic stem cells Wu and colleagues identified that the balance of symmetric and asymmetric divisions in hematopoietic precursors are regulated by the microenvironment and subverted by oncogenes (Wu et al. 2007). Single cell analysis also provided insight into the regulation of a newly discovered adult stem cell subset in the central nervous system. Ravin and colleagues showed how discrete cell types emerge from single multipotent central nervous system stem cells and identify factors involved in this process (Ravin et al. 2008).

Similar insights may be gained in the subset of mesenchymal stem cells (MSC) in the near future. First approaches used a combination of several fluorescently labelled

marker proteins to specifically distinct between hMSC and osteoblasts on the single cell level (Schieker et al. 2007). Others showed, that in vivo homing of MSC is improved by single cell analysis controlling safety and efficacy of transplanted MSC (Phillips et al. 2012).

1.3.2. Mesenchymal stem cells

The understanding of cell cycle progression and regulation is important to find new insights concerning treatment strategies in various diseases. One field with great promises in medicine is the stem cell field. Multiple adult stem cell subsets exist. The earliest adult stem cell described is the hematopoietic stem cell (HSC). Side by side work in clinic and research laboratories led to the use of HSCs for treatment of fatal diseases and, moreover, as a curative option for individuals born with inherited disorders that carry limited life expectancy and poor quality of life (de la Morena & Gatti 2011).

human MSC

Mesenchymal stem cells (MSC) were first described by Friedenstein et al. as bone marrow stromal stem cells (BMSC). They discovered, that a small subset of cells in bone marrow (BM), characterized by rapid plastic adherence and a fibroblast like shape, is responsible for the osteogenic potential (Friedenstein & Lalykina 1970; Owen & Friedenstein 1988). MSC are able to proliferate for a certain time and differentiate into multiple cell types, such as osteocytes, adipocytes and chondrocytes, in vitro. The understanding of MSC was extended by a study demonstrating that in vivo transplantation of progenitor cells is the standard assay for confirming their multipotency and self-renewal, the two hallmarks of stem cells (Sacchetti et al. 2007). Despite some advancement, for example the suggestion of a stem cell niche together with HSCs (Méndez-Ferrer et al. 2010), the precise physiological role of MSC in maintenance and repair of peripheral tissue still remains elusive.

However, due to their multipotent character MSC increasingly became the focus of regenerative medicine during the last years. The ability of MSC to migrate to the site of injury in animal models (Uccelli et al. 2007), combined with their differentiation potential, made them a promising research object for tissue regeneration. Some

advances in treatment of osteogenesis imperfecta (Horwitz et al. 1999; Horwitz et al. 2002) were as attributed to cell replacement and long term engraftment of the transplanted MSC´s. Later on it was shown that the beneficial effect of MSC was a result of their paracrine activity on the injured site (Javazon et al. 2004; Bernardo et al. 2009; Caplan 2007). Still, the actual mechanism of action is not completely clear. However, several studies have shown positive effects on animal disease models, such as ameliorated diabetes and kidney disease in streptozotocin induced diabetes mice (Lee et al. 2006), stimulated glomerular healing in rats with glomerulonephritis (Kunter et al. 2006) and a protection against bleomycin-induced injury in murine lungs (Ortiz et al. 2007). Furthermore, MSC had certain immunosuppressive effects on the host immune system (Bernardo et al. 2009) and could therefore be used in the treatment of autoimmune diseases and rejection reactions after transplantation (Uccelli et al. 2007). In line with this, it could be shown that MSCs prolonged skin graft survival in baboons (Bartholomew et al. 2002), promoted engraftment in NOD-SCID mice (Noort et al. 2002; in't Anker et al. 2003) and prevented graft-versus-host disease in mice (Yañez et al. 2006).

The immunogenic capacities and consequences on the hosts immune system, of transplanted MSC themselves, on the other hand, are still discussed controversially. MSC have been considered as cells that are immune privileged and could be potentially ignored by the immune system. However, it has been demonstrated that allogeneic MSC were rejected by a MHC-mismatched host mouse. The infusion of syngeneic host-derived MSC on the contrary, resulted in enhanced engraftment of allogeneic stem cells (Nauta et al. 2006).

Hence it is no surprise, that the scope of potential clinical indications for MSC-based therapy is currently under heavy debate (Bianco, Cao, et al. 2013; Pittenger 2013; Phinney et al. 2013; Fibbe et al. 2013). In particular, despite a few promising reports of clinical benefits of MSC therapy, controlled clinical studies so far trail behind high flying expectations (Bianco, Cao, et al. 2013; Bianco, Barker, et al. 2013). Thus, in-depth understanding of stem cell biology and particularly of cell cycle control is needed to further exploit MSC's clinical potential.

mouse MSC

Because of the ability to manipulate their genome, mice would be an excellent choice to study MSC-related biological questions. However, the progenitor cell frequency in mouse bone marrow is extremely low and has been estimated to be only 0.001 – 0.0001%. Additionally, differences with respect to yield and growth kinetics among different mouse strains were reported (Peister et al. 2004; Phinney et al. 1999) making the isolation of murine BMSCs still challenging. A particular problem is that isolates of BMSCs are often contaminated with hematopoietic cells of the myeloid/macrophage lineage, which adhere on top of the stromal cells (Kuznetsov & Gehron Robey 1996). Due to these difficulties efforts to take advantage of existing mouse models to study fundamental aspects of MSC biology are still hampered.

Furthermore, general in vitro properties are not clear at present for mMSC. Basic questions in mMSC biology, as for example proliferative capacity, are discussed controversially. For example, there are conflicting reports about the ex vivo expansion capacity. Some groups were able to cultivate mMSC till very high passage numbers without chromosomal aberrations (Böhrnsen et al. 2009). In contrast, Josse et al found systematic chromosomal aberrations in murine MSC from different strains upon cultivation (Josse et al. 2010). Another aspect of proliferation, the ability of mMSC to grow density independent, remains unclear, too. Bianco et al claim the density-independent growing to be an important characteristic for stem cells (Bianco et al. 2008), whereas Peister et al. published increasing proliferation rates at fewer cells per square centimetre (5 cells/cm^2) for mMSC (Peister et al. 2004). In contrast to that Hsiao and Nadri were using high seeding densities in low passages to cultivate mMSC (Soleimani & Nadri 2009; Hsiao et al. 2010).

The second basic characteristic of stem cells, the differentiation potential is also not clearly defined for mMSC. Friedenstein et al convincingly showed that MSC were able to differentiate into osteoblasts, adipocytes and chondrocytes in vitro. However, some reports showing transgermal potential (Beltrami et al. 2007; Jiang et al. 2002) are reviewed critically (Bianco et al. 2008). Therefore, basic properties and questions of defining mMSCs remain to be comprehensively analyzed and answered. To address these questions a more standardized cellular system with clearly defined cell line characteristics would be helpful.

1.3.3. Fucci2-HeLa cell line

In biomedical sciences a very prominent human cell line is HeLa. HeLa cells were originally obtained from the cervical tumour of a female patient in 1951. The cell line showed remarkably high proliferation rate and durability during in vitro cell culture. Up to date, HeLa is the most commonly used cell line in research. Due to its robust proliferative capacity during in vitro culture and sometimes lack of stringent controls in tissue culture units, it contaminated a lot of other cell lines in different laboratories (Capes-Davis et al. 2010). Nonetheless a lot of important scientific results were obtained with this cell line. For example, HeLa cells were used by Jonas Salk to test the first polio vaccine in the 1950s. High cell numbers necessary for the test could be easily reached with HeLa cells (SCHERER et al. 1953). In 2009 60.000 papers about research performed with HeLa cells were published and as much as 300 new articles every month were added (Skloot 2010). It is thus logical, that Sakaue-Sawano and colleagues generated HeLa cells stably expressing the enhanced Fucci2 constructs, merging the highly proliferative potential of this commonly used cell line with a sophisticated tool to analyze the cell cycle continuously and on single cell level. The fused cyclins are Cdt1 and Geminin as described in the original Fucci system (see 1.3.1). The fluorescent proteins used in Fucci2 are Venus and mCherry. The two fluorophores are brighter and more compatible with other dyes (Sakaue-Sawano et al. 2011). The capabilities of these cells enable live-cell imaging and continuous single cell analysis of the resulting images.

1.4. Goals

Analyzing the regulators involved in cell cycle progression is important to understand diseases like cancer. Moreover increased understanding of cell cycle regulation is also vital to improve strategies for cell based therapies with adult stem cells. Controlling differentiation and the proliferative behaviour of these cells is the major safety issue to be solved. Despite promising results in animal models, the therapeutic efficacy of MSC so far is behind the expectations. The main reason for that is the high risk of using poorly characterized in vitro cultured cells in patients. In depth understanding of MSC biology, specifically of proliferation control and cell cycle regulation is necessary for developing safe therapeutically effective treatment strategies.

To establish proliferation and differentiation protocols, as part of this thesis, human MSC from umbilical cord (UC) and BM should be characterized in detail. In a next step, primary MSCs from wild type and Fucci mice should be isolated, characterized and used to study cell cycle progression under defined conditions. Particular attention should be paid to the role of PKD and its downstream signalling pathway, RAF/MEK/ERK, in MSC cell cycle progression. Additionally, experiments should be complemented using Fucci2-HeLa cells. The population and the single cell based data gained should be used to generate a mathematical model of proliferation and to reveal the impact of PKD and RAF/MEK/ERK on cell cycle progression in this model.

2. Materials and Methods

2.1. Materials

2.1.1. Instruments

Table 1: Instruments and company

Instrument	Company
Axiovert (standard light microscope)	Zeiss, Jena
Cell culture incubator	Binder, Tuttlingen
CellObserver: HS CellObserver inverse microscope, AxioCam HR 12 bit camera, Plan Apochromat 20×/0.8 M27 objective lense	Carl Zeiss MicroImaging GmbH, Jena, Germany
Centrifuge Heraeus Fresco 17	ThermoFisher Scientific, Waltham, MA, USA
Cytomics FC 500 (FACS)	Beckman Coulter, Krefeld
Electrophoresis: Mini-PROTEAN 3	Biorad, Munich
Eppendorf centrifuge 5415 R	Eppendorf, Hamburg
EVOS fl inverted fluorescence microscope	AMG, Mill Creek, USA
FACSDiVa option – FACSVantage SE	BD Bioscience, Heidelberg
Film Developing Machine Agfa Curic 60	Agfa, Düsseldorf, Germany
iBlot Gel Transfer Device	Invitrogen, Karlsruhe
Incubator	Varolab, Giesen
Labofuge 400R	Heraeus Instruments, Hanau
Laminar flow	NuAire, Plymouth, UK
LSM 710 (confocal laser scanning microscope)	Zeiss, Jena
MACS Quant Analyzer	Miltenyi Biotec, Bergisch-Gladbach
Microplate reader	TECAN INFINITE, Männedorf / Switzerland
Minitron incubator	Infors, Einsbach
Multiskan FC reader	ThermoFisher Scientific, Waltham, MA, USA
NanoDrop spectrometer	ThermoFisher Scientific, Waltham, MA, USA
NanoDrop® ND-1000 (Spectrophotometer)	peQLab, Erlangen
Nanophotometer	Implen, Munich
Neubauer counting chamber	Multimed, Kirchheim
Nucleofector™ II Device,	Lonza, Verviers, Belgium
Odyssey Reader	Li-Cor Biosiences, Lincoln, USA
pH meter FiveEasy	Mettler Toledo, Giessen
pipettes (1 - 20 µl / 20 - 200 µl / 200 - 1000 µl)	Eppendorf, Hamburg
Power Supply EPS-300	Amersham Pharmica Biotech, Freiburg
Quantitative PCR Cfx96	Biorad, Munich
Rotanta 460R (low speed centrifuge)	Multimed (Hettich), Kirchheim
Sonopuls HD 200 (sonyfier)	Bandelin, Berlin
Sterile bench Flow V	Varolab, Giessen
Thermocycler TC-512	Biostep GmbH, Jahnsdorf
Vortex Genie 2	Scientific Industries, Bohemia, USA
Vortexer444-1372	VWR International, Bruchsal
Water Bath WNB 10	Memmert, Schwabach
Water Purification Milli-Q Reference	Millipore, Schwalbach

2.1.2. Consumables

Table 2: Consumables and company

Consumable	Company
NuPAGE® Novex® 4-12% Bis-Tris Protein Gels	Novex, Life Technologies
0.2 µm filter	Sarstedt, Nümbrecht

24-gauge needle Sterican	Braun, Wertheim
Blotting Paper, 3MM	Whatmann, Schleicher Schuell, Dassel, Germany
blotting paper, type Whatman	A. Hartenstein, Würzburg
Cell culture flasks, plates and dishes	Greiner, Frickenhausen, Germany
Cellview Glass bottom Dish 30,0/10 MM, 4compartments	Greiner, Frickenhausen
Cryo vials 1ml	Greiner, Frickenhausen
falcon tubes	Greiner, Frickenhausen
glass coverslips 18 mm x 18 mm	Carl Roth GmbH & Co, Karlsruhe
iBlot® Transfer Stack, nitrocellulose, mini	Novex, Life Technologies
iBlot® Transfer Stack, nitrocellulose, regular size	Novex, Life Technologies
Medical X-ray film	CEA, Strangnas, Sweden
Nitrocellulose blotting membrane	Pall Corporation, Pensacola, USA
NuPAGE® Antioxidant	Life Technologies
NuPAGE® MES SDS Running Buffer (20X)	Life Technologies
NuPAGE® Transfer Buffer (20X)	Life Technologies
pipette tips	Greiner, Frickenhausen
qPCR plates MLL-9651	Biorad, Munich, Germany
reaction tubes	Eppendorf, Hamburg
replica dishes	Sterilin Limited, Newport, UK
serological pipettes	costar®, Corning Incorporated, New York, USA
syringe	BRAUN, Wertheim
universal fit filter tips	Corning Incorporated, New York, USA

2.1.3. Chemicals

Table 3: Chemicals and company

Chemical	Company
3, 3', 5, 5'-Tetramethylbenzidine (TMB)	BD Bioscience, Heidelberg
4-nitrophenyl phosphate disodium salt hexahydrate (4-NPP)	Sigma-Aldrich, Taufkirchen
Acetic acid	Carl Roth GmbH & Co., Karlsruhe
Acid sulphur (H_2SO_4)	Carl Roth GmbH & Co., Karlsruhe
Acrylamide (Rotiphorese Gel 30)	Carl Roth GmbH & Co., Karlsruhe
Adenosine-5'-triphosphate (ATP)	Sigma-Aldrich, Deisenhofen
Agar	Carl Roth GmbH & Co., Karlsruhe
Agarose	Carl Roth GmbH & Co., Karlsruhe
Ammonium persulfate (APS)	Carl Roth GmbH & Co., Karlsruhe
Blocking reagent	Roche Diagnostics, Mannheim
Bovine Serum Albumin (BSA)	Sigma-Aldrich, Deisenhofen
Bradford assay	Carl Roth GmbH & Co, Karlsruhe
Bromphenol blue	Serva, Heidelberg
Complete Protease Inhibitor Cocktail (EDTA free)	Roche Diagnostics, Mannheim
Coomassie brilliant blue R250	Carl-Roth GmBH & Co., Karlsruhe
Crystal violet	Merck, Darmstadt
Dimethyl sulfoxide (DMSO)	Carl Roth GmbH & Co, Karlsruhe
Dithiothreitol (DTT)	Carl Roth GmbH & Co, Karlsruhe
Ethanol	VWR, Darmstadt
Ethidium bromide	Roche Diagnostics, Basel, Switzerland
Ethylene diamine tetraacetic acid (EDTA)	Carl Roth GmbH & Co, Karlsruhe
Ethylene glycol tetraacetic acid (EGTA)	Carl Roth GmbH & Co, Karlsruhe
Fluoromount-G	Southern Biotech, Birmingham, USA
Gene Ruler 1 kb Ladder	MBI Fermentas, St. Leon-Rot
Glycerol	Carl-Roth GmbH & Co., Karlsruhe
Glycine	Carl Roth GmbH & Co, Karlsruhe
HEPES (4-(2-hydroxyethyl)-1- pipera-zineethanesulfonic acid)	Carl Roth GmbH & Co, Karlsruhe

Hoechst 33258 (bisbenzimide)	Sigma-Aldrich, Deisenhofen
HRP SuperSignal®West substrate dura	Pierce Biotechnology, Rockford, USA
HRP SuperSignal®West substrate pico	Pierce Biotechnology, Rockford, USA
Hydrochloric acid (HCl)	Carl Roth GmbH & Co, Karlsruhe
IBMX (3-Isobutyl-1-methylxanthine)	Sigma-Aldrich, Deisenhofen
Indomethacin	Sigma-Aldrich, Deisenhofen
Isopropanol	Carl Roth GmbH & Co., Karlsruhe
KCl	Carl Roth GmbH & Co., Karlsruhe
KH_2PO_4	Carl Roth GmbH & Co., Karlsruhe
Magnesium acetate	Sigma-Aldrich, Deisenhofen
Magnesium chloride ($MgCl_2$)	Carl Roth GmbH & Co., Karlsruhe
Magnesium chloride (MgCl2)	Sigma-Aldrich, Deisenhofen
Methanol	Carl Roth GmbH & Co., Karlsruhe
Mowiol® 4-88 (immunofluorescence mounting media)	Polysciences Europe GmbH, Ep-pelheim
N,N,N,N-Tetramethylethyldiamine (TEMED)	Carl Roth GmbH & Co, Karlsruhe
Na_2HPO_4	Carl Roth GmbH & Co., Karlsruhe
PageRuler prestained protein ladder	MBI Fermentas, St. Leon-Rot
Paraformaldehyde (PFA)	Carl Roth GmbH & Co, Karlsruhe
Peptone	Carl Roth GmbH & Co, Karlsruhe
Phosphatase Inhibitor Cocktail	Roche Diagnostics, Mannheim
Potassium acetate	Sigma-Aldrich, Deisenhofen
Potassium chloride (KCl)	Sigma-Aldrich, Deisenhofen
Prestained Protein Ladder	Sigma-Aldrich, Deisenhofen
Propidium iodide (PI)	Invitrogen, Karlsruhe
RNase A stock solution (20 mg/ml)	Invitrogen, Karlsruhe
Sodium azide	Sigma-Aldrich, Taufkirchen
Sodium chloride (NaCl)	Carl Roth GmbH & Co, Karlsruhe
Sodium dodecyl sulfate (SDS)	Carl Roth GmbH & Co., Karlsruhe
Sodium hydroxide (NaOH)	Carl Roth GmbH & Co., Karlsruhe
Thimerosal	Carl Roth GmbH & Co, Karlsruhe
Thymidine	Sigma-Aldrich, Deisenhofen
Tris-hydroxymethyl-aminomethane (Tris)	Carl Roth GmbH & Co, Karlsruhe
Triton X-100	Carl Roth GmbH & Co, Karlsruhe
Trypan blue	Sigma-Aldrich, Deisenhofen
Tween-20	Carl Roth GmbH & Co., Karlsruhe
Tween-80	Carl Roth GmbH & Co., Karlsruhe
Uridine-5'-triphosphate(UTP)	GE Healthcare, München
$ZnCl_2$	Carl Roth GmbH & Co., Karlsruhe
β-Glycerophosphate	Sigma-Aldrich, Deisenhofen
β-Mercaptoethanol	Sigma-Aldrich, Deisenhofen

2.1.4. Buffers and solutions

Table 4: Buffers and solutions with their recipe

Buffer	Recipe
1% Alizarin red solution	100 mg alizarin red solved in 10 ml H_2O, pH adjusted to pH 6.4
Alcian blue solution	1% alcian blue in 0.1 N HCl; pH 1.0
Blocking solution (IF)	5% (v/v) FBS in PBS
Blocking solution (Western blot)	0.5% (v/v) blocking reagent, 0.05% (v/v) Tween-20
Blotting buffer	200 mM glycine, 25 mM Tris, 20% (v/v) methanol
Coomassie stain solution	40% (v/v) methanol, 10% (v/v) acetic acid, 0.1% (w/v) coomassie brilliant blue

Destain solution	10% (v/v) acetic acid 40% (v/v) methanol in H$_2$O
ECL homemade solution A: solution B: working solution:	250 µg/ml in 0.1M Tris-HCl, pH 8.6 1.1 mg/ml p-coumaric acid in DMSO solution A + 1:10 solution B + 30% (v/v) H$_2$O$_2$
Hemalaun solution	1 g hämatoxylin, 0.2 g NaIO3, 50 g aluminium potassium sulphate, 50 g chloral hydrate, 1 g citric acid, ddH$_2$O added to 1
Laemmli protein sample buffer (5x)	312.5 mM Tris, pH 6.8, 25% (v/v) glycerol, 10% (w/v) SDS, 0.05% (w/v) bromophenol blue 25% β-mercaptoethanol (for reducing, without for non-reducing)
Nuclear fast red solution	0.1% nuclear fast red in 5 % aluminum sulphate solution
Oilred-o solution	6 parts of 0.5 % oil red O solution solved in isopropanol with 4 parts dH2O
PBS (Phosphate Buffered Saline)	140 mM NaCl, 2.7 mM KCl, 8 mM Na$_2$HPO$_4$, 1.5 mM KH$_2$PO$_4$
PBST	0.05 % (v/v) Tween-20 in PBS
PI staining solution	474 µl PBS, 25 µl PI (1 mg/ml), 0,5 µl RNAase A (20 mg/ml)
SDS-PAGE running buffer	25 mM Tris pH 8.8, 192 mM glycine, 0.1% SDS
TAE (Tris-Acetat-EDTA), pH 8,0	40 mM Tris-acetate, 1 mM EDTA, pH 8.3

2.1.5. Primary Cells and Cell lines, reagents, cell culture

Table 5: primary cells and Cell lines

Cell line	Characteristics	Tissue	Source
Fucci2-HeLa	Adherent, expressing Cdt1-mCherry and Geminin-mVenus	Human cervix adenocarcinoma	Riken Institute, Japan
Fucci-MEF	Isolated MEFs from Fucci-mouse	Mouse embryo	Isolated by Dr Ellwanger
HeLa	Adherent	Human cervix adenocarcinoma	ATCC
HeLa-Tet On PKD1-WT-eGFP	Inducible expressing PKD1-WT-eGFP	Human cervix adenocarcinoma	
HeLa-Tet On PKD2-WT-eGFP	Inducible expressing PKD2-WT-eGFP	Human cervix adenocarcinoma	
Human BM-MSC	Primary MSC	Human bone marrow	Fraunhofer Institute, Stuttgart
Human UC-MSC*	Primary MSC	Human umbilical cord	University Hospital, Munich*
M2	Immortalized mBMSCs	Mouse bone marrow	
Fucci-BMSC	Immortalized mBMSCs	Mouse BM	

*kindly provided by Prof. Eissner (Interdisziplinäre Stammzellforschung, Klinikum der LMU, Großhadern)

Table 6: Cell culture reagents, medium and antibiotics

Reagent	Company
10 x Trypsin EDTA	Life Technologies, Darmstadt, Germany
Aphidicolin (DNA-Polymerase-Inhibitor)	Calbiochem, San Diego, USA
CID 755673 (PKD inhibitor)	Tocris Bioscience, Bristol, UK
Collagen R solution	Serva, Heidelberg
DMEM, RPMI 1640, OptiMEM	Life Technologies, Darmstadt, Germany
Doxycycline, HCl	Merck Biosciences, Darmstadt, Germany
FBS (HyClone)	Thermo Scientific, Karlsruhe
FCS (fetal calf serum)	PAA, Laboratories, Pasching, Austria
G418	Life Technologies, Darmstadt, Germany
Glucose (sterile)	Sigma-Aldrich, Taufkirchen, Germany
IST+1	Sigma-Aldrich, Taufkirchen, Germany
kbNB142-70 (PKD-Inhibitor)	Tocris Bioscience, Bristol, UK
Lipofectamine™ 2000	Life Technologies, Darmstadt, Germany
L-Prolin	Sigma-Aldrich, Taufkirchen, Germany
MSCGM-Medium	Lonza, Basel, Switzerland
Oligofectamine	Life Technologies, Darmstadt, Germany
PD 98059 (MEK inhibitor)	Cell Signaling, Frankfurt (Main)
Plus reagent	Life Technologies, Darmstadt, Germany
Pyruvat	Sigma-Aldrich, Taufkirchen, Germany
RNAiMAX	Life Technologies, Darmstadt, Germany
RO3306 (Cdk1-Inhibitor)	Tocris Bioscience, Bristol, UK
RPMI 1640	Invitrogen, Karlsruhe
Sodium selenite	Sigma-Aldrich, Taufkirchen, Germany
Sorafenib	Santa Cruz Biotechnology, Dallas, USA
TransIT-293 Transfection reagent	Mirus Bio, Madison, USA
TransIT-HeLaMONSTER®	Mirus Bio, Madison, USA
Trypan blue	Sigma-Aldrich, Taufkirchen, Germany
UO126 (MEK-Inhibitor)	Calbiochem, San Diego, USA
Versene	Life Technologies, Darmstadt, Germany

2.1.6. siRNAs, Primer and Plasmids

Primers for qPCR were ordered from Qiagen (Quanti-Tect Primer Assays).

Table 7: qPCR primers

miRNA	Primer assay ID for qPCR
DLK1	Mm_Dlk1_1_SG
Fabp	Mm_Fabp4_1_SG
GAPDH	Mm_Gapdh_3_SG
Integrin-binding-sialo-protein	Mm_Ibsp_1_SG
Osteocalcin	Mm_Bglap_1_SG
Osteopontin	Mm_Spp1_1_SG
PParɣ	Mm_Pparg_1_SG
Runx2	Mm_Runx2_1_SG

Table 8: siRNAs

siRNAs	Company
non-target plus smartpool control	Dharmacon
si ON-Targetplus SMART pool Mouse Runx2	12393, Dharmacon

Table 9: DNA plasmids

name	Reference
gPKDrep	(Fuchs et al. 2009)
PKDrep	(Czondor et al. 2009)

2.1.7. Antibodies

Table 10: Antibodies

Antibody	Specie	Dilution	Company
Alexa Fluor® 488 anti-mouse	Goat	1:500 (IF)	Invitrogen
Alexa Fluor® 546 anti-rabbit	Goat	1:500 (IF)	Invitrogen
Alexa Fluor® 633 anti-mouse	Goat	1:500 (IF)	Invitrogen
Alexa-488 labeled phalloidin	Goat	1:100 (IF)	Invitrogen
anti-ERK	Rabbit	1:2000 (WB)	Cell Signalling
anti-GAPDH	Rabbit	1:2500 (WB)	Sigma-Aldrich
anti-GFP	Mouse	1:2000 (WB) 1:300 (IF)	Roche
anti-giantin	Rabbit	1:100 (IF)	Abcam
anti-MEK	Rabbit	1:1000 (WB)	Cell Signalling
anti-mouse 800	Goat	1:15000 (WB)	Li-CoR
Anti-p53 (1C12)	Mouse	1:1000 (WB)	Cell Signalling
anti-phospho-ERK p44/42 (T2027204)	Rabbit	1:1000 (WB)	Cell Signalling
anti-phospho-Histone H3 (pSer10)	Rabbit	1:2000 (WB)	Sigma-Aldrich
anti-phospho-Histone H3 (pSer10)	Mouse	1:1000 (WB)	Cell Signalling
anti-phospho-MEK1/2 (S217/221)	Rabbit	1:1000 (WB) 1:50 (IF)	Cell Signalling
anti-phospho-PKD Ser744/748	Rabbit	1:2000 (WB)	Cell Signalling
anti-pPI4KIIIβ (Ser294)	Rabbit	1:1000 (WB) 1:300 (IF)	(Hausser et al. 2005)
anti-rabbit 690 LT	Goat	1:15000 (WB)	Li-COR
anti-tubulin-α Ab-2 (Clone DM1A)	Mouse	1:2000 (WB)	Thermo Scientific
POD-anti-mouse IgG (heavy & light chain)	Goat	1:10000 (WB)	Dianova
POD-anti-rabbit IgG (heavy & light chain)	Goat	1:10000 (WB)	Dianova

2.1.8. Kits

Table 11: Kits

Kit	Company
MSC Nucleofector Kit	Lonza
QuantiTect SYBR Green RT-PCR Kit	Qiagen
RNAeasy Kit	Qiagen
Senescence beta galactosidase staining kit	Cell Signalling

2.2. Methods

2.2.1. Culture of human bone-marrow (hBM-MSCs) and umbilical-cord derived stromal cells (hUC-MSCs)

Cells were cultured in MSCBM + 2% FCS (Lonza Cologne AG, Germany) and cultured at 37 °C in a 5% CO_2 humidified atmosphere. After reaching a confluency of 80%, cells were seeded at a density of 1000 cells/cm² into T-75 culture flasks (Greiner BioOne, Germany) for passaging.

2.2.2. Differentiation of hMSCs

Osteogenic medium for primary hMSCs consists of MSCBM medium (Lonza Cologne AG, Germany) containing 10 mM ß-glycerol phosphate, 50 µg/ml ascorbic acid 2-phosphate, 100 nM dexamethasone and 2% FCS (Lonza Cologne AG, Germany). Primary hMSCs were plated in 24-well plates (Greiner BioOne, Germany) and medium was changed every two days for 21 days. To analyze osteogenesis of hMSCs induced by osteogenic medium mineralization deposits were stained by alizarin red. Alizarin red staining was performed as stated in 2.2.8.1.

Adipogenic medium for primary hMSCs consists of DMEM High Glucose (4,5 g/l) supplemented with 10% FCS (Lonza Cologne AG, Germany), 1% Pen/Strep, 1 µM Dexamethasone, 500 µM IBMX, 1 µg/ml Insuline and 100 µM Indomethacin. Control medium for adipogenic differentiation consists of DMEM High Glucose (4,5 g/l) supplemented with 10% FCS (Lonza Cologne AG, Germany) and 1% Pen/Strep. Medium was replaced every 2-3 days. Adipogenic differentiation was analyzed by Oil red o staining after 13 days as stated in 2.2.8.2.

Chondrogenic medium for primary hMSCs consists of DMEM High Glucose (4,5 g/l) supplemented with 1% Penicillin/Streptomycin, 50 µg/ml l-ascorbic acid-2-phosphate, 100 nM dexamethasone, 100 µg/ml pyruvate, 40 µg/ml l-proline and 1% Insulin-transferrin-sodium selenite media supplement. TGF-β3 (10 ng/ml) was added with every medium change. The negative controls were cultured in chondrogenic differentiation medium without TGF-β. Chondrogenic differentiation and analysis was performed as stated in 2.2.8.3.

2.2.3. Isolation, culture, and maintenance of bone-marrow-derived stromal cells

Isolation of BMSC was performed as previously described (Soleimani & Nadri 2009). Briefly, C57BL6 mice were sacrificed using cervical dislocation and rinsed with 70% ethanol. The two tibias and femurs of each animal were cleaned of skin and transferred into alpha-MEM (Genaxxon) supplemented with 1% Pen/Strep. After removing the connective tissue in a sterile bench the ends of each bone were clipped off and the bone marrow was flushed out with a 26 G needle containing culture medium. The samples were stored on ice. Cells were separated with a 70 µm filter mesh followed by centrifugation (1000 g; 5 min) and resuspended in 1 ml of BMSC culture medium consisting of α-MEM medium (Genaxxon) supplemented with fetal calf serum (15%, Hyclone). 4×10^6 cells/cm^2 were plated (Greiner) and incubated at 37% and 5% CO_2 in a humidified incubator. The culture medium was replaced after 3, 8 and 16 hours. 72 hours after isolation, the cells were washed with phosphate buffered saline (PBS). Afterwards, the medium was changed every 2-3 days until the cells were 70% confluent. Cells were split using Versene plus 0.5% trypsin (Invitrogen) and cultured in a 25 cm^2 flask or a 6 cm culture dish (Greiner). Cells were maintained in culture medium for further studies and passaged at a confluence of 6700 cells/cm^2 every 2-3 days if not mentioned otherwise. The number of population doublings (PD) was calculated using the formula $PD = (\ln n_{ch} - \ln n_{cs})/\ln 2$, where n_{ch} is number of cells harvested and n_{cs} is number of cells seeded (Kurz et al. 2004).

2.2.4. Immunofluorescence and microscopy

BMSCs or Fucci2-HeLa were grown on collagen-coated coverslips, washed with PBS, fixed in 4% paraformaldehyde at room temperature for 15 min, washed, permeabilized with 0.1% Triton-X 100 (5 min, RT) and blocked with blocking buffer (5% FBS in PBS) for 30 min. The cells were incubated with for example with DAPI (1 µg/ml) for 15 min, washed, incubated for example with Alexa-488 labelled phalloidin diluted in blocking buffer for 1 hour, washed, mounted in Fluormount G (Southern Biotechnology, AL, USA) and analyzed using the Cellobserver (Zeiss, Germany). Cells were imaged with a Plan-Apochromat 20x/0.8 DIC objective lens.

Confocal images were taken using the LSM 710 (Zeiss). DAPI was excited at 405 nm using the diode laser, mAG was excited at 488 nm, and mKO2 was excited at 514 nm using a multiline argon laser. Alexa633 was excited at 633 nm using the Helium

neon laser. Images were taken with 40 or 63 times magnification (oil) in a 10 stack 4x4 tile scan. Pictures were analyzed using ZEN, Image J and Adobe Photoshop.

2.2.5. Beta-galactosidase staining

mBMSCs were stained with the senescence beta-galactosidase staining kit (Cell Signalling) according to manufacturer's guidelines. Briefly, cells were rinsed once with PBS. Then 1 ml of 1x fixative solution was added to each well. The cells were fixed for 10-15 minutes at room temperature. After that cells were rinsed two times with PBS. After that 1 ml of the beta-galactosidase staining solution was added to each well and incubated at 37°C overnight in a dry incubator. While the beta-galactosidase staining solution was still on the plate, images were taken at a light microscope to detect development of blue colour.

2.2.6. Propidium iodide staining

$1*10^6$ HeLa cells were seeded in 6 cm culture dishes. Cells were trypsinized, washed with cold PBS and resuspended in 1 ml of cold PBS. 1 ml of the cell suspension was then added to 9 ml 70% EtOH while vortexing to ensure minimal cell clumping. Cells were washed with PBS and resuspended in 500 µl PI-staining solution (474 µl PBS, 25 µl PI (1 mg/ml), 0,5 µl RNAase A (20 mg/ml). Cells in staining solution were incubated at 37°C for 30 minutes under light protection and measured afterwards.

2.2.7. Flow cytometry

Flow cytometry analysis of PI stained HeLa cells was performed using the MACS Quant Analyzer. MACS Quantify software was used to analyze fluorescence intensity. Linear gating between FL height and FL area ensured exclusion of clumped cells.

Flow cytometry analysis of mouse BMSC and human BM- and UC-MSC was performed by Georg Siegel and colleagues (Institute of Clinical and Experimental Transfusion Medicine (IKET), University Hospital Tübingen, Tübingen, Germany). Flow cytometry analysis of mMSC populations was performed at passage 8, passage 23 and passage 43 and for hMSC at passage 1-4 employing a FACScan instrument (BD Biosciences) and BD CellQuest Pro software. Cells were incubated with (secondary) PE-labeled mouse or human-specific antibodies (anti-CD4, -CD8a, -CD9,

-CD11b, -CD11c, -CD14, -CD29, -CD31, -CD43, -CD44, -CD45R, -CD71, -CD73, -CD80, -CD86, -CD90, -CD105, -CD106, -CD117, -CD135, -CD140a, -CD144, -CD184, -CD195, -H-2K/H2D, -IA/IE, -SCA1 and -VEGFR2 (BD Biosciences); -CD34 (Abd Serotec); -CD39 (R&D); -CD140b (Epitomics); -CD146 (Bio Legend) and -CD271 (STEMCELL Technologies)) for 60 min on ice. Unspecific antibody binding was prevented by using the Mouse BD Fc Block™ (BD Biosciences) according to the manufacturer's instructions. PE-conjugated or non-labeled IgG, IgG2aκ, IgG1κ, IgG1λ1, IgG2cκ, IgG2bκ, IgG2bκ and IgG1 antibodies (BD Biosciences) were used as isotype matched controls. As secondary antibodies mouse anti-rat Ig, donkey anti-goat IgG, goat anti-rat Ig, rat anti-mouse IgG2a+b (BD Biosciences) or goat anti-rabbit Ig (Biotrend) were used. Dead cells were excluded by uptake of 7-Aminoactinomycin D. Analysis of percentage of antigen positive cells and fluorescence intensity was performed using FlowJo software. The respective isotype control was subtracted from all samples to compensate unspecific antibody binding.

2.2.8. Differentiation of mBMSCs

2.2.8.1 Osteogenic differentiation

BMSCs were grown to 90-100% confluence in 24-well-plates and the culture medium was then replaced with osteogenic medium (α-MEM supplemented with 15% FCS plus 1% Penicillin/Streptomycin, 100 nM dexamethasone, 50 µg/ml ascorbate-2-phosphate, and 10 mM beta-glycerol phosphate). The medium was changed every 2-3 days. Osteogenic differentiation was assessed by Alizarin Red staining 21 days after initial osteogenic induction. In brief, cells were washed with PBS and allowed to dry for 5 to 10 min. Then cells were fixed with 50% ethanol for 20 min. The fixed cells were then stained with 1% Alizarin red (Roth) at pH 6.4 for 30 min under continuous shaking. Subsequently, cells were rinsed three times with H_2O, and transmitted light pictures were taken. As a negative control cells grown in culture medium for 21 days were used.

2.2.8.2 Adipogenic differentiation

BMSCs were grown to confluence on Permanox 4-well chamber slides (Thermo Scientific). Adipogenic differentiation medium (α-MEM supplemented with 15% FCS

plus 1% Penicillin/Streptomycin, 1 µM dexamethasone, 500 µM IBMX, 10 µg/ml human insulin and 100 µM indomethacin) was added and renewed every 2-3 days. 12 days after initial adipogenic induction cells were washed with PBS and fixed for 10 min in 4% Histofix (Roth). Then, cells were rinsed once with H_2O and incubated in 60% isopropanol for 5 min. Subsequently, the cells were incubated for 10 min with Oil Red O. Afterwards the cells were washed once with 60% isopropanol followed by H_2O. Nuclei were counterstained with hemalaun. As a negative control cells grown in culture medium for 12 days were used.

2.2.8.3 Chondrogenic differentiation

$2.5*10^5$ BMSC were centrifuged (1000 g; 5 min) in a 15 ml Falcon tube, the supernatant was discarded and 1 ml of chondrogenic differentiation medium (α-MEM plus 1% Penicillin/Streptomycin, 50 µg/ml l-ascorbic acid-2-phosphate, 100 nM dexamethasone, 100 µg/ml pyruvate, 40 µg/ml l-proline and 1% Insulin-transferrin-sodium selenite media supplement) was added to the cell pellet. TGF-β_3 (10 ng/ml) was added with every medium change. The negative controls were cultured in chondrogenic differentiation medium without TGF-β_3. Medium was changed twice a week for 27 days. After fixing the pellets for two hours in 4% Histofix (Roth), they were embedded in paraffin in cassettes using the automated system Shandon Citadel 1000 (Thermo Scientific). The cassettes with the pellets were transferred to a heating chamber at 60°C after the program of the automated system was finished. The melted paraffin was removed from the cassettes and the cell pellets were transferred into a metal form filled with liquid paraffin. The paraffin solidified on a cooling plate. The obtained solid paraffin block containing the pellet was then sliced with a rotary microtome RM 2145 (Leica).

The slices were deparaffinized using a descending sequence of xylol-ethanol. After 3 min in 0.1 N HCl the slices were stained with 1% Alcian Blue (Roth) dissolved in 0.1 N HCl (pH 1.0) for 30 min. Two washing steps 0.1 N HCl followed by H_2O, were performed to remove the unspecific bound dye. The slices were counterstained with nuclear fast red for 4 min. To dehydrate the pellet slice ascending concentrations of ethanol were used. Isomount (LABOnord) was used to fix the slices on the object slides.

2.2.9. Colony-forming-unit fibroblast assay

The proliferative induction capability of the M2 cell line was evaluated by colony-forming-unit fibroblast (CFU-F) analysis. M2 BMSCs were seeded into 100 cm^2 cell culture dishes at an initial density of three cells per cm2 in 12 ml medium. Cells were incubated for 7 days in a humidified 5% CO_2 incubator at 37°C. On day 7, cultures were simultaneously fixed and stained with 0.1% crystal violet in 20% methanol by incubating them at room temperature for 30 min and then washed twice with water. Crystal-violet stained colonies with a minimum surface area of 1 mm^2 were counted and then photographed. CFU-F frequency was calculated by dividing the number of colonies by the number of cells seeded. The experiment was performed in triplicates.

2.2.10.   Single clone analysis

BMSCs (P42) were seeded with a concentration of 0,5 cells/well in a 96-well plate in pre-conditioned sterile filtered α-MEM supplemented with 15% FCS. The wells were analyzed microscopically to record the single cell seeding events one day after plating. Single clone colonies were passaged after 17 days. 24 clones were analyzed for osteogenic and adipogenic differentiation.

2.2.11.   Nucleofection

BMSCs (P20-P24) were nucleofected with Amaxa nucleofection kit for MSC (Lonza) according to the manufacturer's instructions. Briefly, $5*10^5$ cells were resuspended in 100 µl nucleofector solution, 1 µM siRNA (ON-Targetplus SMART pool Mouse Runx2 (12393, Dharmacon) or the non-target plus smartpool control) was added and the cell suspension was transferred to a Nucleofector cuvette. Cells were nucleofected using program U23 of the Amaxxa Nucleofector (Lonza). Subsequently, the cell suspension was transferred into culture medium and incubated at 37°C and 5% CO_2. Successful knockdown was verified by qPCR two days post nucleofection.

2.2.12.   Quantitative real-time PCR

RNA was extracted using the RNeasy Kit (Qiagen) according to the manufacturer's instructions and concentration was measured using a NanoDrop (Peqlab). The

260/280 and 260/230 OD ratios were measured to assess the purity of RNA samples. One-step real-time RT-PCR was applied to quantitatively analyze mRNA levels. In brief, the reaction was performed on the CFX96 Touch qPCR System (BioRad) platform using QuantiTect SYBR Green RT-PCR Kit (Qiagen). The PCR mix contained 10 µl Quantitect SYBR Green PCR Mix, 0,2 µl reverse transcriptase, 2 µl of the respective QuantiTect Primer Assay consisting of a mixture of predesigned forward and reverse primer for the gene of interest and 100 ng RNA in 7,8 µl RNAse free H$_2$O. PCR was performed under the following conditions: 50°C for 30 min, 95°C for 15 min, followed by 40 cycles of 95°C for 30 s, 55°C for 30 s, 72°C for 30 s. A melt curve analysis step was added with a melting profile of 65.0°C to 95.0°C (Increment 0.5°C) Quanti-Tect Primer Assays (Qiagen) were used for Osteocalcin (Mm_Bglap_1_SG), Osteopontin (Mm_Spp1_1_SG), Integrin-binding-sialo-protein (Mm_Ibsp_1_SG), Runx2 (Mm_Runx2_1_SG), GAPDH (Mm_Gapdh_3_SG), PParɣ (Mm_Pparg_1_SG), Fabp (Mm_Fabp4_1_SG) and DLK1 (Mm_Dlk1_1_SG). The relative expression was calculated by normalization to GAPDH using the ΔCq or the ΔΔCq method.

2.2.13.   Western blot analysis

2.5*10^5 cells were harvested via the hot lysis method. Briefly, supernatants were aspirated and adherent cells lysed by addition of 300 µl of hot (95°C) laemmli buffer (125 mM tris (pH 6.8), 10% glycerol, 4% SDS, 0.02% bromophenol blue, 10% beta-mercapto-ethanol) followed by incubation at 95°C for further 10 min and sonication. Freshly prepared bone marrow cells (BM) were lysed by resuspension in 300 µl hot laemmli buffer. After centrifugation, supernatants were collected and 15 µl of each protein samples subjected to a 4-12% gradient Bis-Tris SDS-PAGE (Life Technologies) blotted onto nitrocellulose membranes and incubated with primary antibodies for example a p53-specific antibody (1C12; Cell Signalling). Equal loading was monitored by reprobing membranes with an antibody against actin or Tubulin (Sigma-Aldrich). HRP conjugated secondary antibodies were from Jackson Immunoresearch Laboratories. Bands were visualized applying chemiluminescence SuperSignal®detection system (PIERCE). Alternatively secondary infrared labelled antibodies (LiCor) were used. Bands were visualized using the Odyssey-Reader (Li-Cor). Bands were quantified using ImageJ.

2.2.14.   Anchorage-independent growth

1000 BMSCs were seeded in 50 µl of α-MEM supplemented with 15% FCS in the lid of a 100 mm culture dish. The lid was then inverted to create hanging drops. Images were captured with a 45 times magnification at a sz61 binocular (Olympus). The diameter of the spheres was monitored at day 3, 6, 8, 12, and 18.

2.2.15.   In vivo transplantation

The in vivo experiments with mBMSCs were performed by Dr Sacchetti (Department of Molecular Medicine, Sapienza University, Rome, Italy).

In order to assess the osteogenic potential of the M2 cell line in vivo, mBMSC M2 cell strains in early (P8-10) or late (P40-44) passages were seeded onto osteoconductive material (hydroxyapatite/tricalcium phosphate particles, HA/TCP) as reported previously (Kuznetsov et al. 1997; Krebsbach et al. 1997; Bianco et al. 1998). All animal procedures were approved by the relevant institutional committees. Briefly, $2x10^6$ cells were loaded onto hydroxyapatite/tricalcium phosphate particles (40 mg, 100–200 µm; Zimmer, Warsaw IN) and embedded in a fibrin gel to generate carrier-cell constructs. The constructs and the cell-free carrier, as control, were subcutaneously transplanted in the backs of 6-15 weeks-old female SCID/beige mice (CB17.Cg-Prkdcscid Lystbg/Crl; Charles River Laboratories International, Inc., Wilmington, MA). In brief, operations were performed under sterile conditions under anaesthesia achieved by intramuscular injection of a mixture of Zoletil 20 (Virbac, 5 µl/g of body weight) together with Rompun (Bayer, 1ml/ Zoletil 20 bottle). The mouse back was disinfected with betadine and midlongitudinal skin incisions of about 1 cm in length were made on the dorsal surface of each mouse. Subcutaneous pockets were formed by blunt dissection. A single transplant was placed into each pocket with up to four transplants per animal. The incisions were closed with surgical staples.

2.2.16.   Histology

Histology of M2 transplants was performed by Dr Sacchetti (Department of Molecular Medicine, Sapienza University, Rome, Italy).

Heterotopic transplants were harvested after 8 weeks, fixed in 4% formaldehyde, decalcified in 10% ethylenediaminetetraacetic acid at pH 7.2, and embedded in paraffin. Subsequently, the deparaffinized and rehydrated sections were stained with hematoxylin and eosin.

2.2.17.   Statistical analysis

Data are expressed as means ± SEM. A one-way ANOVA test followed by a Bonferroni posttest was used in statistical analysis for comparison, and $P < 0.05$ was used as the criterion for statistical significance.

2.2.18.   Synchronization of Fucci-BMSCs and Fucci2-HeLa cells

2.2.18.1 RO 3306

RO3306 is a selective CDK1 inhibitor that reversibly arrests proliferating human cells at the G2/M phase border (Vassilev 2006). Fucci-BMSCs were treated with RO3306 for 24 hours. Cells were released from synchronization by changing the medium to culture medium.

2.2.18.2 Aphidicolin block

Aphidicolin is a specific inhibitor of DNA polymerase in eukaryotic cells and can be used to synchronize cells at the G1/S boarder (Pedrali-Noy et al. 1980).
Synchronization of Fucci-BMSC was performed using 5 µg/ml aphidicolin for 24 hours. Fucci2-HeLa cells were treated with descending concentrations from 5 µg/ml down to 0,3 µg/ml. If not stated otherwise 0,3 µg/ml aphidicolin were used for Fucci2-HeLa cells for 18 hours. Cells were released by an initial medium change to remove aphidicolin and a second medium change 15 minutes later to ensure that residual aphidicolin is removed.

2.2.18.3 Thymidine-Nocodazole block

2 mM of thymidine were added to HeLa cells at 40 % confluency for 24 hours. After washing cells were released in culture medium for 3 hours. Subsequently, cells were

treated with 100 ng/ml nocodazole for 12 hours. Cells were released by washing cautiously and new culture medium was added. Cells progressed synchronously through mitosis.

2.2.18.4 Serum deprivation

Fucci-BMSC were seeded in 24-well plates and cultured with αMEM without serum for 24 hours. After addition of serum cells were fixed at different time points.

2.2.19.   Live Cell Imaging

Live cell imaging of Fucci-BMSCs and Fucci-MEFs was performed at the Cell Observer. 20.000 cells were seeded in collagen coated 4well glass bottom chambers. Images were taken every 10 minutes for up to 27 hours with 10 x magnification. Used filtersets were 43 HE Cy3, shiftfree (E), 38 HE eGFP shift free (E) and transmitted light. Time lapse images were analyzed using Image J plugin MTrack J.

Live cell imaging of Fucci2-HeLa cells was performed at the Cell Observer. The Colibri-System was used to excite mCherry and mVenus. Additionally transmitted light was used. The MatLab based Fucci Analysis software, developed by Matthias Lorenzen (IST, Stuttgart), was used to analyze imaging data obtained with Fucci2-HeLa cells.

2.2.20.   PKDreporter assay

PKDrep, a PKD activity reporter, and G-PKDrep, the Golgi targeted variant (Czondor et al. 2009; Fuchs et al. 2009), were transfected using Turbofect according to manufacturer's instructions. Briefly, $8*10^5$ cells were seeded in a 6 cm dish. 7 µg DNA, 700 µl Optimem and 14 µl Turbofect were mixed and incubated at room temperature for 20 min. Subsequently, the transfection mix was added to the growth medium on the cells. The pSer294-specific antibody was used to detect the phosphorylation state of the substrate sequence and GFP antibody was used to normalize phosphorylation to expression levels of the construct.

3. Results

To address the question of how PKD and the RAF/MEK/ERK pathway control mitotic entry an adequate cellular system was needed. Because the control of cell cycle in stem cells is of particular interest for clinical application, human and mouse MSCs were used for initial studies. The first step was to characterize and verify the stem cell potential of human MSC. Therefore cells from two different sources – the bone marrow and the umbilical cord – and from three different donors each were used. BM-MSC were kindly provided by the IGB Fraunhofer Institute in Stuttgart and UC-MSC by Prof Eissner from the LMU in Munich. Both cooperation partners were part of the BMBF funded Systec project number 0315506A.

3.1. Characterization of hBM-MSC and hUC-MSC

Cells from both sources displayed a typical spindle-shaped phenotype described for MSCs in literature (Dominici et al. 2006) (see Figure 4A). Proliferation in low passages was monitored over several days. UC-MSC showed an increased proliferation rate compared to BM-MSC under standard culture conditions (see Figure 4B). Remarkably, the proliferation capacity of both MSCs decreased with increasing passage. BM-MSC stopped expanding after 7 passages whereas UC-MSC showed dramatically reduced growth after 11 passages (see Figure 4C).
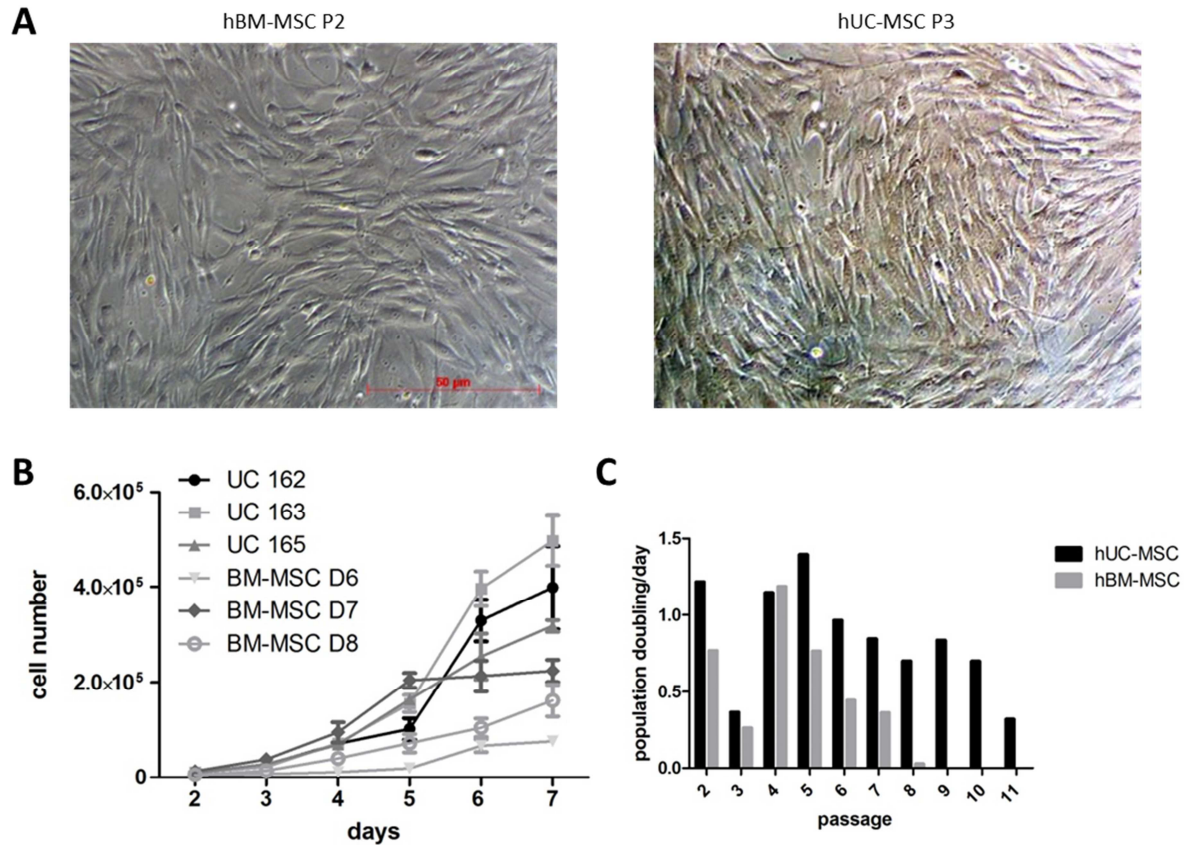
Figure 4 Phenotype and proliferative characteristics of human BM – and UC-MSC
(A) Transmitted light images of BM (passage 2) and UC-MSC (passage 3). Scale bar = 50 μm (B) Proliferation assay of three isolates of UC-MSC and three isolates of BM-MSC. 5000 cells were seeded on day 0 and cell number was counted on the indicated days. Shown is the mean of three wells ± SD (C) Relationship between cell passages and population doubling per day. BM and UC-MSC cultures were continuously passaged. Cell numbers of BM-MSC D7 and UC-MSC 162 were recorded and population doubling per day was calculated as described in 2.2.3.

To assess the stem cell potential surface marker expression of UC- and BM-MSC with three different isolates each was analyzed in collaboration with Dr. Georg Siegel (Institute of Clinical and Experimental Transfusion Medicine (IKET), University Hospital Tübingen, Tübingen, Germany). According to the International Society of Cellular Therapy human MSCs must express certain cell surface markers such as CD73, CD90, and CD105, and lack expression of other markers including CD45, CD34, and CD14. The expression panel of all isolates was in accordance with these criteria (see supplements 6.1). However, there were some differences between the UC and BM-derived MSCs. CD56 and CD173 were only expressed on MSC of UC origin. In contrast GD2, a neuronal ganglioside, as well as W8B2, the tissue nonspecific alkaline phosphatase, were only detectable in higher fractions of MSC from the BM (see Figure 5).
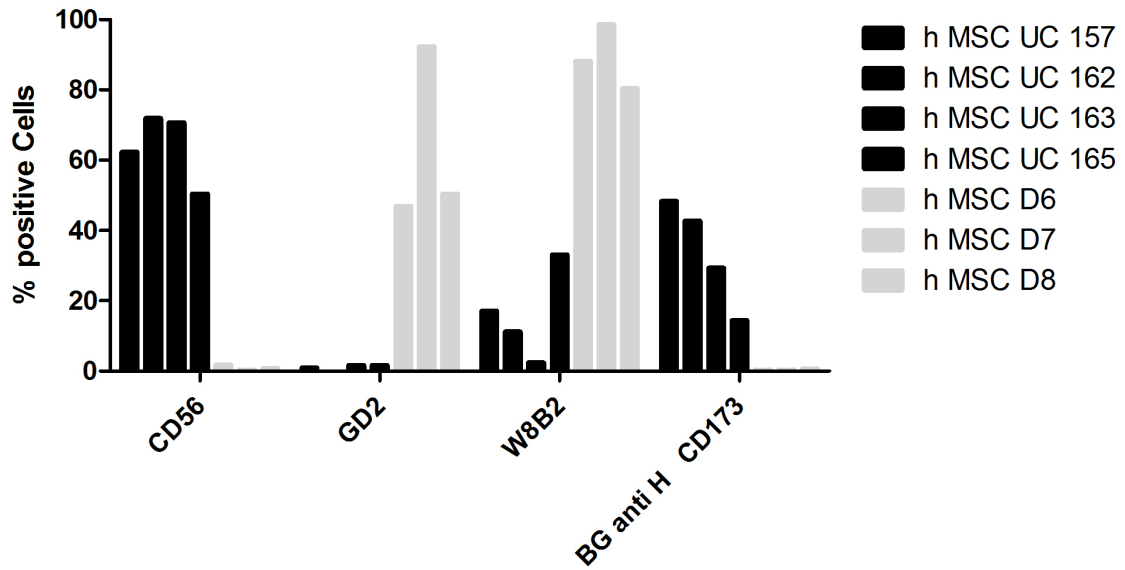
Figure 5 Surface marker expression human BM and UC-MSC
Flow cytometry analysis of human BM and UC-MSC in passage 4 with exception of UC 162 (passage 1). Cells were stained with indicated antibodies and binding was analyzed by flow cytometry. Unstained cells were used as a negative control. % of positive cells was determined with FlowJo software. Experiment and analysis was performed by Dr Georg Siegel and colleagues.

The most important verification of mesenchymal stem cell characteristics in vitro is the ability of the cells to differentiate towards a more committed osteo-, adipo- and chondrogenic state. All tested isolates, either of BM or UC origin, were able to show mineralization visible by Alizarin red staining (see Figure 6).

UC 162

UC 165

− +   − +

Alizarin-red

Oil-red

Alcian-blue

UC 163

D7

− +   − +
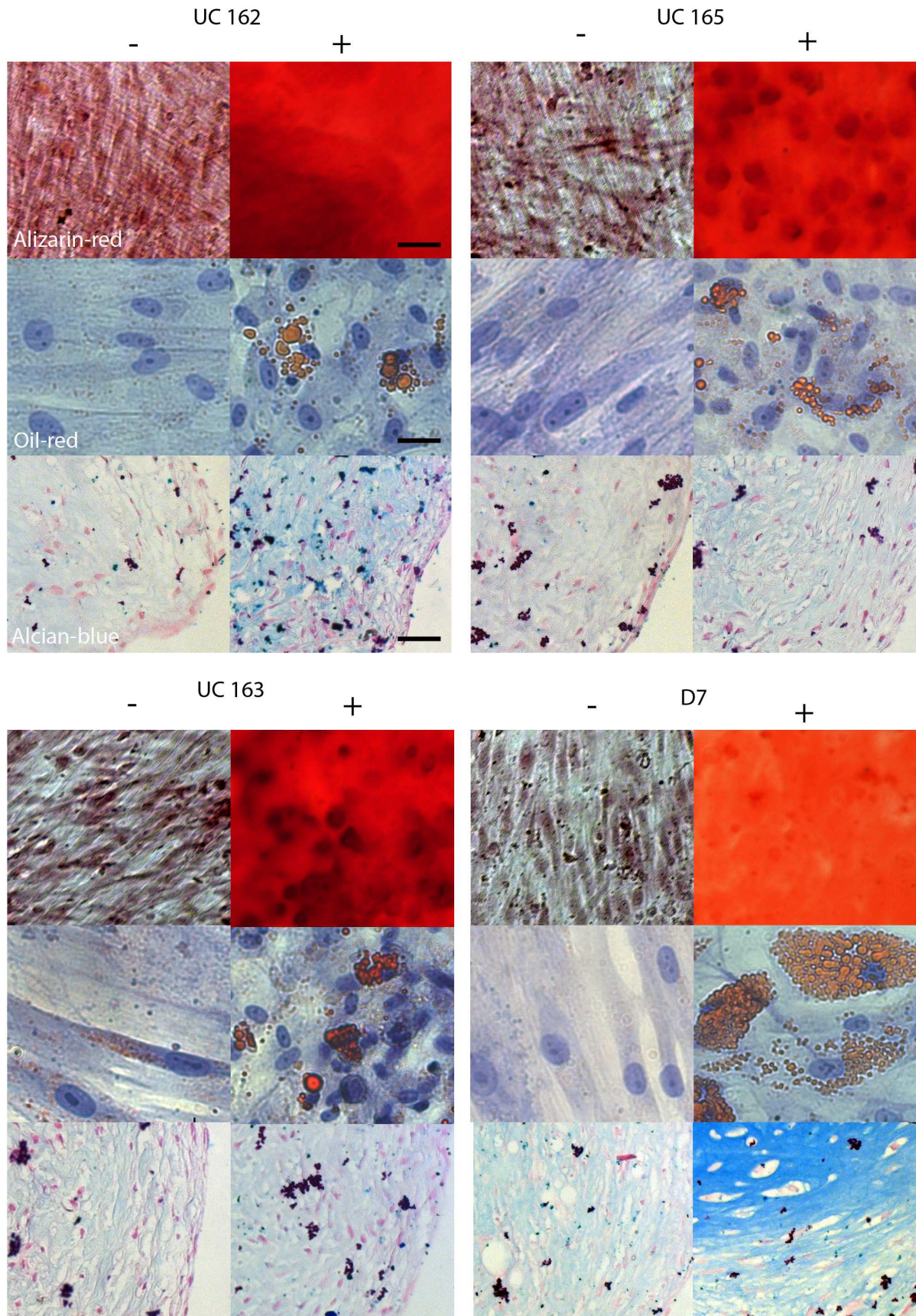
Figure 6 Multipotency of human BM and UC-MSC
Differentiation of BM and UC-MSC. hMSC were cultured in vitro in adipogenic, osteogenic, or chondrogenic media (indicated by +) to assess multilineage differentiation capability. The cells were fixed and stained with Alizarin Red (osteogenesis), Oil Red O (adipogenesis), or Alcian Blue

(chondrogenesis) for adipocyte, osteoblast, or chondrocyte differentiation. Cells cultured in standard growth medium served as a control for adipogenic and osteogenic differentiation. For chondrogenic differentiation cell pellets in chondrogenic differentiation medium without TGF-ß3 served as a control. Scale bars = 200 µm (osteogenesis), 50 µm (adipogenesis), and 100 µm (chondrogenesis).

They were also able to generate lipid droplets indicative of adipogenic differentiation. However, the formation of lipid droplets was more pronounced in MSC from BM (see Figure 6). Finally, all isolates could generate cell pellets and were stained positive for mucopolysaccharadis and glycosaminoglycans showing commitment to the chondrogenic lineage. Of note, the TGF-ß$_3$ specific effect was stronger in BM-MSC (see Figure 6). Taken together, these differentiation assays show the in vitro multipotency of these hMSC isolates.

3.2. Isolation of mBMSC

The knowledge obtained from human MSC was then used to isolate primary BMSC from mouse. A recent publication demonstrated that only bone marrow-derived stromal cells (BMSC) have osteogenic potential in vivo and are thereby bona fide stem cells (Sacchetti et al. 2007). Thus, BMSCs from femur and tibia of eight week old C57Bl6 mice were isolated. Animals of this young age were chosen since age-related effects on BMSCs were reported (Wilson et al. 2010; Bellantuono et al. 2009). Additionally, cells of C57Bl6 origin are compatible with most transgenic mouse models available. To isolate MSC from mouse BM several isolation methods were available. Most strategies rely on a single, or a combination of sorting steps to ensure a relative purity of the isolated MSC (Xu et al. 2010). Because there is no agreement on a common surface marker panel for mouse MSC an alternate strategy published by Nadri and colleagues was used. This method relies on frequent medium changes to favour initial growth of MSC, resulting in less contamination with other cell types such as hematopoietic or myeloid cells (Soleimani & Nadri 2009).

After several days of cultivation small colonies were visible. The cells were passaged at 70% confluency. In total, six independent cell cultures, M2, M3, M4, M5, M6 and M7 were obtained. Of note, these six cultures stopped proliferating after the initial passaging entering a state of quiescence.
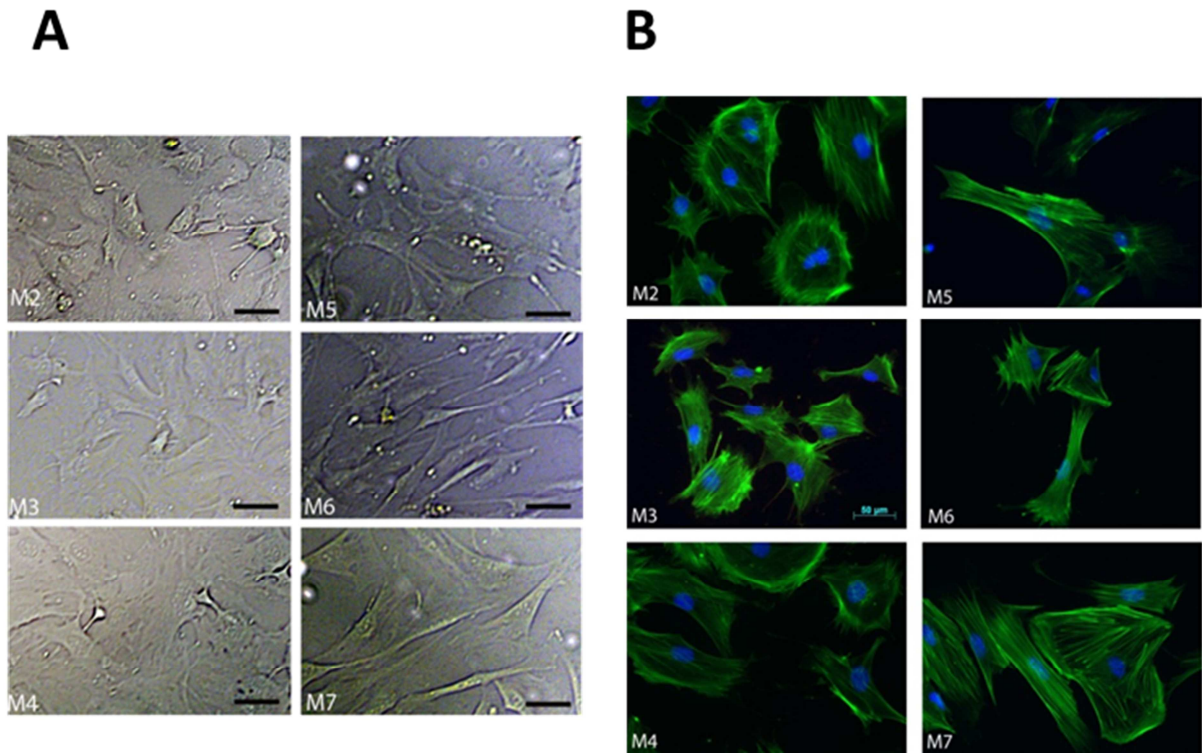
Figure 7 Phenotype of mBMSC
(A) Transmitted light images of mBMSC cells in early passage. Scale bar, 50 μm. (B) Mesenchymal phenotype of early-passage mBMSC by fluorescence microscopy. Cells were stained with Alexa488-coupled phalloidin (green). The nuclei were counterstained with DAPI (blue). Scale bar, 50 μm.

Surprisingly, the cells started to proliferate again after several weeks in culture (50 to 150 days after initial passage)(see Figure 8A). These cells showed a spindle shaped phenotype, with distinct differences in cell morphology visible between the different isolates (see Figure 7A & B). The proliferative characteristics after this state of quiescence also showed differences with the isolates M2 and M7 growing faster than M3, M4 and M6. M5 showed nearly no proliferation (see Figure 8B).
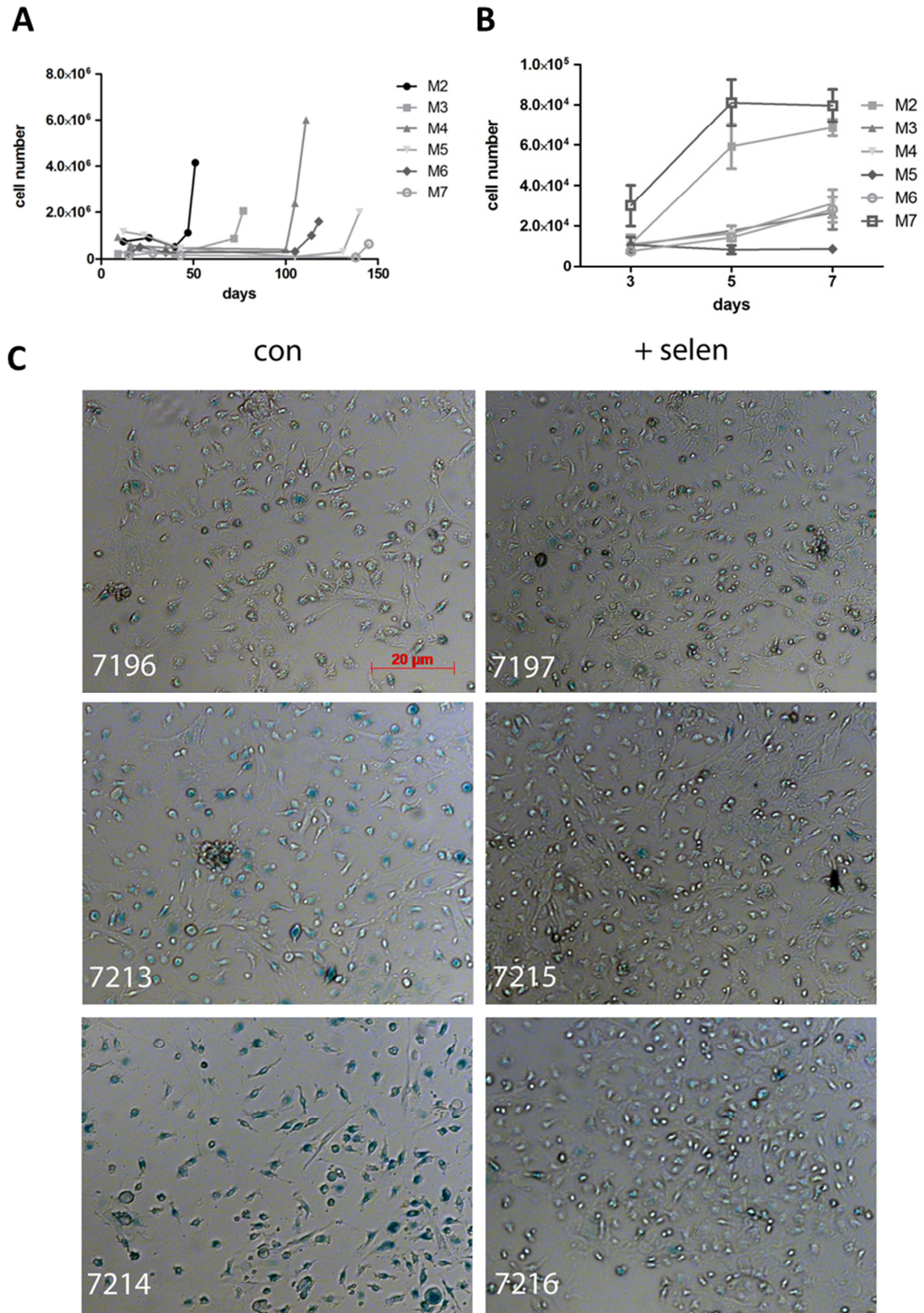
**Figure 8 Proliferative characteristics of mBMSC**
(A) Six independent cell cultures (M2-M7) were isolated from bone marrow. Cell numbers were recorded from P1 until P5. (B) Proliferation assay of six isolates of mBMSC. 5000 cells were seeded on day 0 and cell number was counted on the indicated days. Shown is the mean of three wells ± SD (C) ß-gal staining of freshly isolated mBMSCs in passage 1. Shown are images of three isolates without (con) and three isolates supplemented with 100 nM sodium selenite (+selen). Scale bar, 20 µm.

Because some reports suggested, that oxidative stress may be the cause for this quiescent state, three BMSC isolates were cultured in the presence of the antioxidant sodium selenite right after initial isolation. As a control, three freshly isolated cell cultures were isolated without sodium selenite being present in the medium. Senescent cells are characterized by the presence of beta-galactosidase activity at pH 6. Of note, beta-galactosidase activity is absent in presenescent, quiescent or immortal cells (Itahana et al. 2013). Indeed, the BMSC control isolates cultured without sodium selenite showed a remarkable beta-galactosidase staining visible by a blue colour. The beta-galactosidase staining of BMSCs cultured in the presence of sodium selenite was not that pronounced as in the control cells (see Figure 8C).

This indicates that mouse BMSCs show signs of senescence during early in-vitro culture and that addition of antioxidants may reduce the stress that causes this. Nonetheless, the BMSC isolates containing sodium selenite also showed a state of quiescence after passage 1. To further investigate the role of oxidative stress in this process reactive oxygen species (ROS) detection assays were performed. Unfortunately, this assay was not sensitive enough to detect differences in ROS generation in primary isolates (data not shown).

Intriguingly, cells overcoming the initial state of quiescence showed rapid doubling times. Hence, we determined the proliferation capacity of the multipotent cell cultures over time. As Figure 9A shows, cumulative population doublings increased steadily over time with increasing passage number. This indicates that the three cell cultures M2, M6, and M7 are potential bone marrow derived stromal cell lines.
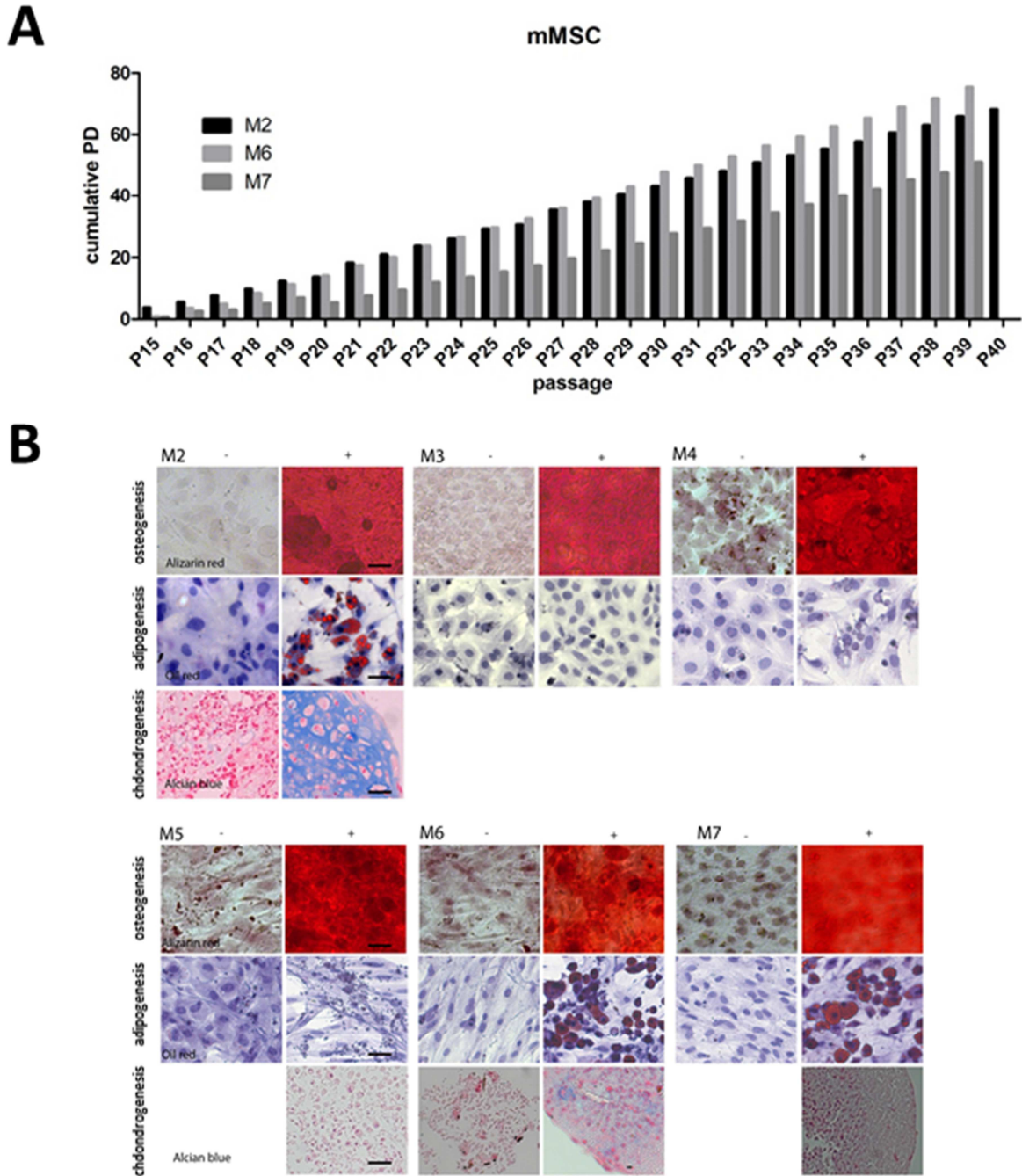
Figure 9 Proliferation potential and multipotency of immortalized mBMSC
(A) Relationship between cell passages and cumulative population doubling (PD). BMSC cultures M2, M6, and M7 were continuously passaged in α-MEM supplemented with 15 % FCS. Cell numbers were recorded and cumulative population doublings was calculated as described. (B) Differentiation of bone marrow stromal cells. BMSC were cultured in vitro in adipogenic, osteogenic, or chondrogenic media (indicated by +) to assess multilineage differentiation capability. The cells were fixed and stained with Alizarin Red (osteogenesis), Oil Red O (adipogenesis) or Alcian Blue (chondrogenesis) for osteoblast, adipocyte, or chondrocyte differentiation. Cells cultured in standard growth medium (-) served as a control. Scale bar: 100 μm (chondrogenesis), 50 μm (adipogenesis), 200 μm (osteogenesis).

To investigate whether the stromal cell cultures contained multipotent BMSCs, early passage cells (P7-9) were cultured under various conditions as described in methods to assess their capacity to differentiate into committed mesodermal lineages. In vitro multipotency towards the osteogenic, adipogenic and chondrogenic lineage could be demonstrated for the cell cultures M2, M6 and M7 (see Figure 9B). M3, M4 and M5 only showed mineralization and hence osteogenic differentiation, but failed to differentiate towards the adipogenic and chondrogenic lineage. This characterizes M3, M4 and M5 as committed osteogenic progenitors.

The three multipotent cultures M2, M6 and M7 were further analyzed for surface marker expression profile using flow cytometry (see supplements 6.2). All stromal cell populations were positive for the classical mesenchymal markers CD9, CD29, CD44, CD71, CD105 and CD106 as well as the mouse stem cell marker Sca-1 and MCAM/CD146, whereas expression of hematopoietic and lymphoid markers CD34, CD45, CD11b, CD14, CD31, CD80, CD117 and CD135 was negative. Cells were also positive for H-2Kb (MHC class Ia) and negative for the MHC class IIa (see supplements 6.2). Of note, expression of CD90, a marker in the panel of ISCT, was differentially regulated, with M2 cells lacking this marker completely whereas M6 and M7 cell lines contained a subpopulation of cells that were positive for CD90 (see supplements 6.2). The surface marker profile of the multipotent cell cultures is, thus, in accordance with a typical mouse BMSC phenotype.

3.3. Establishing a stable mBMSC cell line

To investigate whether the established mouse cell lines maintain stromal cell properties over time in vitro M2 cells were chosen for further experiments. The properties of these cells in early (P8-10), mid (P20-26) and late (P40-44) passages was analyzed. First, the cells were stained with phalloidin to visualize F-actin. Microscopic analysis revealed a spindle-shaped fibroblast-like phenotype of the cells in passage 8 (see Figure 10, left image). This phenotype did not change during in vitro culture up to passage 40 (see Figure 10, right panel).
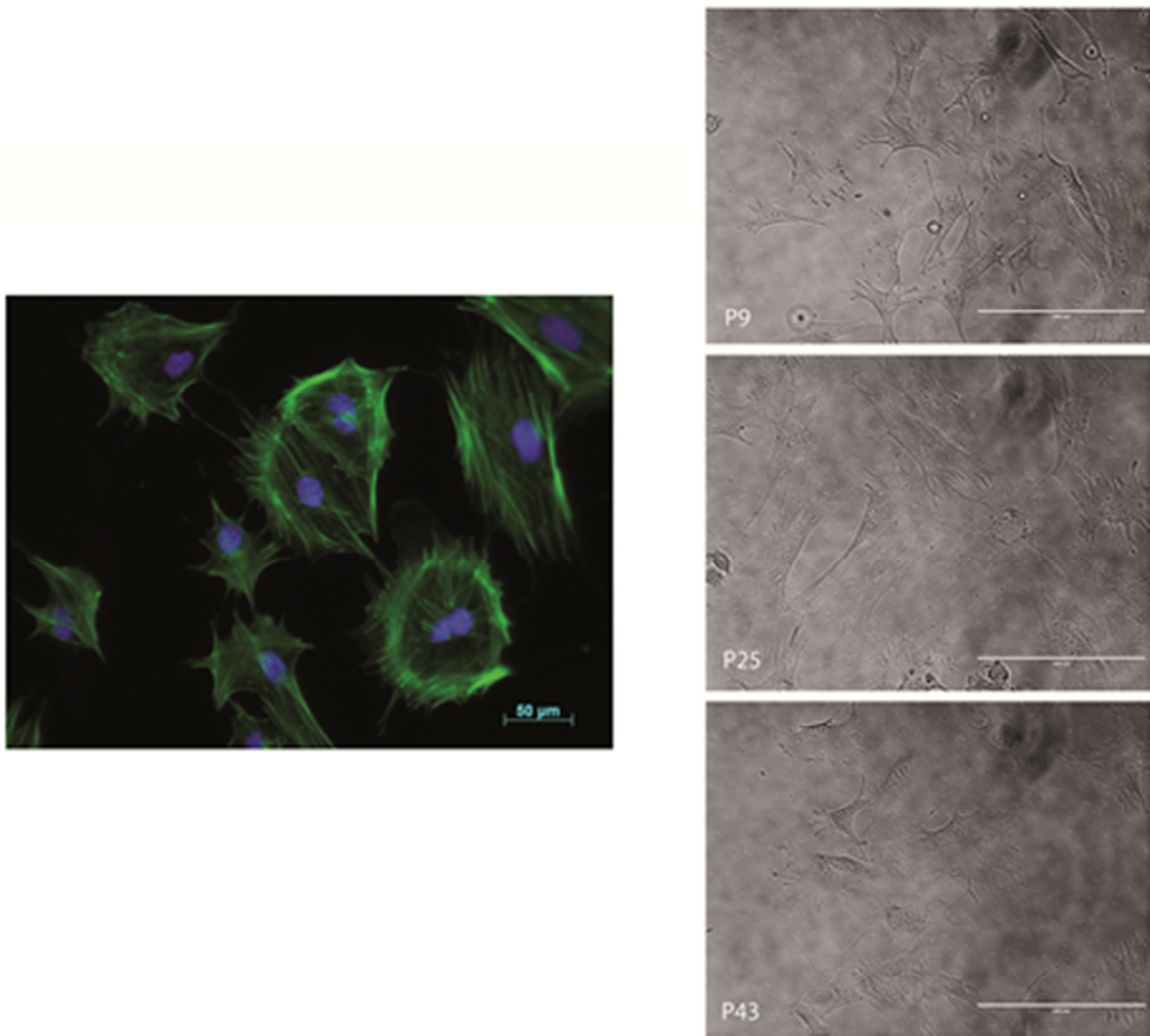
Figure 10 Phenotype of mouse cell line M2
Left: Mesenchymal phenotype of early-passage (P8) M2 cells by fluorescence microscopy. Cells were stained with Alexa488-coupled phalloidin (green). The nuclei were counterstained with DAPI (blue). Scale bar, 50 µm. Right: Transmitted light images of M2 cells in P9, P25, and P43. Scale bar, 200 µm.

Then the density-independent growth of M2 cells was analyzed using the CFU-F assay. Early-passage cells formed discrete colonies indicative of density-independent growth with a CFU-F frequency of 12%. Colony number even increased in mid-passage and late-passage cells resulting in CFU-F frequencies of 25% and 29%, respectively (see Figure 11A). This indicates that M2 cells are highly proliferative BMSCs with a clonogenic potential. Phinney and colleagues demonstrated that long-term normoxic exposure of BMSC derived cells selects for clones defective in p53 (Boregowda et al. 2012; Krishnappa et al. 2013). Indeed, Western blot analysis of cell extracts revealed that M2 cells in early, mid, and late

passage expressed high levels of p53 protein whereas p53 protein expression was absent in freshly isolated BM cells (see Figure 11B). The M2 cells thus underwent spontaneous immortalization most likely by mutation of p53, liberating the growth arrest.
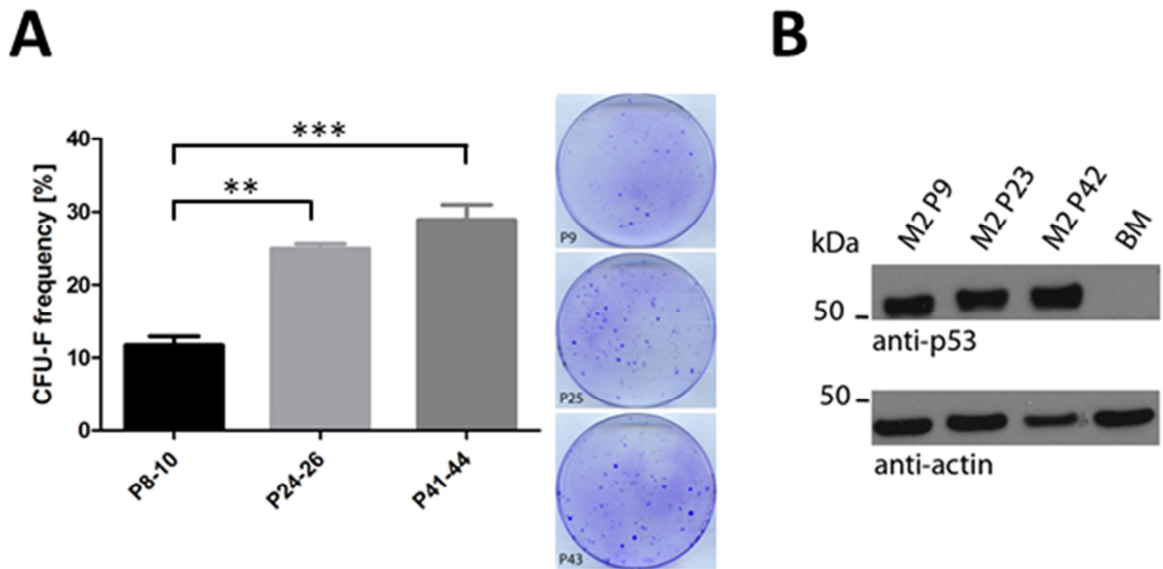
Figure 11 Characterization of the mouse bone marrow stromal cell line M2
(A) Left: CFU-F assays of M2 cells in passage P8-10, P24-26, or P41-44. Shown is the mean ± SEM of three independent experiments. **: $p<0.01$; ***: $p<0.001$. Right: Representative images of crystal violet stained CFU-F colonies formed from M2 cells. (B) Western Blot analysis of early (P9), mid (P23), and late (P42) passage M2 cells and freshly prepared bone marrow (BM). Cells were lysed, proteins separated by SDS-PAGE and p53 was detected by Western blot analysis using a specific antibody. Detection of actin served as a loading control.

Karyotyping was performed on early and late passage cells by Dr Ulrike A. Mau-Holzmann (Department of Medical Genetics, University of Tübingen, Tübingen, Germany) and showed the presence of aneuploid cells, which is typical for established mouse cell lines (Prouty et al. 1993). In Figure 12C the early passage karyotype is shown.

A

B

C
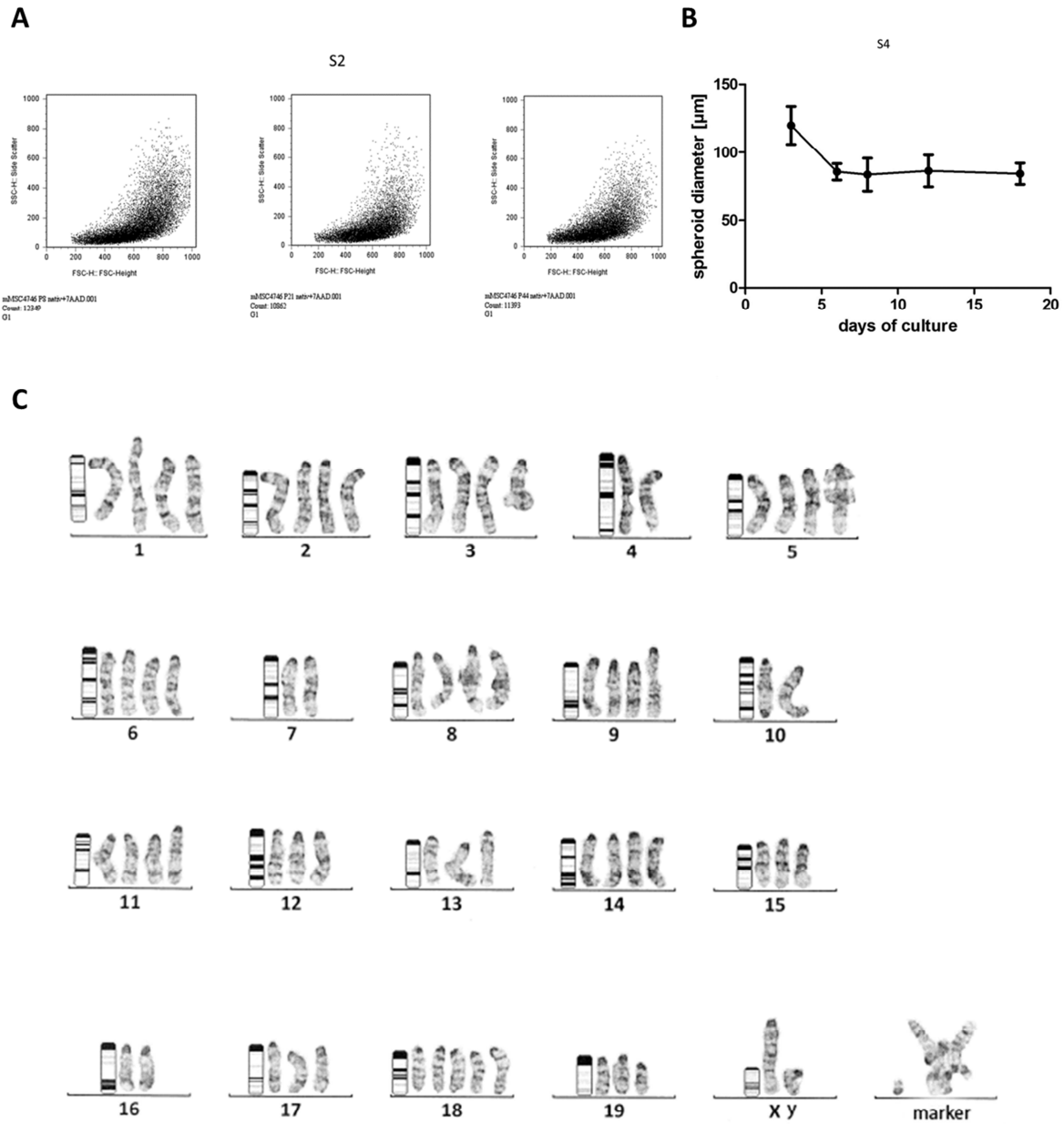
Figure 12 Stability and anchorage independent growth of M2 cells during in vitro cultivation
(A) Flow cytometry analysis of early-passage (P8), mid-passage (P21) and late-passage (P44) M2 cells. Shown is a forward scatter (FSC) vs. side scatter (SSC) dot plot. (B) Anchorage independent growth of M2 cells. 1000 M2 cells (P23) were seeded in 50 µl of α-MEM supplemented with 15 % FCS in the lid of a 100 mm culture dish. The diameter of the spheroids was calculated at indicated time points. Shown is the mean of three spheroids, error bars represent SEM. (C) Karyogram of M2 in early passage (P6) Karyotype analysis was performed by Dr Ulrike A. Mau-Holzmann (Department of Medical Genetics, University of Tübingen, Tübingen, Germany).

However, anchorage-independent growth, a hallmark of several cancer cells, could not be observed in a hanging drop assay (see Figure 12B). In line with this, the cell size and granularity did not change over time of cultivation as can be seen in flow cytometry dot-blots of early, mid, and late passage cells (see Figure 12A). Cells were further analyzed at early (P8), mid (P23) and late (P43) passage numbers for the expression of CD9, CD11b, CD34, CD44, CD45, CD71, CD105, and Sca-1 (see Figure 13A). For each culture passage M2 cells were negative for CD11b, CD34, and CD45. Comparison of common stromal cell surface markers in M2 cultures revealed a cell passage independent expression of CD9, CD71, and CD105, and Sca-1. Of note, late-passage cells even displayed a higher expression of Sca-1 compared to early and mid-passage cells. Early-, mid-, and late-passage cells were also positive for MCAM/CD146 (see Figure 13A) and negative for CD90 (data not shown). FACS profiles thus demonstrate stability in marker expression during in vitro culture. Finally, subcutaneous transplantation of late passage M2 cells in nude mice did not result in tumor formation (data not shown) proving that a malignant transformation has not occurred. Taken together, these data demonstrate phenotypic and functional stability of M2 cells during in vitro culture.
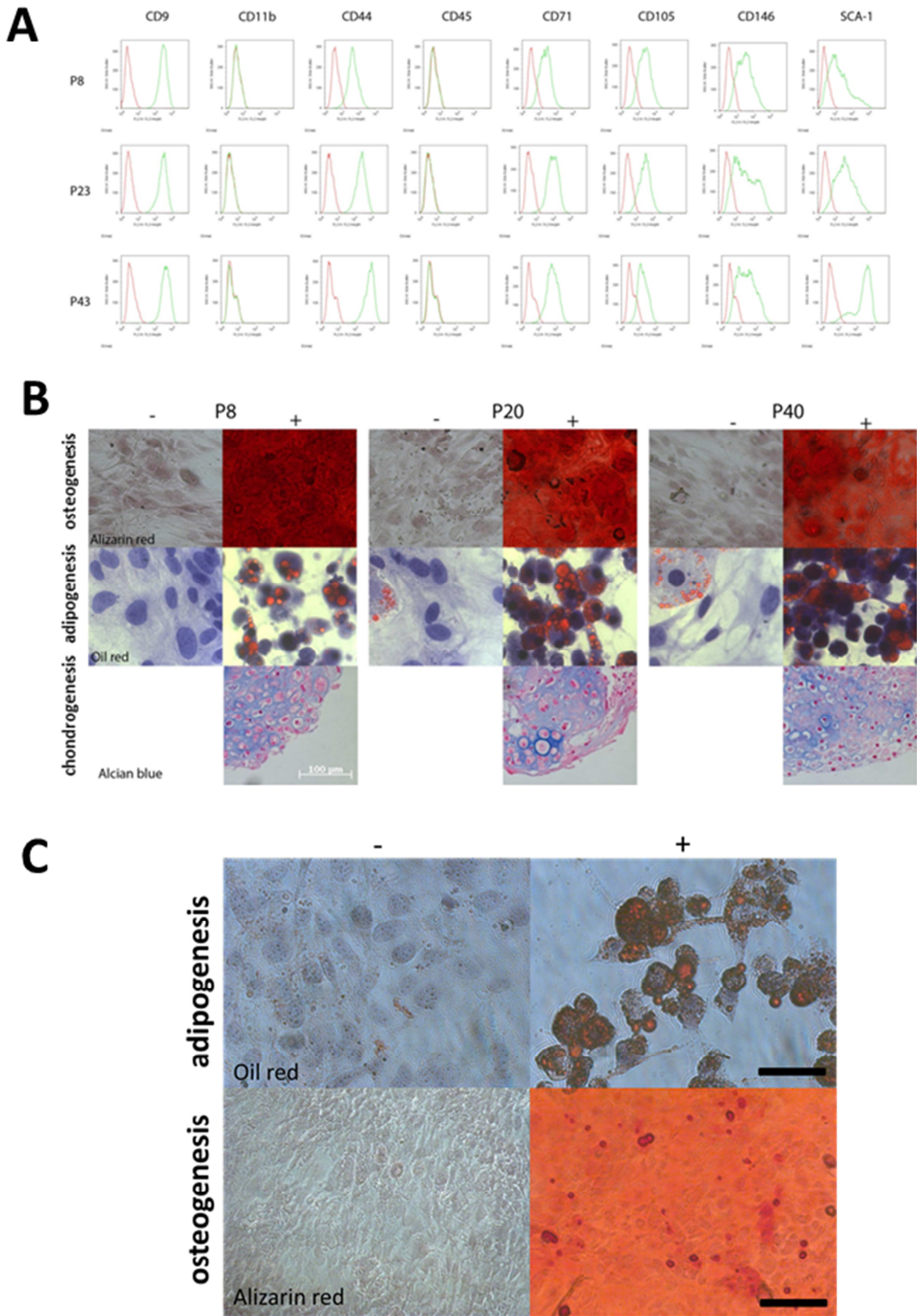
Figure 13 Characterization of the mouse bone marrow stromal cell line M2
(A Flow cytometry analysis of M2 cells in passage 8, 23, and 43. Cells were stained with indicated antibodies and binding was analyzed by flow cytometry (green). Unstained cells were used as a negative control (red). (B) Differentiation of M2 cells. M2 cells in passage 8, 20 or 40 were cultured in vitro in adipogenic, osteogenic, or chondrogenic media (indicated by +) to assess multilineage

differentiation capability. The cells were fixed and stained with Oil Red O (adipogenesis), Alizarin Red (osteogenesis) or Alcian Blue (chondrogenesis) for adipocyte, osteoblast, or chondrocyte differentiation. Cells cultured in standard growth medium (-) served as a control. (C) Clones obtained by serial dilution were cultured in vitro in adipogenic or osteogenic media (indicated by +) to assess multilineage differentiation capability. The cells were fixed and stained with Oil Red O (adipogenesis) or Alizarin Red (osteogenesis) for adipocyte or osteoblast differentiation. Cells cultured in standard growth medium (-) served as a control. A representative result from one clone is shown. Scale bar: 100 µm (chondrogenesis), 50 µm (adipogenesis), 200 µm (osteogenesis).

Next, it was investigated whether multipotency of M2 cells was retained during long-term in vitro culture. Indeed, osteogenic, chondrogenic and adipogenic differentiation could be successfully induced in M2 cells of early (P8), mid (P20) and late (P40) passages (see Figure 13B). A spontaneous adipogenic differentiation in late-passage cells, however, only when cultured at high cell density, was observed. Because the M2 cell line was developed from bulk culture and could be of polyclonal origin, the aim was to analyze whether the observed multipotency can be tracked to individual cell clones. Thus serial dilutions of late-passage cells (P42) were performed and microscopically single cell state immediately after plating was verified. In total, progeny from 24 individual clones was analyzed with respect to their osteogenic and adipogenic differentiation potential. All clones were able to differentiate towards the adipogenic and osteogenic lineage in vitro (for representative clone see Figure 13C). Of note, the chondrogenic differentiation potential of these clones was not analyzed.

Next the expression of marker proteins specific for adipogenic or osteogenic differentiation was analyzed by quantitative real-time PCR. Adipogenic and osteogenic differentiation was induced in mid-passage (P21-24) M2 cells by culture in the respective differentiation media and gene expression assessed after 12 days and 21 days, respectively. As a control, cells incubated for 12 or 21 days in growth medium was used. To show adipogenic differentiation the mRNA levels of Fabp4 and PParγ1, whose expression is upregulated in adipocytes (Rosen et al. 1999; Rosen & Spiegelman 2000; Rosen et al. 2000), were measured. Additionally, DLK1 (Pref-1), which has been reported to inhibit adipogenesis and is thus downregulated in adipocytes (Hudak & Sul 2013), was analyzed. Indeed, Fabp4 and PParγ1 expression was strongly upregulated in adipogenic differentiated M2 cells (see Figure 14A). By contrast, DLK1 was only weakly expressed by undifferentiated M2 cells and expression was completely lost upon adipogenesis (see Figure 14A). To verify osteogenic differentiation osteocalcin, osteopontin and Ibsp (bone sialoprotein)

expression was analyzed, which were reported to be late, osteoblast-specific matrix proteins (Aubin et al. 1995). Indeed, a strong upregulation of mRNA levels of these matrix proteins upon incubation of mid-passage M2 cells in osteogenic medium compared to the control was observed (see Figure 14B). These data indicate that M2 cells are able to differentiate into mature adipocytes and osteoblasts in vitro. Together, these data indicate that M2 is a bone marrow-derived stromal cell line, which maintains in vitro multipotency over many in vitro passages.
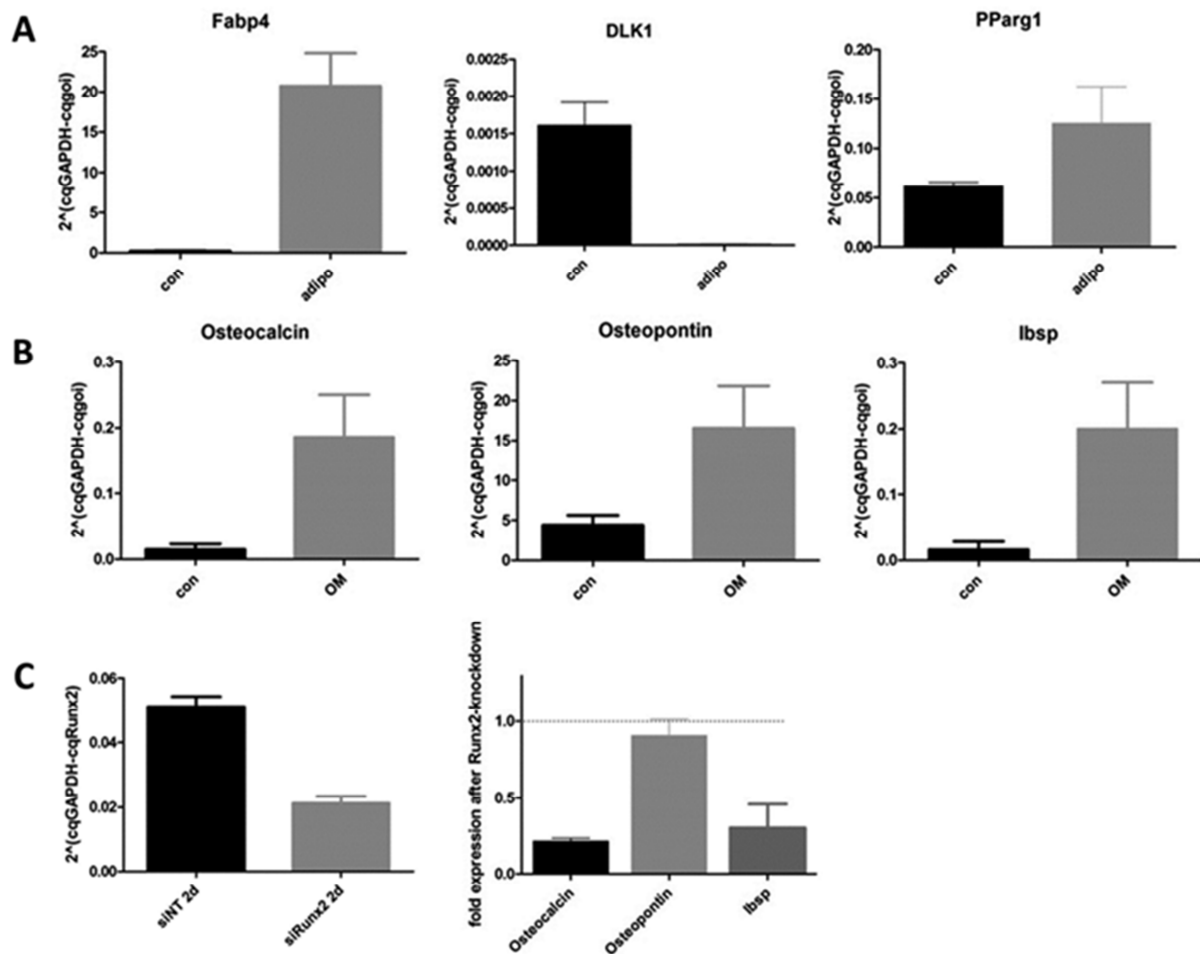

Figure 14 Adipogenic and osteogenic marker expression in M2
Mid-passage M2 cells (P21-24) were cultured in vitro in adipogenic (A) or osteogenic (B) media. RNA was extracted and levels of adipogenic marker proteins Fabp4, DLK1, and PParɣ$_1$ (A) and osteogenic marker proteins osteocalcin, osteopontin, and lbsp were measured by qRT-PCR analysis. As negative controls, cells cultured in α-MEM supplemented with 15 % FCS were used. In all cases, the relative expression was calculated by normalization to GAPDH using the ΔCq method (n=3, error bars represent SEM). (C) Mid-passage M2 cells (P21-24) were nucleofected with a control siRNA (siNT) or with a siRNA specific for mouse Runx2. Three days post transfection, RNA was extracted to measure the level of Runx2 (left). Levels of osteocalcin, osteopontin and lbsp were assessed from siNT and siRunx2 nucleofected cells cultured for 21 days in osteogenic media. The fold expression was calculated by normalization to GAPDH using the ΔΔCq method (right). Shown is the mean of four independent experiments, error bars represent SEM.

The transcription factor Runx2 is the critical key regulator in osteogenic differentiation and regulates the expression of bone matrix proteins in terminally differentiated osteoblasts (Karsenty 2008). To analyze whether the Runx2 controlled osteogenic differentiation cascade is present in M2 cells, the mid-passage (P21-24) M2 cells were transfected with a Runx2-specific siRNA to deplete mRNA and Runx2 protein. Quantitative real-time PCR of cells transfected with the Runx2 siRNA two days post transfection confirmed a reduction of Runx2 mRNA to about 40% of control siRNA (siNT) transfected, undifferentiated M2 cells (see Figure 14C). Subsequently, osteogenic differentiation was induced two days post transfection by addition of osteogenic medium. After 21 days the expression of osteoblast-specific matrix proteins osteocalcin, osteopontin, and Ibsp in siRunx2 transfected and control transfected M2 cells was monitored by quantitative real time PCR. Indeed, Runx2 depletion resulted in a 75% reduced expression of osteocalcin and Ibsp, compared to control cells. By contrast, osteopontin expression was unaffected by the initial Runx2 knockdown (see Figure 14C). This was surprising as osteopontin expression has been reported to be dependent on Runx2 (Sato et al. 1998). However, the incomplete knockdown might result in a residual Runx2 protein level sufficient to induce osteopontin expression.
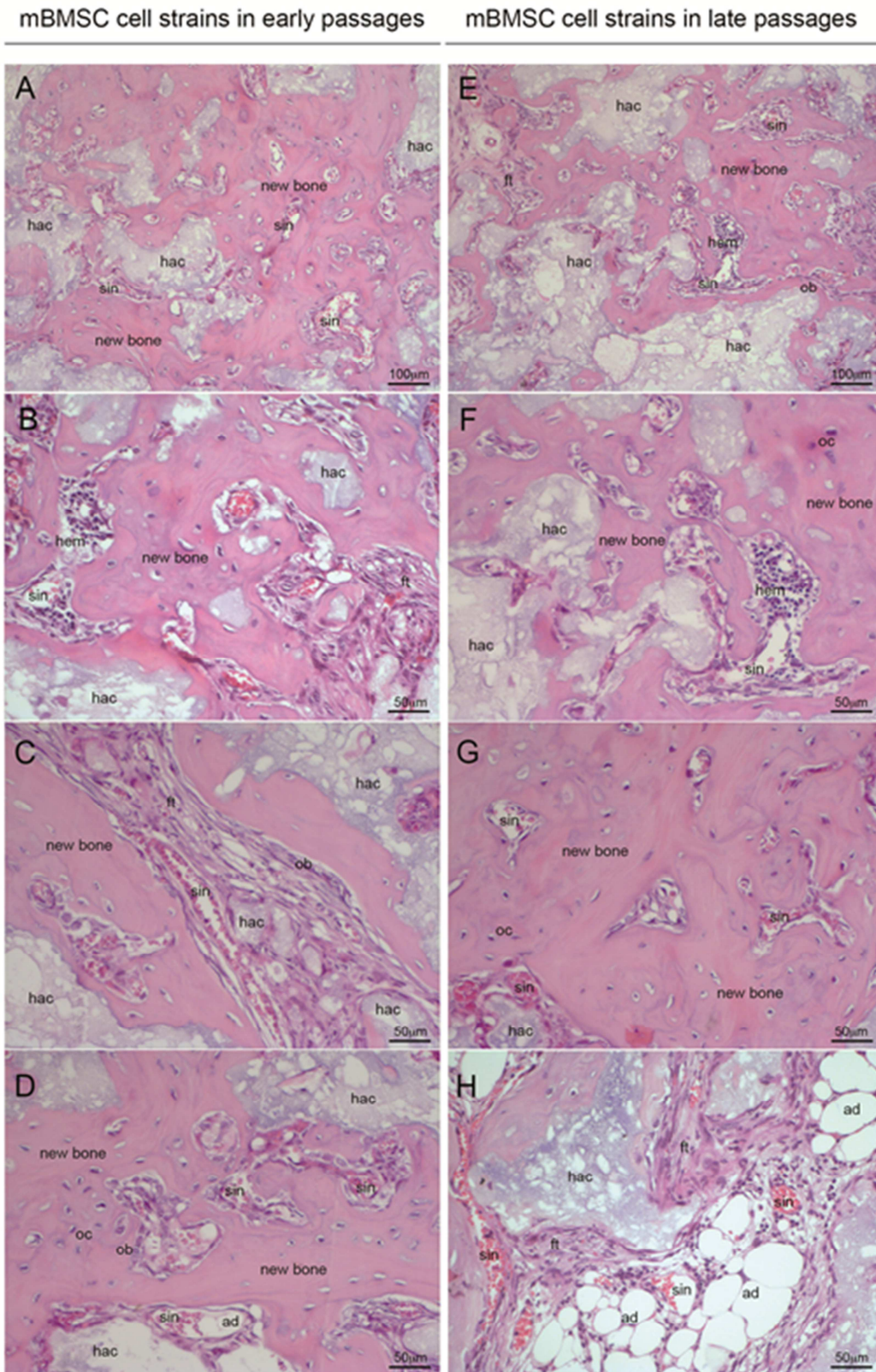
Figure 15 In vivo osteogenic potential of M2

Experiment and histology was performed by Dr Benedetto Sacchetti (Department of Molecular Medicine, Sapienza University, Rome, Italy). (A–H) 8 weeks post-transplantation both M2 cell strains in early (P8-10) and in late (P40-44) passages have formed abundant quantities of new full bone along with mesenchymal fibroblastic tissue (ft, in C and H). Bone contains differentiated osteoblasts (ob), osteocytes (oc) and adipocytes (ad; in D and H). Large caliber, branching sinusoids have formed within the fibroblastic tissue (in C and H). Hematopoietic cell clusters (in B, F and H, hem) are detectable around sinusoids (sin). hac, hydroxyapatite carrier. H&E.

BMSC generate heterotopic ossicles and are capable of establishing the hematopoietic environment in vivo (Sacchetti et al. 2007). Thus the capacity to establish bone and hematopoietic microenvironment (HME) by the transplantation of M2 cells was evaluated. This experiment was performed by Dr Benedetto Sacchetti (Department of Molecular Medicine, Sapienza University, Rome, Italy). To assess the osteogenic potential, scaffolds of osteoconductive material (hydroxyapatite/tricalcium phosphate particles, HA/TCP) loaded with M2 cells in early (P8-10) or late (P40-44) passages were generated. When transplanted subcutaneously into immunocompromised mice, early- and late-derived M2 cell strains were able to generate complete heterotopic ossicles establishing full bone, adipocytes, vessels and host derived, heterotopic hematopoietic tissue clusters (see Figure 15) proving that the M2 cell line possesses full skeletal stem cell characteristics in vivo.

3.4. Using Fucci System in mBMSC

The Fluorescence-ubiquitinated-cell-cycle-indicator system by Sakaue-Sawano et al provides a useful tool for unravelling processes linked to cell cycle progression. The aim was to establish a mouse MSC line derived from the BM of transgenic Fucci mice. These mice have a knockin of the fusion proteins mKO2-Cdt1 and mAG-Geminin, with Cdt1 being expressed only during G1 and beginning of S-phase. Geminin, on the other hand, is only expressed during S-G2/M-phase (Sakaue-Sawano et al. 2008). Therefore, cells of these mice show a cell-cycle stage dependent fluorescence (see Figure 16A & B).

A
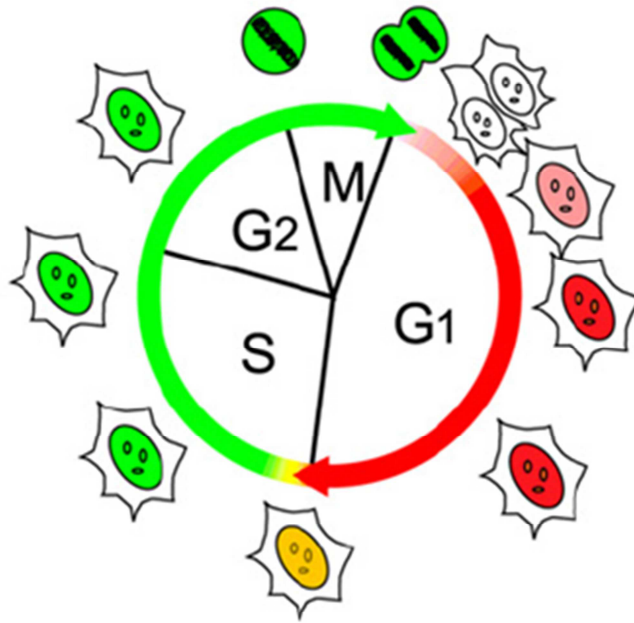
B
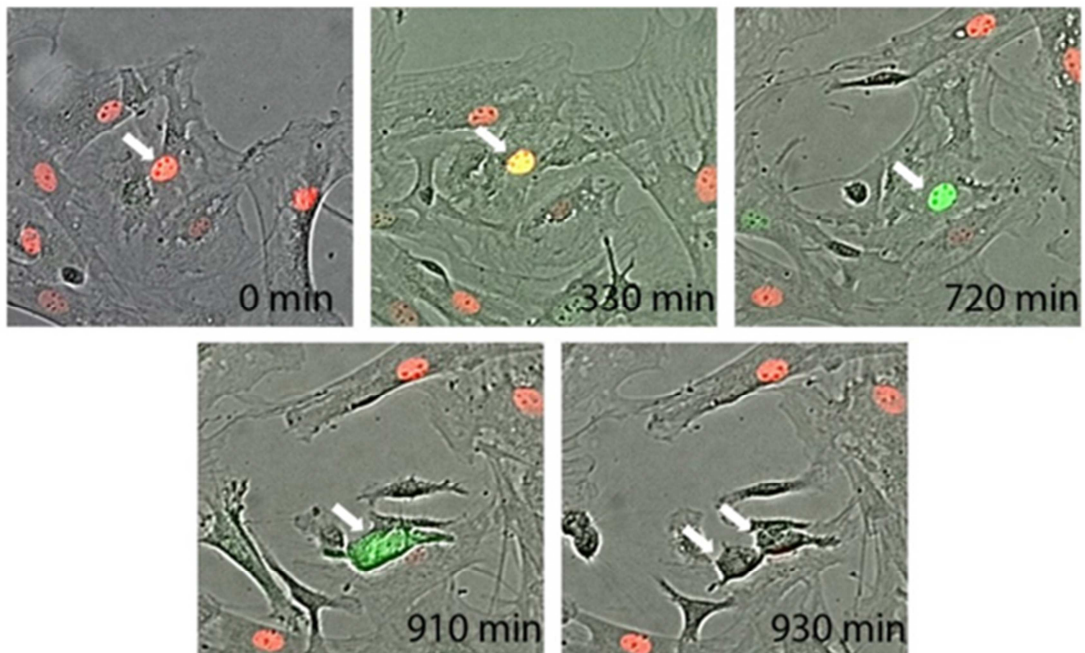
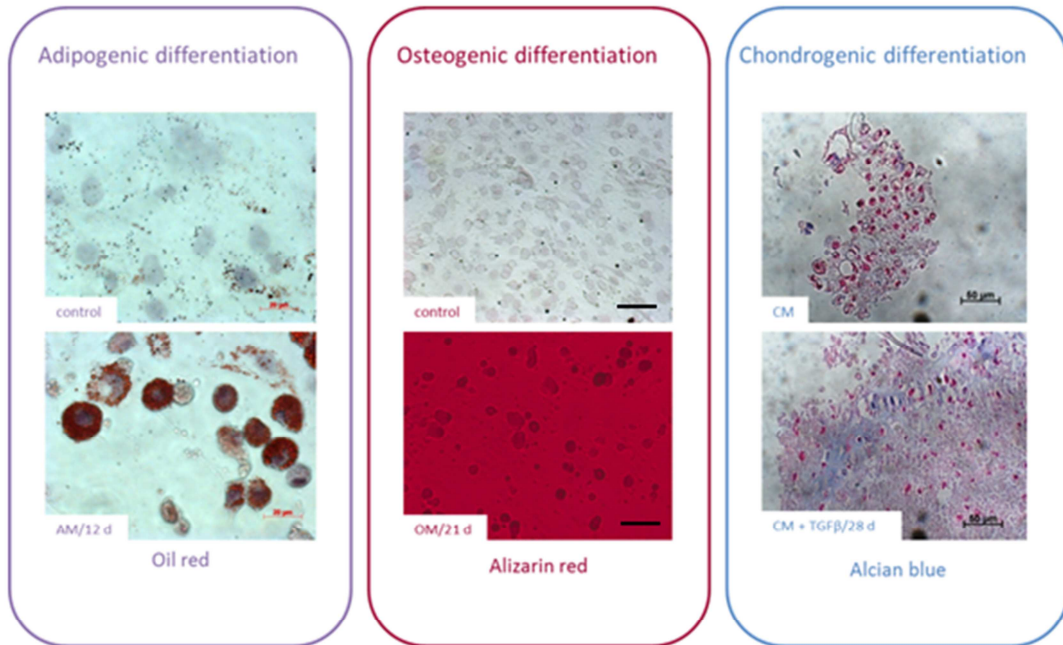**Figure 16 Phenotype of isolated Fucci-mBMSC**
(A) Cell cycle dependent expression of mKO2 (G1/s-phase) and mAG (S-and G2/M-phase) (Sakaue-Sawano et al. 2008). (B) Representative images of a time-lapse movie. At the indicated times cell cycle progression of one representative cell can be seen. White arrow indicate cell.

Cells were isolated as previously described for wild type C57Bl6 mice. To verify successful BMSC isolation multipotency was tested. The isolated Fucci-BMSC were capable of differentiation towards osteogenic, adipogenic, and chondrogenic lineage,
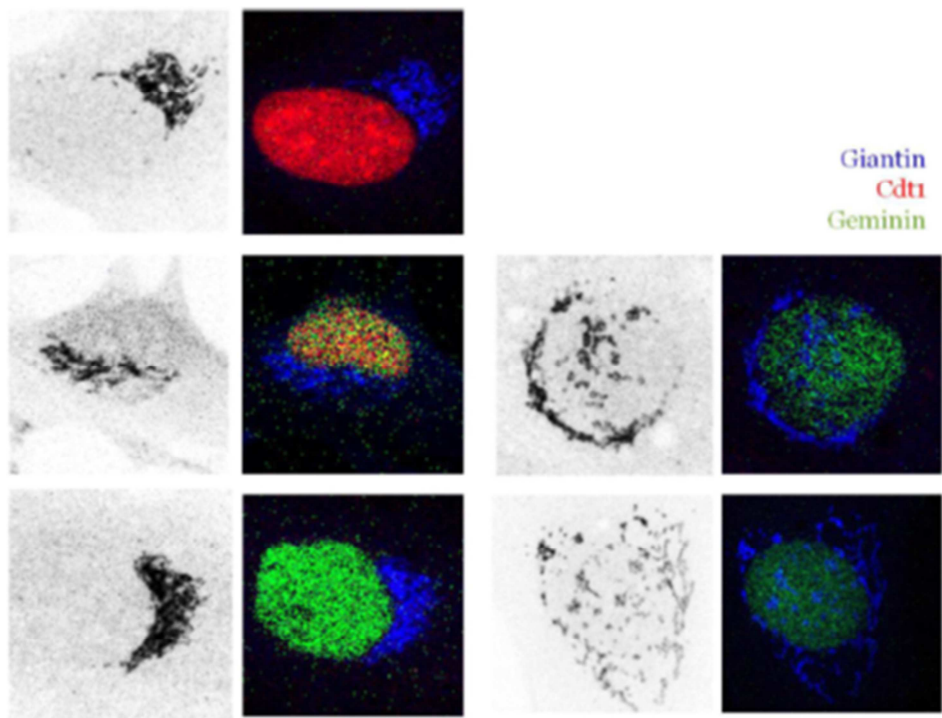
proving multipotency (see Figure 17A). With these Fucci-BMSCs a model system was generated to assess cell cycle regulation in multipotent cells with stem cell characteristics.

Figure 17 Phenotype and multipotency of isolated Fucci-mBMSC
(A) Differentiation of bone marrow stromal cells isolated from a Fucci-transgenic mouse. BMSC were cultured in vitro in adipogenic, osteogenic, or chondrogenic media to assess multilineage differentiation capability. The cells were fixed and stained with Alizarin Red (osteogenesis), Oil Red O (adipogenesis) or Alcian Blue (chondrogenesis) for osteoblast, adipocyte, or chondrocyte

differentiation. For adipogenic and osteogenic differentiation cells cultured in standard growth medium (control) served as a control. For chondrogenic differentiation cells in chondrogenic media without TGF-ß$_3$ served as a control. (B) left: representative microscopic images of cells stained with giantin. Pictures were inverted for better visualization of Golgi morphology. Right panel: red, yellow and green cell nuclei showing typical Fucci-dependent fluorescence. Blue: giantin with Alexa 633.

Next, the cell cycle state of single cells was analyzed by fluorescence microscopy. Additionally, Golgi morphology was analyzed and brought in relation to cell cycle phases (see Figure 17B).
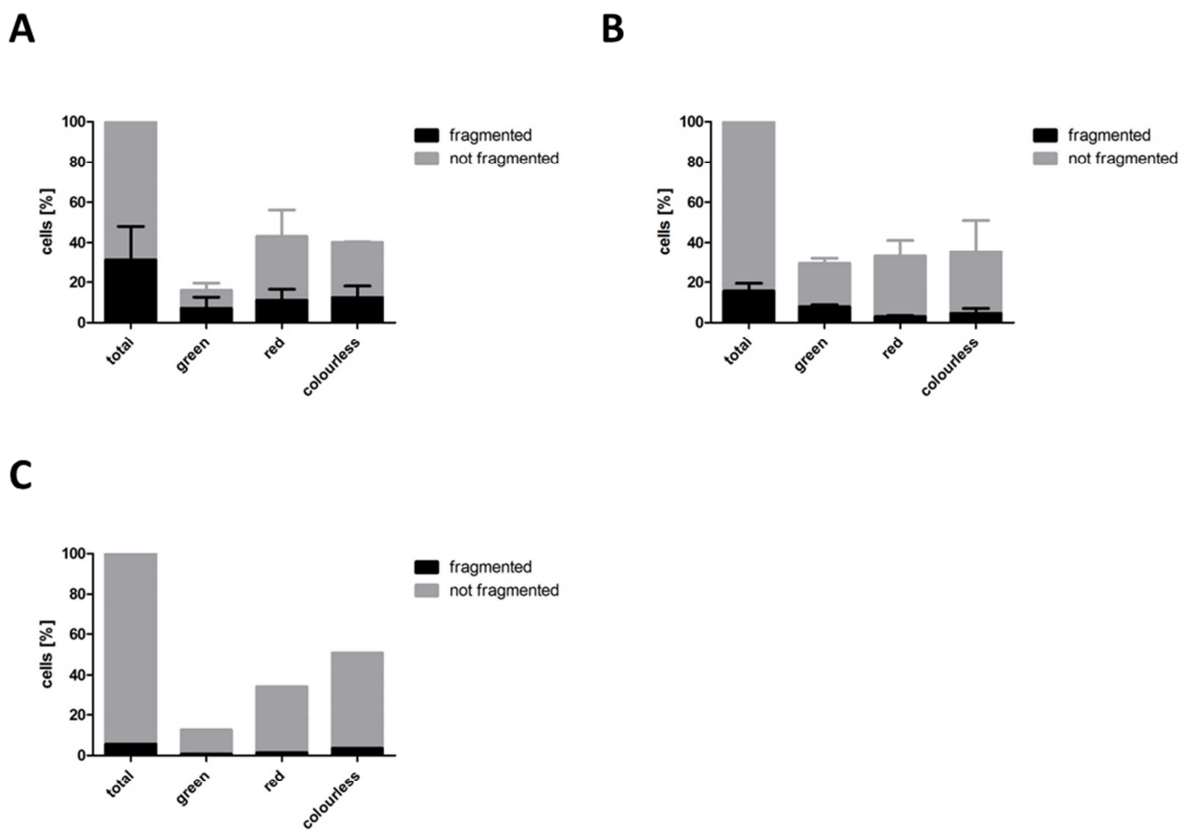
Figure 18 Effects of PKD und MEK inhibitor on asynchronous Fucci-BMSC
Fucci-BMSC were incubated with (A) culture medium for 24 h, (B) culture medium supplemented with 10 µM PKD inhibitor CID755673 (C) or culture medium supplemented with 10 µM MEK-inhibitor UO126. The cells were fixed and stained with giantin to visualize the Golgi complex. Percentage of cells with red, green, and colourless nuclei was determined in microscopic images. In each category Golgi morphology was determined. 60-150 cells were analyzed for each condition n=2 for (A) and (B), n=1 for (C).

The influence of PKD and MEK specific inhibitors on cell cycle phase length was investigated. Surprisingly nearly 40% of cell nuclei in untreated control cells did not show detectable fluorescence. However, the remaining 60% of the cell population showed green and red fluorescence indicative of G1 and S/G2/M, phase respectively (see Figure 18A). Interestingly, treatment of Fucci-BMSC with the PKD inhibitor CID755673 for 24 h increased the percentage of cells with green nuclei indicating a prolonged S/G2/M phase. A decreased number of cells in S/G2/M harboured a fragmented Golgi complex compared to control cells in S/G2/M (see Figure 18A & B). However, this is also the case for cells in G1 phase. Treatment with the MEK inhibitor UO126 did not result in an increased number of cells with green nuclei. Notably, under these conditions, almost all cells in green phase had an intact Golgi complex compared to control cells in S/G2/M phase (see Figure 18C).

One disadvantage of the analysis of asynchronous cells is that inhibition of the different kinases affects the cells in all phases of cell cycle. To analyze the impact of PKD and MEK activity specifically during the S/G2/M phase, the cells had to be synchronized. First, different synchronization strategies were tested in Fucci-BMSC.
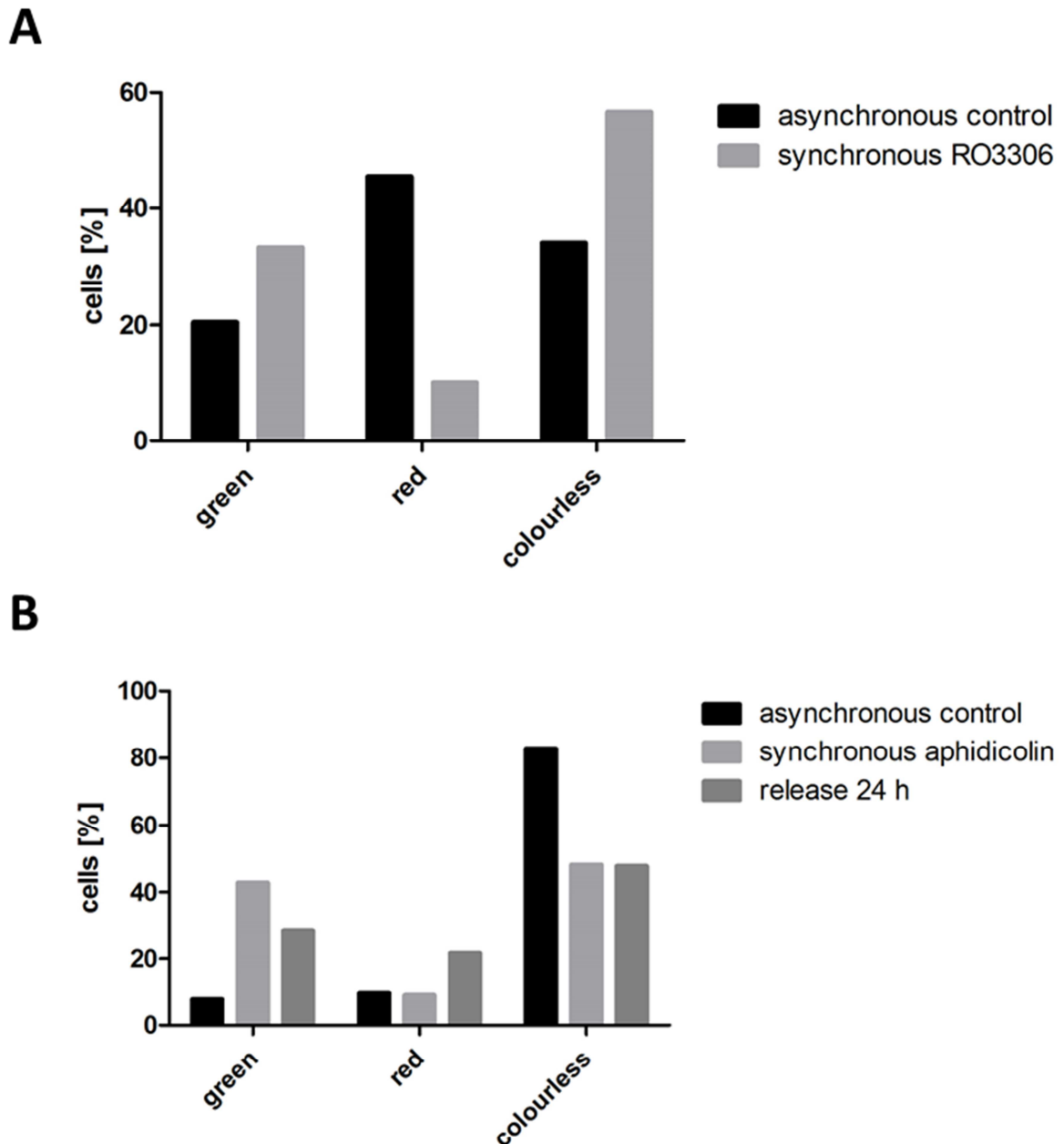
Figure 19 Synchronisation of Fucci-mBMSC
(A) Synchronisation of Fucci-BMSCs with the CDK1-Inhibitor RO 3306 (9 µM). (B) Synchronisation and release of Fucci-BMSCs with DNA-polymerase inhibitor aphidicolin (5 µg/ml). Cells were fixed and microscopic images were used to analyze nucleus specific fluorescence. 50 cells were analyzed for each condition.

The incubation of Fucci-BMSCs with the CDK1 inhibitor RO3306 resulted in an increase in cells in green phase (S/G2/M). However, most of the cells died during this treatment. After releasing the cells for 24 h all remaining cells died. Thus, synchronization with a CDK1 inhibitor was not tolerated by Fucci-BMSC (see Figure 19A). Treatment with the DNA polymerase inhibitor aphidicolin also led to an

increase of cells in S/G2/M phase. After the release, part of the cells progressed through S/G2/M phase, which can be seen in the increase in G1 phase cells 24 hours later (see Figure 19B). Similarly to treatment with RO3306, aphidicolin showed toxic effects and cells died during synchronization and also during release. Finally, cells were synchronized by 24 hours of serum starvation resulting in a nearly complete cell cycle arrest in G1. However, after the release all cells died (data not shown). Taken together, a successful synchronization of Fucci-BMSC was unfortunately not possible.

Alternatively, the effect of PKD and MEK inhibitors specifically in S/G2/M phase was investigated by live cell imaging experiments.
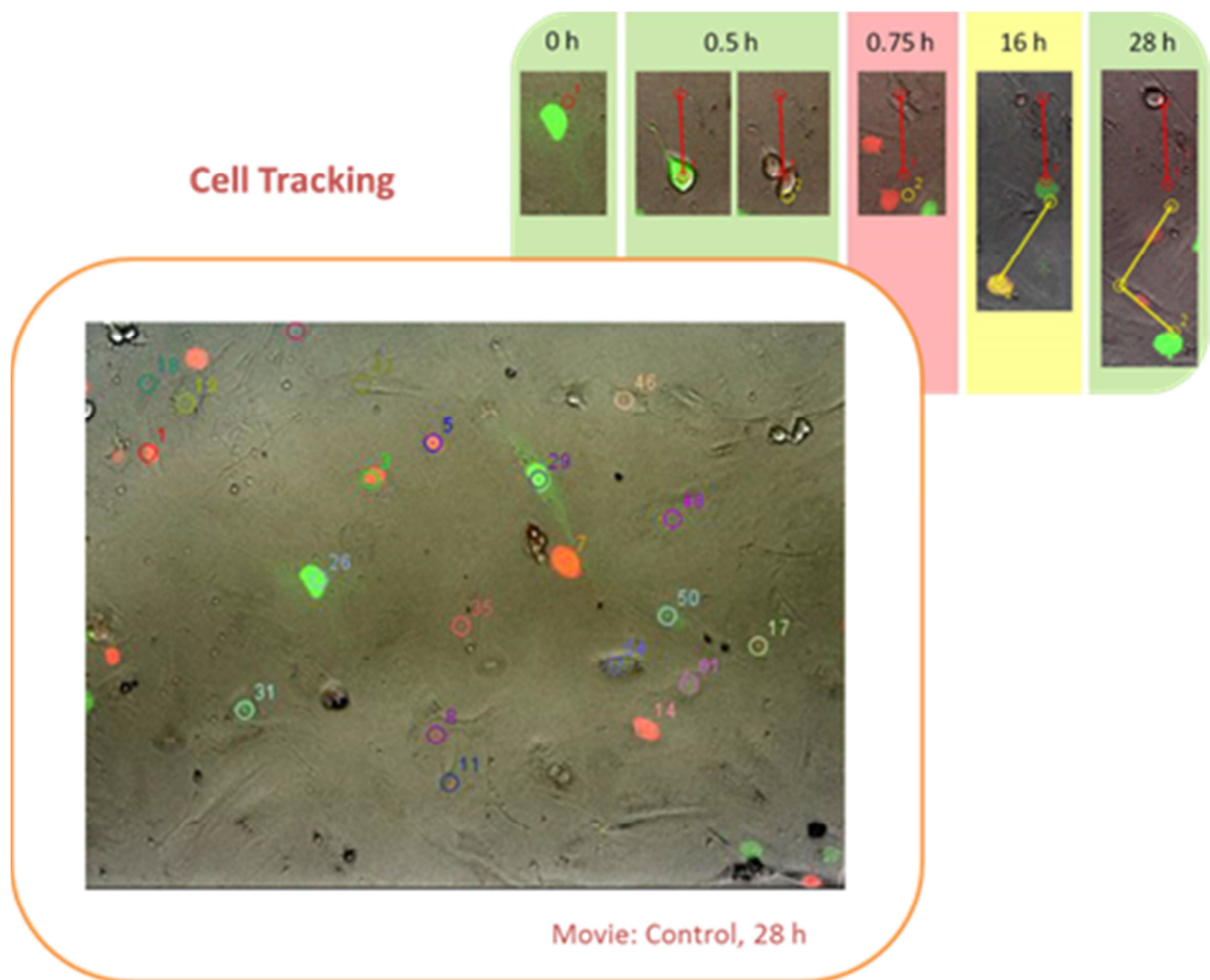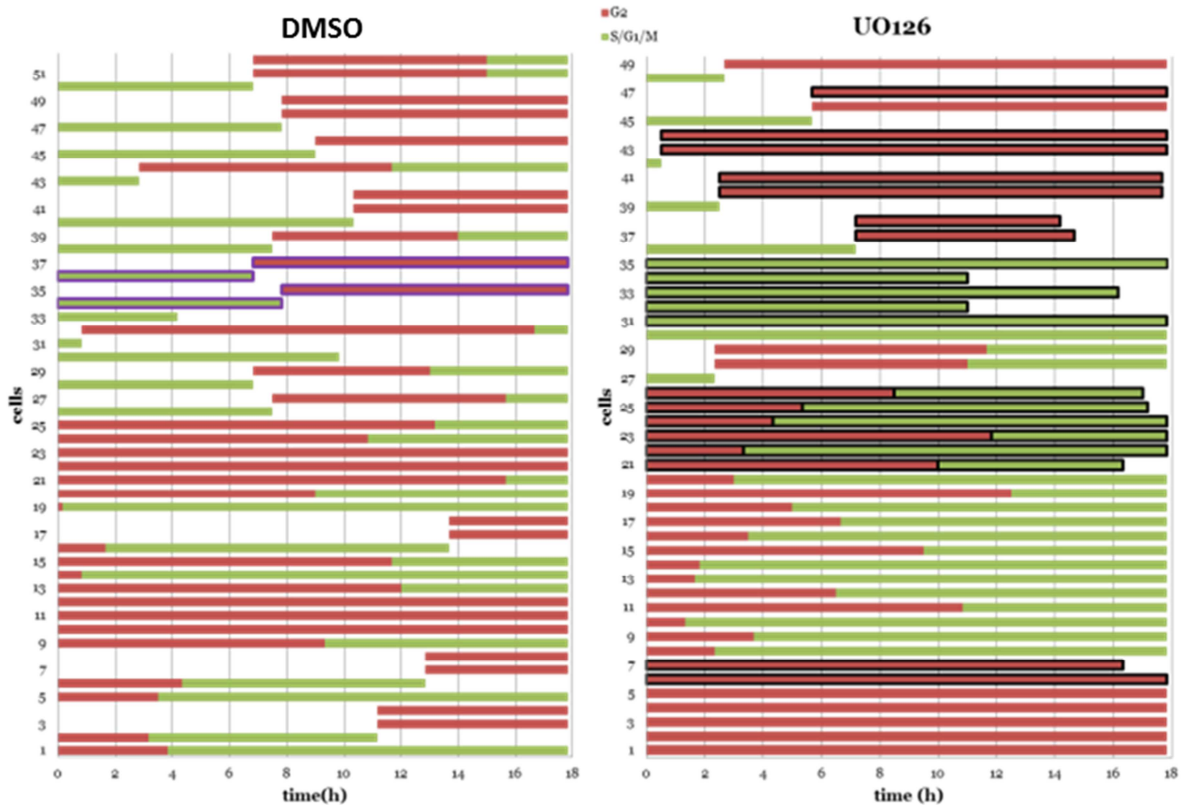

Figure 20 Live cell experiments und manual tracking of Fucci-BMSC
Representative live cell frame showing examples of cell cycle phase length verification by manual tracking.

To compare data 4-well chambers were used to image different conditions in one experiment. In a first time lapse movie cells incubated without and with 10 μM UO126 were imaged for 18 hours. A picture was taken every 10 minutes. The single cells were manually tracked throughout the movie (see Figure 20). Figure 21 shows all analyzed cells.

Figure 21 Result of live cell experiment
Graphical results of manual tracking of an 18 hours live cell movie in control and 10 μM UO126 treated Fucci-BMSC. The colours indicate the red (G1) and green (S/G2/M) phase. Black highlighted bars represent cells that died during observation.

It was obvious that a higher percentage of cells died during observation time in the MEK inhibited population. Notably, the average phase length was longer for MEK inhibited cells for both red and green phase. In line with this, there was less cell division in this population compared to control cells (see Figure 22A).
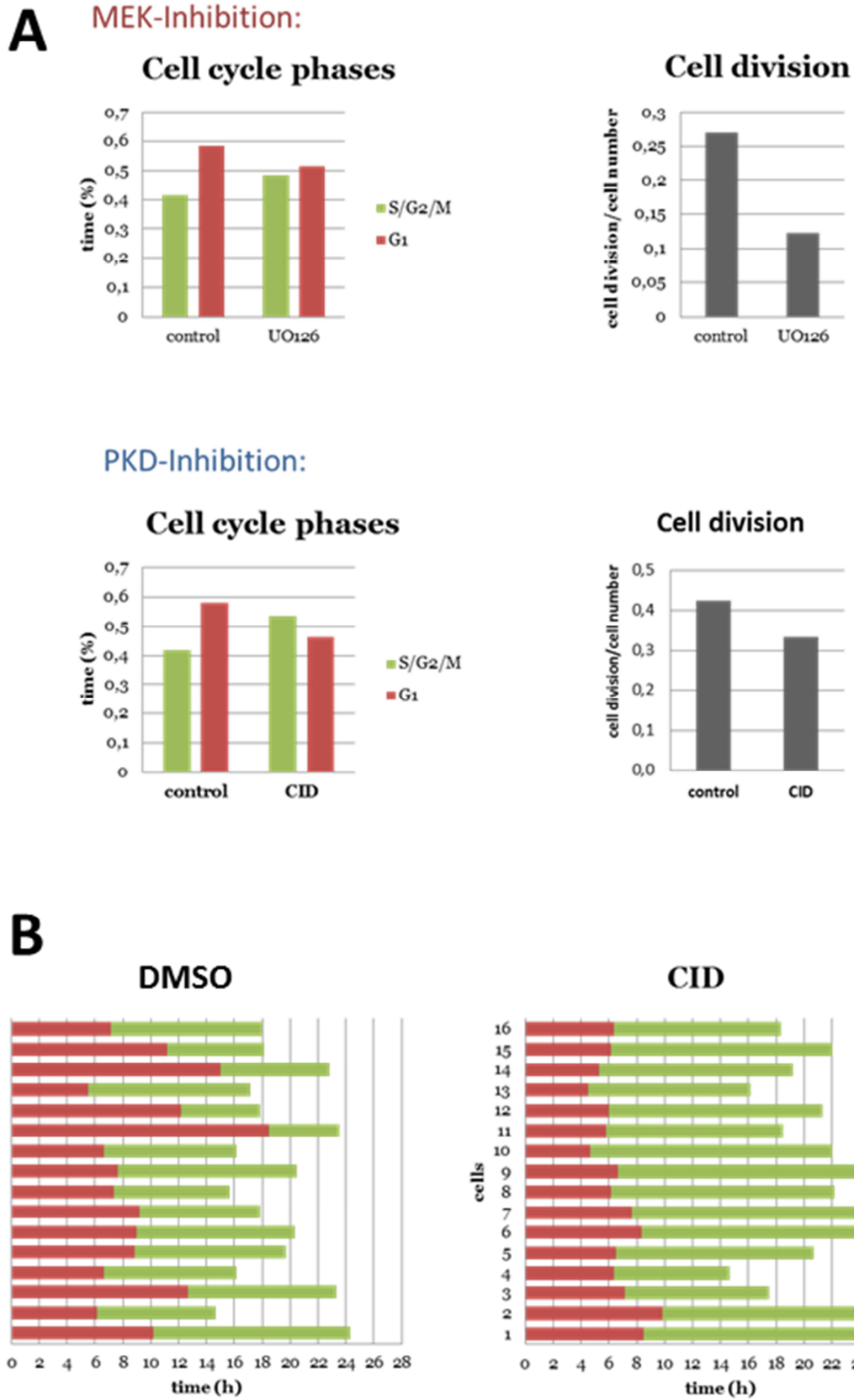
Figure 22 Analysis of live cell imaging with Fucci-BMSC
(A) Population based evaluation of cell cycle phase length and cell divisions per cell number of manual tracking data. (B) Graphical display of entire cell cycles during 28 hours of observation in live cell imaging Fucci-BMSC

Because MEK inhibition caused a delay in both, G1 and S/G2/M phases, it can be suggested that MEK has important functions in the cell cycle in Fucci-BMSC. Nevertheless, cells did not tolerate the MEK inhibitor very well resulting in enhanced cell death. The effect of PKD inhibition was analyzed in a second 28 hours live cell imaging experiment. An effect of PKD inhibition on G1 phase was not observed. Most importantly, the S/G2/M phase was strongly prolonged pointing to an involvement of PKD in this phase (see Figure 22A & B).

To get more robust primary cells tolerating the inhibitors, Fucci-MEF were isolated and immortalized by Dr Kornelia Ellwanger. Similarly to Fucci-BMSC, the expression of red and green tagged proteins was only visible in some cells. Heterogenous expression was detected in living and fixed cells confirming that a potential loss of the dye by fixation is not likely (see Figure 23). Instead, a heterogenic or too weak expression of the fusion proteins mKO2-Cdt1 and mAG-Geminin seems to be a possible reason. Because only 15-20% of the Fucci-MEF cells were showing detectable amounts of fluorescence (data not shown), further experiments with these cells were not conducted.
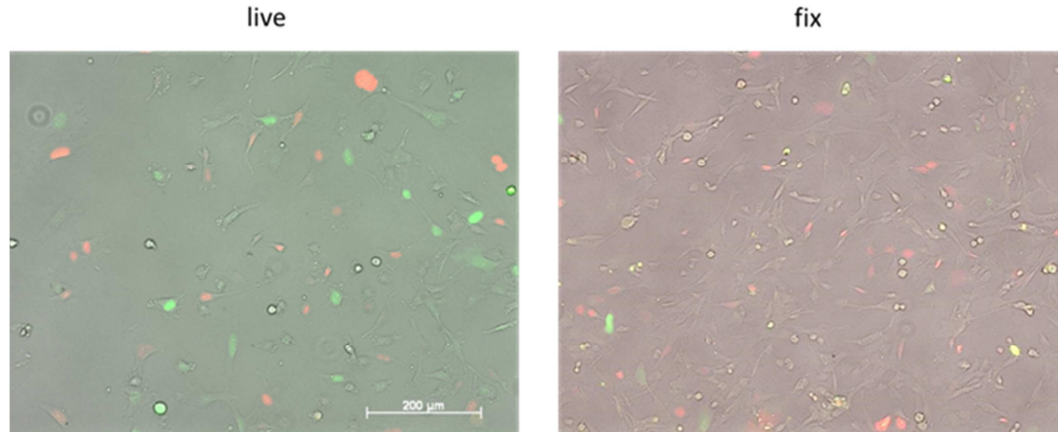
Figure 23 Phenotype of Fucci-MEF
(A) Comparison of living and fixed Fucci-MEF. Scale bar represents 200 µm.

3.5.   Fucci2-HeLa

Because the primary cells did not tolerate treatment with inhibitors and the synchronization at the G1/S border Fucci2-HeLa cells were chosen for further experiments (see Figure 24A).
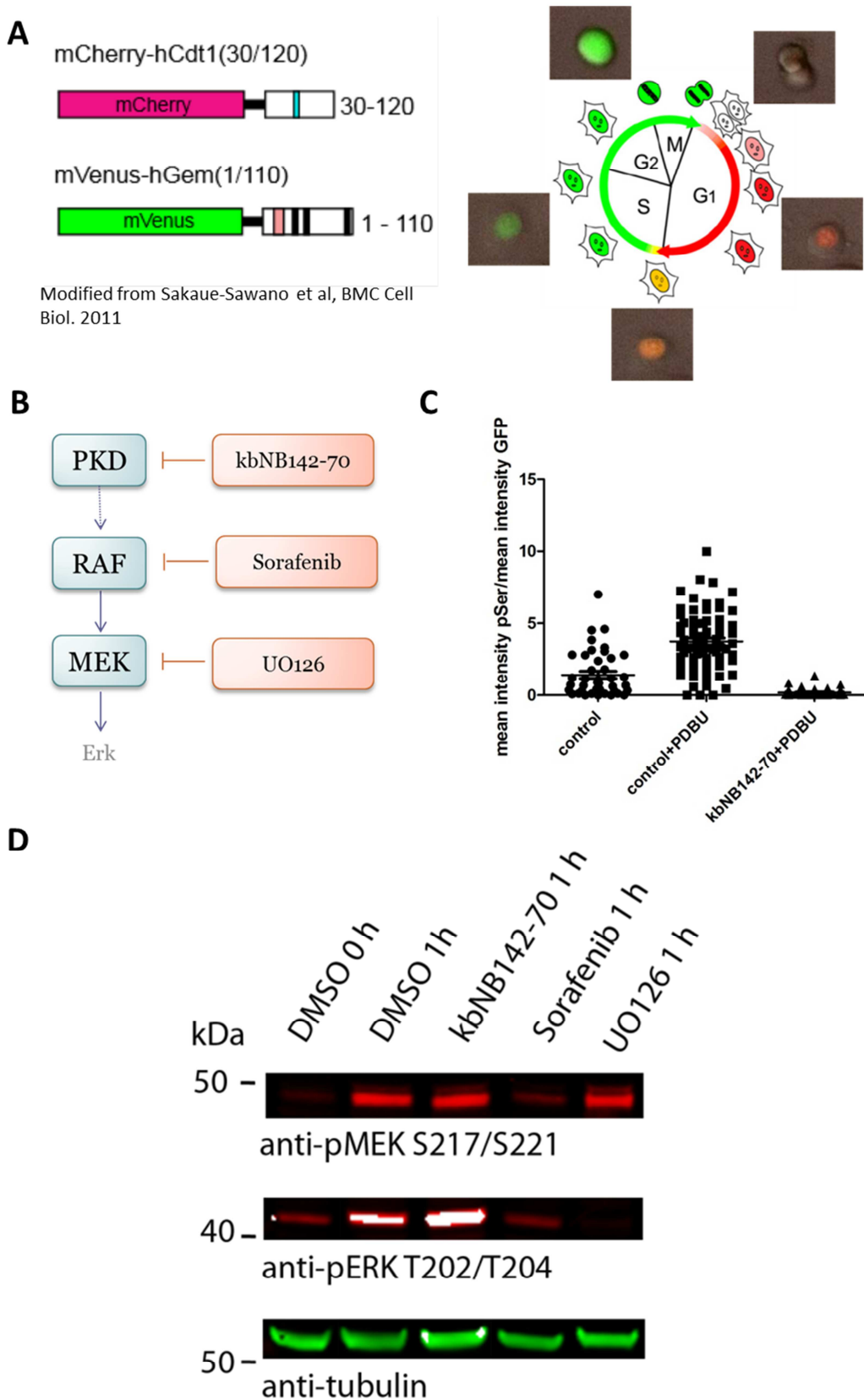
Figure 24 Fucci2-HeLa cells and effectiveness of inhibitors
(A) Left: Fusion proteins used in Fucci2 system. Right: Cell cycle indicator of Fucci2-HeLa cells with live cell image examples of one cell in different stages of cell cycle. (B) Overview of kinase inhibitors used. (C) Fucci2-HeLa cells transfected with the G-PKDrep were left untreated (control), treated with PdBu (control+PDBU) or with a combination of PKD inhibitor and PDBU (kbNB142-70+PDBU), fixed and stained with the pS294-specific antibody followed by Alexa546-coupled anti-rabbit IgG.

Fluorescence intensity of Alexa546 and EGFP was quantified in Golgi regions of transfected cells and the ratio was calculated as described in the material and methods section. 40 to 70 cells were analyzed per condition. Shown is the mean ± SEM. (D) Aphidicolin-synchronized HeLa cells were released from cell cycle arrest and treated with DMSO, kbNB142-70 (5µM), Sorafenib (10 µM) or UO126 (30µM). Cells were lysed at indicated time points after release and protein phosphorylation was analyzed by Western Blotting. MEK and ERK activity was monitored using phospho-specific antibodies and equal loading was verified by probing with a tubulin-specific antibody. LiCor system was used for detection.

At first the inhibitor effectiveness was analyzed. kbNB142-70 is a more potent derivate of the previously used CID755673 (C. LaValle et al. 2010). Because antibodies specific for active, phosphorylated PKD were not suitable to detect the endogenous protein in HeLa cells a different strategy was chosen. A Golgi PKD activity reporter, G-PKDrep (Fuchs et al. 2009), was transiently expressed in HeLa cells. This reporter contains a PKD-specific target sequence fused to EGFP and targeted to the trans-Golgi by the GRIP domain of p230. The phosphorylation of this target sequence at a single serine residue can be measured with a phospho-specific antibody and thus used as readout for PKD activity. Under basal conditions, PKD activity was comparably low (see Figure 24C). However an increase in reporter phosphorylation and hence in PKD activity was observed by stimulation of cells with Phorbol 12,13-dibutyrate (PDBU), which is a known activator of PKD activity (Rozengurt et al. 1995). If kbNB142-70 was added together with PDBU, reporter phosphorylation decreased strongly and was lower than reporter phosphorylation in control cells. This result demonstrates successful inhibition of PKD activity in HeLa cells by addition of 5 µM kbNB142-70 (see Figure 24C).

To verify inhibition of RAF and MEK by sorafenib and UO126, respectively, phosphorylation of the RAF substrate MEK and the MEK substrate ERK was analyzed using phospho-specific antibodies. To do so, HeLa cells were synchronized at the G1/S border and left untreated or treated with the PKD inhibitor kbNB142-70, the RAF kinase inhibitor sorafenib or the MEK inhibitor UO126. One hour after release cells were lysed and phosphorylation of MEK and ERK was monitored as described in 2.2.13. MEK and ERK phosphorylation strongly increased one hour after the release. Sorafenib efficiently blocked MEK and consequently ERK phosphorylation whereas UO126 only blocked ERK phosphorylation. kbNB142-70 had no apparent effect on MEK and ERK phosphorylation (see Figure 24D).

After the effectiveness of the inhibitors was verified, kbNB142-70 and UO126 were selected to investigate the inhibition of PKD and MEK, respectively, on cell cycle progression. First, Fucci2-HeLa cells were treated with the respective inhibitors for 12 hours and the percentage of the cells with a green nucleus (indicative for S/G2/M phase) was determined. The resulting images were quantitatively assayed by a Mat-Lab based software written by Matthias Lorenzen (Institute for Systems Theory and Automatic Control, University of Stuttgart, Stuttgart, Germany). With the help of this automated Fucci image detection tool it was possible to analyze 500-1000 cells per sample. The result is shown in Figure 25A. Asynchronous Fucci2-HeLa cells treated with 10 µM of kbNB142-70 showed an increase of green cells compared to control cells. Consequently, cells treated with kbNB142-70 had a significantly longer S/G2/M phase (see Figure 25A).
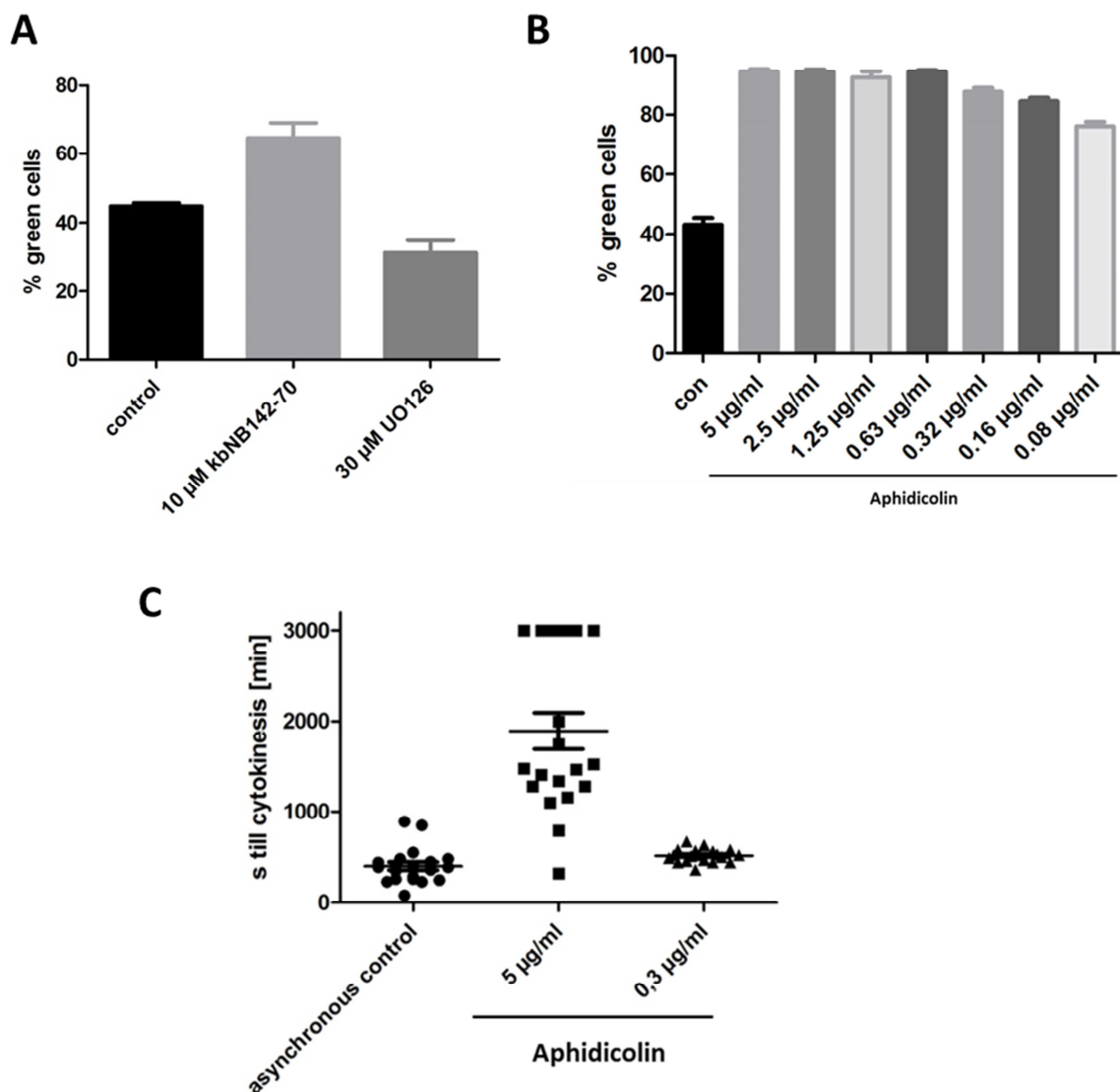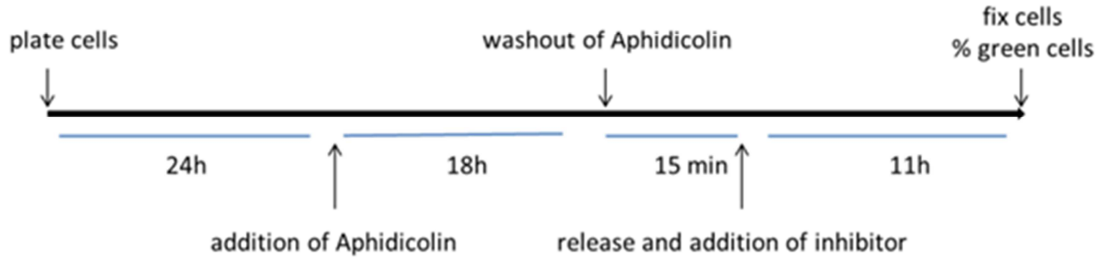
Figure 25 Effects of PKD and MEK inhibitors on asynchronous Fucci2-HeLa cells and synchronization with aphidicolin
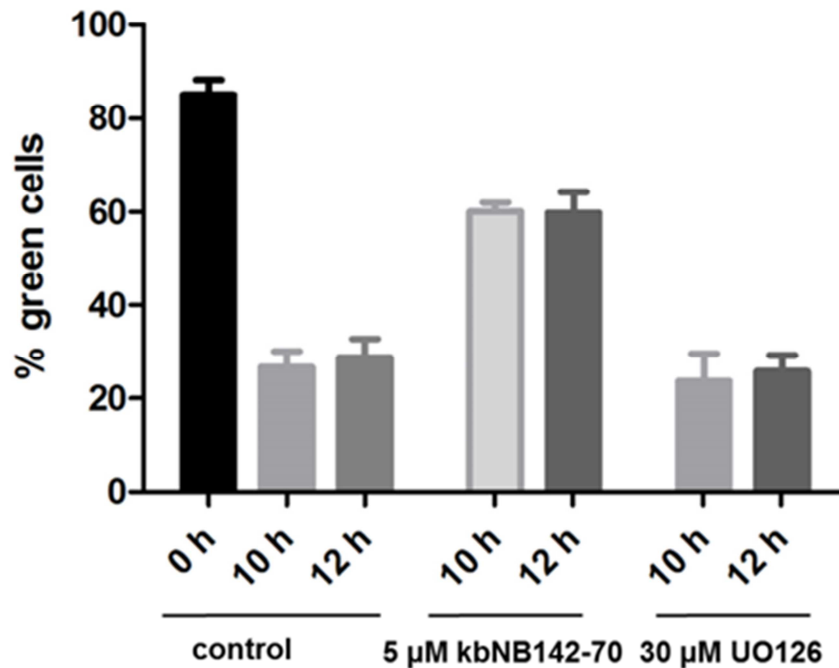(A) Fucci2-HeLa cells were treated with indicated inhibitors for 12 hours, fixed and the amount of green and red fluorescent cells was quantified. % of cells displaying green nucleus, indicative of S/G2/M phase is shown as a mean of three independent experiments ± SEM. In each experiment 5 view fields (< 1000 cells) were analyzed with the Fucci analysis software. (B) Fucci2-HeLa cells were treated with descending concentration of aphidicolin for 18 hours. Cells were fixed and % of green cells was determined with Fucci analysis software. Shown is the mean of five view fields (< 1500 cells) ±SEM. (C) Manual tracking of time cells need to progress through S/G2/M phase in asynchronous cells or after aphidicolin release. 20 cells were tracked for each condition. Shown are single cell results as dots. Mean as line ± SEM. 3000 minutes is the maximum time of observation for the movie.

Cells treated with 10 µM UO126 showed no increase in the percentage of S/G2/M cells after 12 hours of treatment (data not shown). However, in the case of 30 µM UO126 a decrease of cells in S/G2/M phase was observed pointing to a prolonged G1 phase in these cells (see Figure 25A). Because cell cycle transitions are tightly regulated it was necessary to ensure that PKD and MEK activity were specifically inhibited at the beginning of G2 phase but not in G1 phase. To do so, aphidicolin, a DNA-polymerase inhibitor was used to synchronize cells at the beginning of S phase. Treatment with various concentrations of aphidicolin showed that an efficient synchronization was reached at 0.32 µg/ml aphidicolin, evident from a dramatic increase in the amount of green cells from 40% to nearly 90% (see Figure 25B). More importantly, cells treated with this aphidicolin concentration showed a progression time through S/G2/M phase, which was comparable to non-treated cells. On the contrary, cells treated with 5 µg/ml aphidocolin progressed through S/G2/M much slower (see Figure 25C). In sum, treatment of cells with 0.32 µg/ml aphidcolin provided efficient synchronization in S phase combined with a physiological cell cycle progression.

A

B

Figure 26 Effects of PKD and MEK inhibitors on asynchronous Fucci2-HeLa cells
(A) Time-line to analyze effect of inhibitors on synchronous Fucci2-HeLa cells. (B) Fucci2-HeLa cells were treated according to the timeline in C and fixed. % of green cells was determined with Fucci analysis software. Shown is the mean of five view fields (< 400 cells) ±SEM.

Having established the synchronization protocol (see Figure 26A), the effect of PKD and MEK inhibitors on progression of cells through S/G2/M was analyzed. 10 and 12 hours after cells were released from aphidicolin treatment nearly all cells passed through the S/G2/M phase indicated by a decrease of the amount of green cells from 90% down to 30%. A similar behaviour was observed for cells treated with UO126. However, cells did almost not progress through S/G2/M phase in the presence of 5

μM kbNB142-70. Here, 60% of the cells were still in S/G2/M phase compared to 30% in the control pointing to a cell cycle arrest upon PKD inhibition (see Figure 26B). To gain further insight into the fate of single cells during cell cycle transitions, live cell imaging was performed. These data were analyzed with the help of the tracking tool of the Fucci analysis software. After an automated cell detection step and a context based minimization of errors and additional biological rules of detection, the user is able to manually correct residual cell detection errors (see Figure 27A & B).
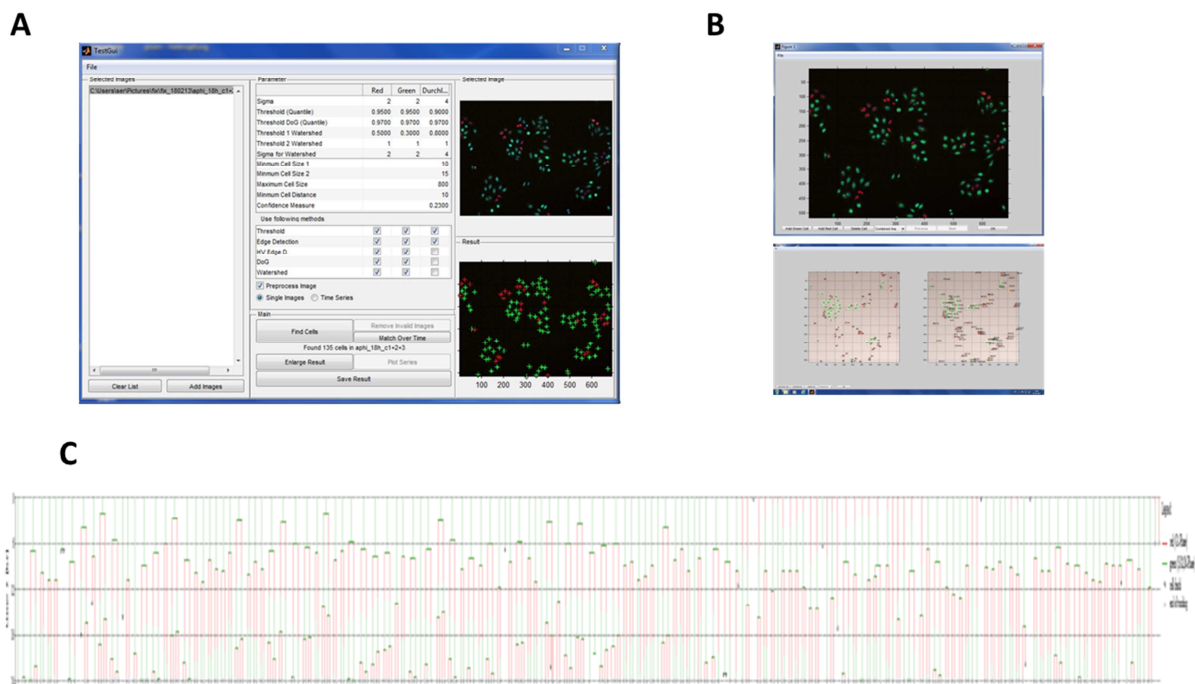
Figure 27 Development of an automated cell detection and tracking software for live cell experiments
(A) Screenshot of user interface of Fucci analysis software. The left part contains the images. The middle part shows the available detection methods. The right part shows original image (upper right) and detected red and green cells (lower right). (B) Screenshot of cell tracking tool of Fucci analysis software. (C) Graphical display of a family tree generated with data of Fucci analysis software tracking tool. Green lines indicate time cell is in S-G2-M phase. Red lines indicate time cell is in G1 phase (for detailed image see supplement 6.3 in electronic version).

This method resulted in nearly 100% correct cell detection, which is necessary for successful tracking of single cell fates. Importantly, the tracking and detection of cell division could be manually corrected at the end of tracking. This semi-automated approach provided a low error frequency combined with timesaving analysis of great amounts of data generated by live cell imaging. An example of tracking a whole population of synchronized Fucci2-HeLa cells upon release on a single cell level over 2 generations is shown in Figure 27C. In a first approach a time resolved population

based analysis was performed. The percentage of cells in S/G2/M phase of a population could be determined continuously over time. At the beginning of the movie the majority of the cells (80 – 90%) displayed a green nucleus indicative of S/G2/M phase. 15 hours later, only 20% of the control cells were still in S/G2/M phase and thus the majority of cells successfully progressed through this phase. Subsequently, the Fucci2-HeLa cells synchronously progressed through further cell cycle phases. Addition of 5 µM kbNB142-70 delayed the progression of cells through S/G2/M dramatically. Specifically, cells were only partially and very slowly progressing through S/G2/M phase. Surprisingly, cells treated with UO126 showed no delay in progression through S/G2/M phase (see Figure28A). The effect of the PKD and MEK inhibitors on progression through S/G2/M phase was also visible on a single cell level (see Figure 28B).
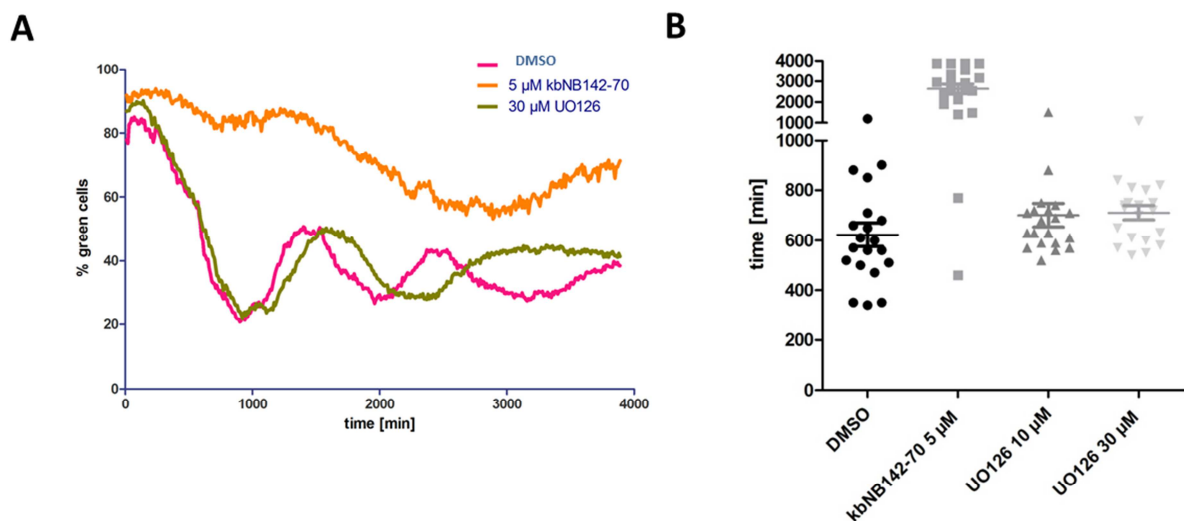
Figure 28 Population and single cell based data from live cell imaging
(A) Population based analysis of live cell imaging of synchronous Fucci2-HeLa cells left untreated (DMSO) or treated with kbNB142-70, UO126. Inhibitors were added immediately after the release from aphidocolin treatment. Imaging was performed over 70 hours. The percentage of green cells was determined by evaluation of microscopic images (timeframe 10 min) with Fucci analysis software. (B) Manual tracking of time cells need to progress through S-G2-M phase after aphidicolin release. 20 cells were tracked for each condition. Shown are single cell results as dots. Mean as line ± SEM.

Kienzle et al showed that depletion of PKD caused a delay in progression through G2 phase. To analyze whether the cell cycle arrest caused by the PKD inhibitor kbNB142-70 occurs in G2 or in S phase, HeLa cells were stained with propidiumiodide and analyzed by flow cytometry. Propidiumiodide binds to double stranded DNA in a stoichiometric manner, i.e. it binds in proportion to the amount of

DNA present in the cell. In this way cells that are in S phase will have more DNA than cells in G1. They will take up proportionally more dye and will fluoresce more brightly until they have doubled their DNA content. The cells in G2 will be approximately twice as bright as cells in G1. Synchronized HeLa cells showed a comparable progression through S phase whether treated with kbNB142-70 or not (see Figure 29). After 4 hours control cells were mainly in G2 with few cells already in G1 again. Cells treated with the PKD inhibitor kbNB142-70 were in G2 phase. 8 hours after release nearly half of control cells already progressed through G2/M, whereas less kbNB142-70 treated cells were in G2 pointing to a delay in this phase (see Figure 29).
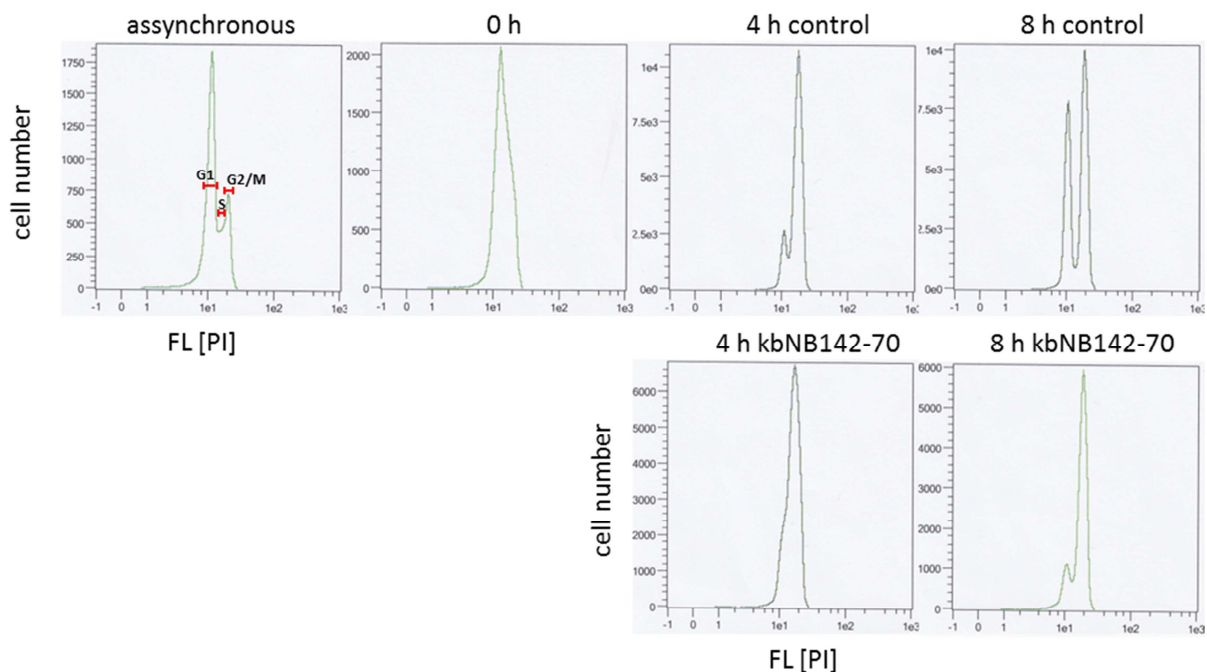
Figure 29 PKD inhibition causes a delay in G2 phase
Flow cytometry analysis of synchronized HeLa cells with aphidicolin were fixed and stained with PI after 0 h, 4 hours and 8 hours release. Assynchronous cells served as control for synchronisation process.

Next it was investigated if the observed delay in S/G2/M progression in kbNB142-70 treated cells was caused by a lack of Golgi fragmentation. Therefore, Brefeldin A (BFA) a Golgi dispersing agent (Fujiwara et al. 1988) was used solely and in combination with kbNB142-70. As Kienzle et al could show that the lack in fragmentation of the Golgi resulted in the delay in progression through G2/M phase Brefeldin A treatment should remove the cause of the delay by dispersing the Golgi. Live cell imaging of synchronized Fucci2-HeLa cells was performed and time of

progression through S/G2/M phase after release was measured. BFA treatment alone showed no difference to control cells with respect to progression of cells through of S/G2/M phase. As expected, kbNB142-70 treatment showed a significant delay in S/G2/M phase progression (C. LaValle et al. 2010). Interestingly, treatment with kbNB142-70 plus BFA resulted in an accelerated progression through S/G2/M phase compared to treatment with kbNB142-70 alone. However, the duration of S/G2/M phase was still significantly higher compared to BFA treated cells, suggesting a Golgi independent role of PKD in S/G2/M phase (see Figure 30A). To analyze the cell cycle transitions in more detail we made use of the fact that Fucci2-HeLa cells detach and show a round phenotype at beginning of metaphase. Therefore, it was possible to analyze the time needed to progress through S/G2 phase till metaphase and subsequently from metaphase till cytokinesis on a single cell level. Indeed, an increase in the duration of the late mitosis phase (metaphase to cytokinesis) was detected in kbNB142-70 treated Fucci2-HeLa cells compared to control cells (see Figure 30B).
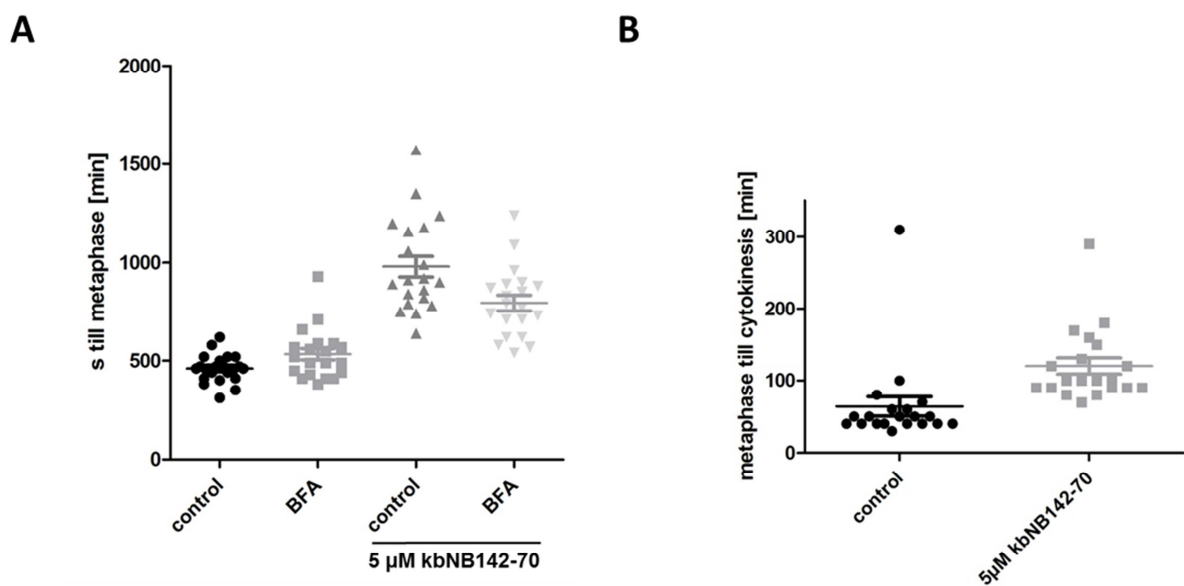
Figure 30 Inhibition of PKD prolonges progression of cells through mitosis
(A) Manual tracking of live cell imaging data. Duration of S till metaphase progression in Fucci2-HeLa cells. n = 20. Each cell is shown as dot plus mean ± SEM (B) Manual tracking of live cell imaging data. Duration of metaphase till cytokinesis is shown. n = 20. Each cell is shown as dot plus mean ± SEM.

The results suggested that PKD controls a pathway important for progression through mitosis. An important part of late mitosis is actin remodelling. A major part of actin remodelling takes place when the contractile ring is formed to separate the

mother from the daughter cell. One important player of this process is the actin depolymerisation factor cofilin (Kaji 2003).

Cofilin activity is tightly regulated by a network of kinases and phosphatases that thus coordinate the initiation of actin polymerization. Cofilin activity depends on its phosphorylation state: On the one hand, phosphorylation at serine 3 by the LIM kinase (LIMK) family (LIMK1 and LIMK2) and the related testicular protein (TES) kinases turns off the actin-binding activity of cofilin and thus leads to inactivation. On the other hand, dephosphorylation by the SSH as well as chronophin phosphatases results in reactivation of the actin binding activity of cofilin (reviewed in Olayioye et al. 2013). Notably, PKD negatively controls cofilin activation on multiple levels. A prominent example is the direct phosphorylation and inactivation of SSH (Eiseler et al. 2009; Peterburs et al. 2009).

Thus, pharmacological inhibition of PKD renders cofilin more active. This could hamper the establishment of the contractile ring. Analysis of mitotic events in a population is problematic due to the relative short duration compared to whole cell cycle events. To specifically analyze late mitosis progression, Fucci2-HeLa cells were synchronized by a Thymidin-Nocodazole block at the beginning of M phase (Ma & Poon 2011). Cells were released from this block in the presence or absence of kbNB142-70, lysed and analyzed for cofilin phoshorylation. Interestingly, the phosphorylation level of cofilin was decreased in cells treated with kbNB142-70 (data not shown), pointing to an increased cofilin activity in these cells. To investigate whether the enhanced cofilin activity in kbNB142-70treated cells could affect the formation of the contractile actin ring and thus cytokinesis HeLa cells, stably expressing Lifeact, a 17-amino-acid peptide, which stains filamentous actin, were generated. Expression of Lifeact and thereby actin dynamics were observed in live cell imaging. However, it was not possible to detect a clear difference in formation of the contractile ring between control cells and cells treated with kbNB142-70 (data not shown). The observation of contractile ring formation and actin dynamics is a challenging task because of the highly dynamic nature of this ring and thus requires analysis in 3 dimensions in a high temporal and spatial resolution. Future studies are thus necessary to enlighten the role of PKD in late mitosis in general and the formation of the contractile ring in particular.

Kienzle et al also showed that the PKD-mediated Golgi fragmentation is dependent on the RAF/MEK/ERK pathway. Thus, the influence of PKD, RAF and MEK inhibitors on the MAPK pathway in S/G2/M phase was investigated. To do so, aphidicolin synchronized HeLa cells stably expressing PKD1-GFP were released and left untreated or treated with the different inhibitors for 1 hour, 5,5 hours, 8,5 hours, and 10 hours. Of note, overexpression of PKD1-GFP in these cells did not affect cell cycle progression (data not shown). Because the commercially available pMEK antibodies were not suitable for immunofluorescence analysis, Western blot analysis of MEK and ERK phosphorylation was performed instead. Additionally, PKD1-GFP phosphorylation was monitored as well.

In control cells an initial rise in phosphorylation was seen 15 minutes after release. This strong phosphorylation of PKD1-GFP, MEK and ERK decreased towards 5,5 hours release time and stayed at comparably low levels till 10 hours after release (see Figure 31A & B). Treatment with the PKD inhibitor kbNB142-70 did not alter this phosphorylation behaviour drastically. However, a slight increase in duration of elevated pPKD, pMEK and pERK was seen (see Figure 31A & B). Sorafenib had no effect on pPKD or pERK levels but diminished phosphorylation of MEK. Treatment with the MEK inhibitor UO126 did not alter pPKD levels but showed a strong feedback of ERK on RAF kinase, visible by the increase in MEK phosphorylation, in cells treated with the MEK inhibitor UO126 (see Figure 31A & B).

A quantification of data created by enhanced chemoluminescence is difficult because of the non-linear signal. Therefore, samples were analyzed using the LiCor detection system. This system is based on infrared dyes, which provide signals linear to the quantity of antibody that is bound.
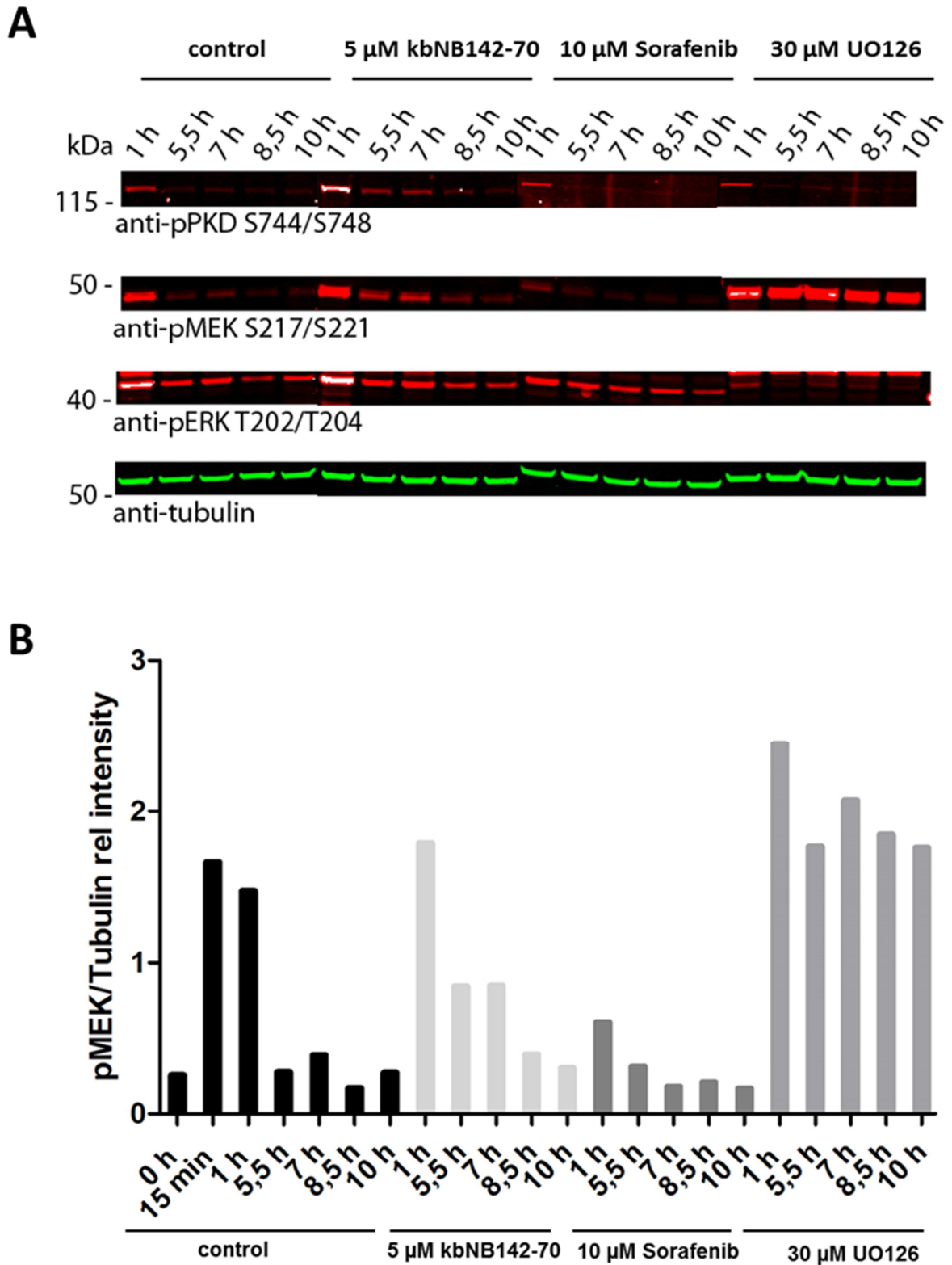
Figure 31 Effects of inhibitors on RAF-MEK-ERK pathway
(A) Aphidicolin-synchronized HeLa cells were released from cell cycle arrest and treated with DMSO, kbNB142-70 (5µM)), Sorafenib (10 µM) or UO126 (30µM). Cells were lysed at indicated time points after release and protein phosphorylation was analyzed by Western Blotting. PKD, MEK and ERK activity was monitored using phospho-specific antibodies and equal loading was verified by probing with a tubulin-specific antibody. LiCor system was used for detection. (B) pMEK and tubulin mean intensity of each band was quantified using ImageJ. Relative intensity of pMEK/tubulin is shown.

To study the influence of PKD-, RAF-, and MEK-activity inhibiting agents on the MAPK pathways, mechanistic dynamical models have been used. These models have been developed in cooperation with Jan Hasenauer (Institute of Computational Biology, HelmholtzZentrum München, München, Germany).
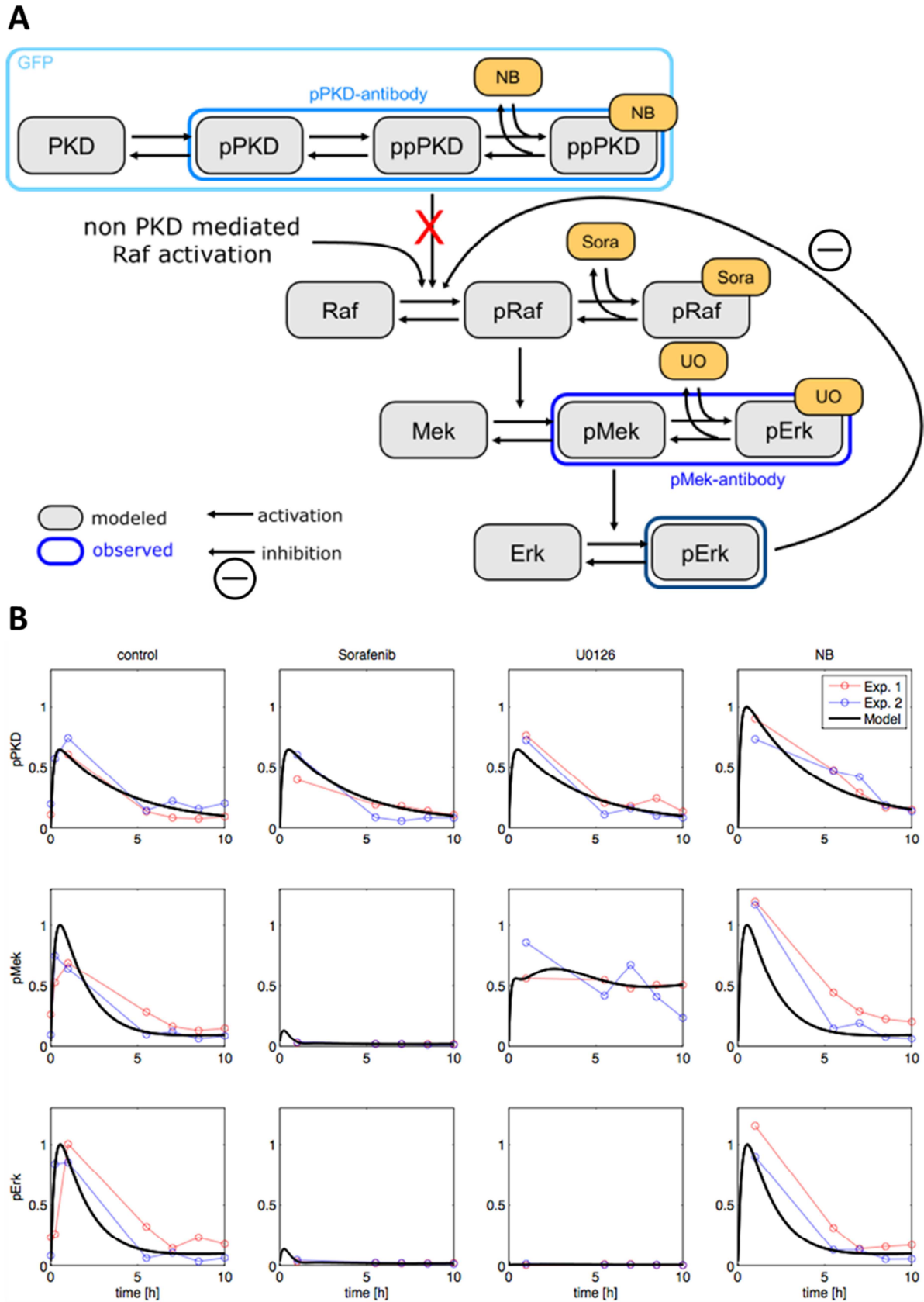
Figure 32 Mathematical model describing the influence of ERK and PKD activity on cell cycle
(A) Structure of mathematical model. Blue bars represent observed data (B) Fit for Model M5 with two experiments. Model (black line), experiment 1 (red line), experiment 2 (green line). Figure by Jan Hasenauer.

In total 8 different model structures and hypothesis were considered. These models were compared using the Akaike information criterion, and the Akaike weights of each model have been computed. The best model (M5) possessed a strong feedback from ERK to RAF and an alternate activation mode for RAF apart from the PKD controlled activation (see Figure 32A &B). In a model comparison it resulted in a 92.7 % probability of the model using AIC weights (H. Akaike 1973) (see Figure 33A) and a similarly high probability using BIC weights (Schwarz 1978) (see Figure 33B).
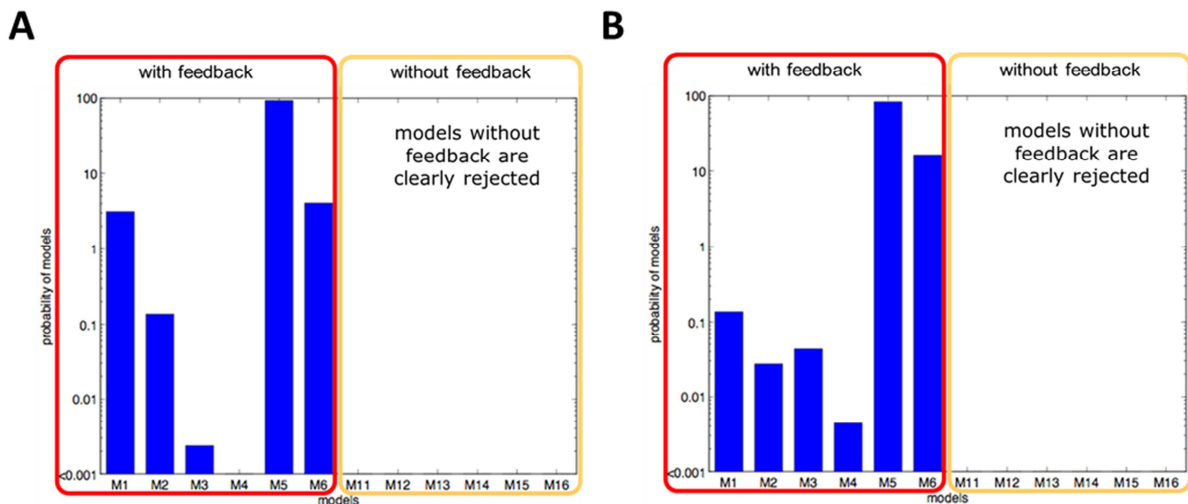
Figure 33 Model Comparison
(A) Model Comparison using AIC weights. (B) Model Comparison using BIC weights. Figure by Jan Hasenauer.

This verifies the hypothesis, that PKD exerts its strong effect on HeLa proliferation primarily via a RAF/MEK/ERK independent pathway.

Statistical evaluation, in cooperation with Jan Hasenauer (Institute of Computational Biology, HelmholtzZentrum München, München, Germany), of the tracking data obtained with Fucci2-HeLa cells verified the observation that inhibition of PKD by kbNB142-70, but not inhibition of MEK by UO126, delayed progression through G2/M phase (see Figure 34). A statistically significant increase in length of s-phase -till cytokinesis duration between control and kbNB142-70 treated cells was found (p < 0.001). No statistically significant increase in length of s-phase -till cytokinesis was found between control cells and UO126 treated cells (p = 0.53).
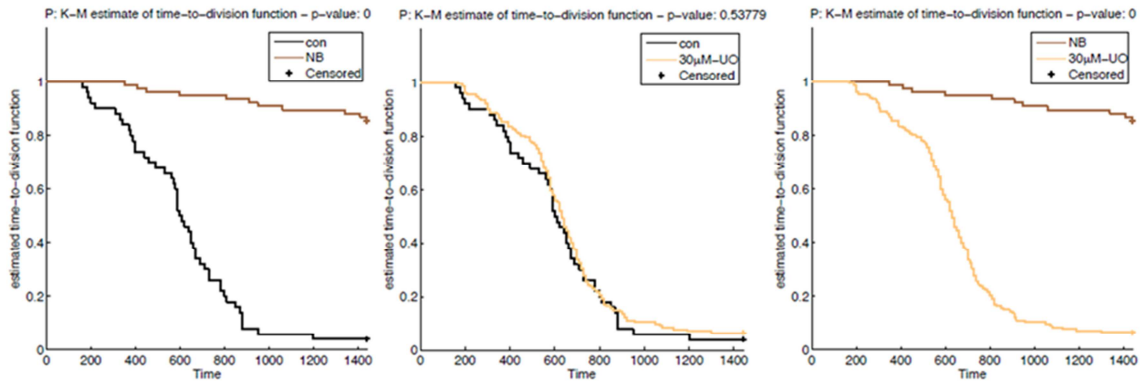
Figure 34 Statistical evaluation of time to first division
K-M estimate of time to division function between control and kbNB142-70 treated Fucci2-HeLa cells (left), control and UO126 treated Fucci2-HeLa cells (middle), and kbNB142-70 treated HeLa cells against UO126 treated Fucci2-HeLa cells (right).

The in-depth single cell data obtained by tracking whole populations in time lapse movies will be used to generate a computational model describing heterogenic proliferation behaviour of cell populations (Jan Hasenauer, Helmholtz-Zentrum München).

Additionally, dose response curves were made to correlate the quantitative signal pathway data with the tracking data. Interestingly, the effect of kbNB142-70 was concentration dependent. As already shown earlier 5 µM kbNB142-70 induced a complete block in cell cycle progression. Lower concentrations of the inhibitor delayed cell cycle progression still significantly (3 µM) or did not affect this process at all (1 µM) (see Figure 35A). To investigate the role of RAF kinase in this pathway, a clinically used inhibitor, sorafenib was also used in live cell imaging. RAF inhibition by 7 µM sorafenib also caused a delay in S/G2/M progression in Fucci2-HeLa cells, however, 3 µM and 5 µM sorafenib did not dramatically delay the cell cycle (see Figure 35B).
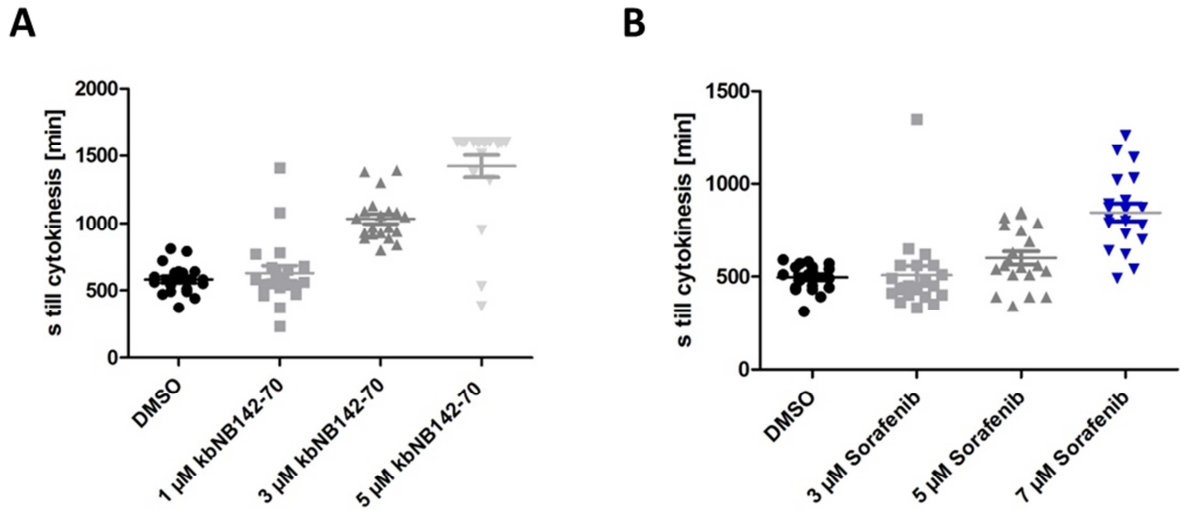
Figure 35 Titration of PKD and RAF inhibitor
(A) Manual tracking of live cell imaging data. Duration of s -till cytokinesis in Fucci2-HeLa cells. n = 20 cells, shown. Each cell is shown as dot plus mean ± SEM.

However, sorafenib is known to have various other targets and therefore these data will not be used in a future correlation analysis of the proliferation data and the quantitative signal pathway data.

In summary, the data demonstrate that PKD but not MEK or ERK activity, are required for progression of HeLa cells through S/G2/M phase.

4. Discussion

4.1.　　Basic Characteristics of human and mouse MSCs

Stem cell research has gained many promising insights and advancements. However the therapeutic benefit at present is mainly restricted to one adult stem cell group, the hematopoietic stem cells. Here, nearly 5 decades of hand in hand collaboration between clinical- and bench work science has led to safe and successful therapies of severe pathologies. Only in the last decade the potential for treatment with other adult stem cell subsets as for example the mesenchymal subset is under investigation. The first step towards a safe and successful therapy with MSC is the understanding of differentiation and proliferation control in these cells.

Therefore, at the beginning of this work hMSC from two different sources were investigated. The cells were characterized according to the three criteria by the International Society of Cellular Therapy (ISCT) (Dominici et al. 2006). First, MSCs must be adherent to plastic under standard tissue culture conditions. Second, MSCs must express certain cell surface markers, such as CD73, CD90, and CD105, and lack expression of other markers, including CD45, CD34, CD14, or CD11b, CD79alpha or CD19, and HLA-DR surface molecules. Finally, MSCs must have the capacity to differentiate into osteoblasts, adipocytes, and chondroblasts under in vitro conditions. The characterization could confirm all of these criteria for BM and UC-hMSC. Still, these criteria are based on the phenotype of culture-expanded MSCs and are not enough to guarantee safety in clinical applications.

Several reports show that source specific differences exist in MSC populations (Kern et al. 2006; Chen et al. 2009; Cheng et al. 2010). Despite the fact that hMSC from both sources showed expression of the marker panel described by the ISCT, different expression of other markers was found in this work. Expression of two surface antigens, namely CD56 and CD173, was only detected on UC-MSC and not on BM-MSC. On the contrary, expression of GD2 and W8B2 was restricted to BM-derived MSC. Noteworthy, two reports suggest that the neural ganglioside GD2 would be a sufficient marker for MSC as its expression in BM, adipose tissue (Martinez et al. 2007) and UC (Xu et al. 2009) was restricted to MSC of these sites.

However, Xu et al stated that expression of GD2 is restricted to a small subset of low passage UC-MSC providing a potential explanation for the lack of GD2 expression on UC-MSC identified in this work.

Differences in surface marker expression may indicate that, even though these cells show comparable differentiation behaviour in vitro, functional differences and diverse differentiation potential may exist. Of note, the finding of Chen et al. that MSC from UC have a higher proliferative potential in vitro could be verified (Chen et al. 2009). Nevertheless a major problem for the sufficient expansion of hMSC is the observed senescence after few passages in vitro. In order to use ex vivo expanded cells in cellular therapies especially control of proliferation and hence cell cycle pathways have to be thoroughly understood.

In this work the influence of PKD and members of the MAPK pathway on the cell cycle of BMSCs was investigated. The analysis was performed on a population and on a single cell level in mouse BMSCs, because these primary cells overcome the initial senescence by spontaneous immortalization. This phenomenon of spontaneous immortalization has been reported before and is known for rodent cells (Hornsby 2003). Parrinello et al. could show that atmospheric oxygen induces oxidative stress in primary mouse fibroblasts resulting in senescence (Parrinello et al. 2003). Primary murine embryonic fibroblast (MEF) can bypass the proliferation block by a spontaneous acquisition of a p53 mutation. This allows outgrowth of the cell that lost function of the tumor suppressor and expansion of the subpopulation into an immortalized cell line (Hahn & Weinberg 2002; Zindy et al. 1998). Indeed, immortal MEF lines typically harbour either a p53 mutation or loss of p19 (Harvey & Levine 1991). Accordingly, Phinney and colleagues could show that, under atmospheric oxygen, the poor growth and growth arrest of primary BMSCs is due to oxidative stress and is p53 dependent (Boregowda et al. 2012). Indeed, we could also detect high levels of p53 in early, mid-, and late-passage mBMSC M2 cells, indicating that accumulation of p53 is most likely due to a loss-of-function mutation. Of note, the loss of p53 function is necessary for spontaneous cellular immortalization but not sufficient to induce malignant transformation.

In line with this, late-passage M2 cells did not form tumors when subcutaneously injected in nude mice (data not shown) nor showed anchorage-independent growth indicating that malignant transformation did not occur.

To date, there is no agreement on a unique marker panel that characterizes cultured mBMSCs. The variances detected in surface antigen expression are likely due to different methods of isolation, cultivation, as well as the different genetic backgrounds of the mouse strains used. Additionally, recent studies demonstrate the existence of different subsets of stromal cells in mouse BM in vivo (Chan et al. 2013). However, several markers have been recently proposed to identify adult MSCs. For example, a subset of Sca1/PDGFRa-positive mBMSCs were able to differentiate in the adipogenic, chondrogenic, and osteogenic lineages. When transplanted into mice, these cells differentiated into osteoblasts and adipocytes (Morikawa et al. 2009). Further, it was demonstrated that nestin expression defines a pool of cells that display BMSC characteristics in vitro and in vivo and support the hematopoietic niche in vivo (Méndez-Ferrer et al. 2010). The transcription factor Mx1 was described as a marker of a subpopulation of BMSCs, which are tripotent in vitro but restricted to the osteogenic lineage in vivo (Park et al. 2012). Most of the surface markers expressed on the stromal cell line M2 have been described by others using mouse MSCs (CD29+CD44+CD105+ CD106+ Sca1+) (reviewed in (Boxall & Jones 2012)).

Additionally, we could show that the stromal cell line M2 expresses Runx2, the master regulator of osteogenesis (Karsenty 2008), and that the loss of this transcription factor impedes osteogenesis in vitro. This is in line with findings that BMSC cultures have a stable expression of Runx2 (Park et al. 2012). Noteworthy, osteogenic markers, such as osteopontin and lbsp, are expressed in the stromal cell line M2. This is especially interesting because expression of lbsp has been proposed to be a predictor of osteogenic capacity in vivo (Satomura et al. 2000). In vivo transplantation of stromal cells verifies their osteogenic capacity by the formation of bone (Krebsbach et al. 1997; Krebsbach et al. 1998). In the past, several BM-derived MSC lines of mouse origin have been established; however, only some studies demonstrated the generation of bone upon transplantation of cells in mice (see Table 12).

Table 12 overview of BM derived MSC lines in literature

BM-derived MSC line (reference)	Generation of bone upon transplantation
(Satomura et al. 2000)	+
(Diduch et al. 1993)	-
(Dennis et al. 1999)	+
(Arakawa et al. 2000)	-
(Allan et al. 2003)	-
(Juffroy et al. 2009)	+
(Negishi et al. 2000)	-
(Takeshita et al. 2001)	-
(Liu et al. 2009)	+

BMC9 cells are conditionally immortalized and, upon subcutaneous implantation on a carrier of porous calcium phosphate ceramics, they formed bone in nude mice (Dennis et al. 1999). D1 cells, isolated from a Balb/C mouse, spontaneously differentiated into osteoblasts in vitro and formed vascularized bone without the presence of additional scaffold material (Juffroy et al. 2009). Satomura et al. established five clonal stromal cell lines and three of these clones formed bone in vivo (Satomura et al. 2000).

It has been reported that transplantation of BM stroma generates bone and establishes the hematopoietic environment at these sites (Latzinic, N V. et al. 1979). Other studies revealed that the ability to generate bone tissue in vivo does not necessarily correlate with an establishment of hematopoiesis (Sacchetti et al. 2007). To our knowledge, the formation of hematopoiesis- accommodating bone upon transplantation of a stable mouse stromal cell line described here was not demonstrated so far.

A unique feature of the M2 cell line described here, namely CD146 expression, is in accordance with its hematopoiesis-inducing activity and resembles the phenotype of human skeletal stem cells. Thus, high expression of CD146 distinguishes human BM stromal stem cells (skeletal stem cells) from other osteogenic progenitors and is a prerequisite for these cells to form bone and support hematopoiesis in vivo (Sacchetti et al. 2007). In line with this, CD146-positive cells could be identified in perivascular adventitial positions close to venous sinusoids but also as scattered fibroblasts in the marrow cavity in sections of human trabecular bone (Rasini et al. 2013).

Mouse-BM-derived CD146+CD105+ cells have been recently shown to possess osteogenic potential in vivo, supporting the specific role of CD146+ cells for murine osteogenesis, too (Tasso et al. 2013). Other studies using mouse BM tissue provide further evidence that a subset of CD105+CD90- skeletal progenitors initiate formation of ectopic bones with marrow cavities containing hematopoietic stem cells (Chan et al. 2009; Chan et al. 2013). Of relevance, the multipotent M2 cell line expresses CD146 and CD105 at high levels in early, mid, and late passages but lacks the expression of CD90. The expression profile of the early and late-passage M2 cells is thus in line with their capacity to form heterotopic ossicles and BM in nude mice. However, whether expression of CD146 and/or CD105 is of functional relevance and a prerequisite for the formation of the hematopoietic tissue clusters in vivo presently remains an open question. This can now be addressed with the M2 cell line by experimental silencing of the respective genes.

In vivo models for bone regeneration have been applied to small and large animals (Kleinschmidt et al. 1993; Hollinger & Kleinschmidt 1990). For example, engineered constructs have been successfully used in small-animal, nonunion critical-sized femur defect models (Kon et al. 2000; Marcacci et al. 1999). Cell based approaches to bone regeneration are in clinical use and results of pilot trials are promising (reviewed in Jones & Yang 2011; Tare et al. 2010); however, the repair of large bone defects requires huge quantities of BM-derived stromal progenitor cells expanded in vitro. Alternatively, the application of growth factors and antagonists of CXCR4 inducing in vivo stem cell mobilization is discussed as a promising approach for bone healing (Kumar & Ponnazhagan 2012). In both cases, a substantial understanding of skeletal stem cell biology is prerequisite for routine clinical use. The cell line described here now provides a model to experimentally approach these issues.

In conclusion, the multipotent M2 cell line established here is a murine stromal cell line harboring skeletal stem cell properties in vitro and in vivo, evident from heterotopic bone formation and induction of hematopoiesis. Long-term proliferation potential under retention of a stable phenotype and multipotent differentiation capacity indicate that this cell line is a versatile tool to study tissue-specific differentiation pathways in vitro and verify/falsify these findings in vivo, thus complementing the scientific questions that can be addressed with human MSCs. As

shown here, M2 cells are a useful model to study in detail osteogenesis in vivo, thereby aiding to improve current therapeutic strategies in bone regeneration.

4.2. Cell Cycle Control in Bone Marrow Stromal Cells

Human and mouse BMSC comprise a very heterogeneous population when cultured in vitro (Bianco et al. 2001). Specifically, the cells showed heterogeneous characteristics concerning their differentiation behaviour as well as their proliferation behaviour. This indicates differences in cell cycle control between single cells. Moreover, this may provide an explanation why clinical trials with cultured MSC show conflicting outcomes, as the ex vivo expansion protocols are not standardized, hence the therapeutically active cell population varies between single trials (Phinney 2012). Indeed, in this work a considerable heterogeneity was detected in Fucci-mBMSCs concerning their G1 and S/G2/M phase length measured by live cell imaging. Although these cells do not resemble the in vivo situation of human or even mouse BMSCs because of the genetic alterations they experienced during the immortalization important knowledge is obtained from the cell cycle analysis on a single cell level.

Surprisingly, not all Fucci-mBMSCs displayed red or green fluorescence. According to Sakaue-Sawano and colleagues the expression of both, mKO2-hCdt1 and mAG-hGem, is controlled by the constitutive active CAG promoter and thus present in every somatic cell. Accordingly, in double transgenic mice generated by crossing the mKO2-hCdt1 transgenic line with the mAG-hGem transgenic line every somatic cell nucleus should exhibit either red or green fluorescence. However, the red and green signals appear to be well balanced at the embryonic stage, but the overall ratio of green-to-red signal decreases as the mice grow (Sakaue-Sawano et al. 2008). This suggests that the expression pattern of the two fluorescently labelled cyclins may change over the lifetime of a mouse. Importantly, the Fucci-BMSCs were isolated from an adult animal. Additionally, it is possible that the spontaneous immortalization of Fucci-BMSCs may result in loss of the fluorescent proteins in a part of the population. However, freshly isolated Fucci-BMSCs not subjected to the spontaneous immortalization already showed only a fraction of fluorescently labelled cells. This cannot be explained by the fact that these cells are in G0, as Cdt1 is also expressed in this phase (Oki et al. 2014).

In addition it was observed that a small part of the non-fluorescent cells were dividing as well in live cell imaging, excluding that these cells are in a non-active cell cycle state (data not shown). Another possibility could be that although the CAG promoter is thought to be active in all tissues (Okabe et al. 1997) and thus also in BM, not all cells present there show fluorescence. For example, a subset of T cells and blood cells was shown to lack detectable fluorescence (Okabe et al. 1997). Moreover, a comparison between the CAG promotor and the ROSA26 BAC expression system revealed that only a part of BM cells showed fluorescence in CAG promoter mice (Giel-Moloney et al. 2007). Interestingly, isolation of Fucci-MEF also resulted in a heterogeneous population concerning the expression of mKO2-hCdt1 and mAG-hGem (see 3.4).

As there were no functional differences detected in cells derived from Fucci compared to wild type strains, it can be concluded that the heterogenous expression of the fluorescent markers did not impact the cell cycle progression and the effect of the inhibitors on this process.

Pharmacological inhibition of PKD by CID755673 led to an accumulation of Fucci-BMSC in the green phase, indicating a prolonged S/G2/M phase. This was accompanied by a reduced number of cells harbouring a fragmented Golgi complex compared to control cells in S/G2/M. Interestingly, the prolonged S/G2/M phase was not observed when cells were treated with UO126, a specific MEK inhibitor. However, the number of cells with a fragmented Golgi still decreased in this case compared to control cells in S/G2/M. These findings verify findings of Kienzle et al, who detected a prolonged S/G2/M phase upon depletion of PKD1 and 2 in HeLa cells and are in accordance with the observation that expression of active MEK in PKD depleted cells rescued the Golgi fragmentation but not cell cycle progression (Kienzle et al. 2013). This suggests an alternate effect of PKD in cell cycle control, which is independent of Golgi fragmentation. Live cell imaging of asynchronous Fucci-BMSC revealed that inhibition of MEK prolonged both phases, G1 and S/G2/M. However, the enhanced cell deaths observed when using the MEK inhibitor UO126 in Fucci-BMSC may suggest an unspecific toxic effect that causes the delay in cell cycle progression in both phases.

To further investigate the role of PKD in cell cycle various synchronization methods were tested. Unfortunately, Fucci-BMSCs did not tolerate the synchronization potentially because the DNA was damaged irreversibly. In future experiments lower concentrations of aphidicolin as described in 3.5 should be tested.

In summary, Fucci-BMSCs are a promising tool to monitor the specific changes in proliferation and cell cycle control that come along with the decrease and sequential increase in growth rate when BMSCs are isolated and cultured under atmospheric oxygen conditions. Results obtained with these cells may provide strategies of how to standardize and control the process of ex vivo expansion in scientifically used mouse MSC and therapeutically used human MSC. Especially the possibility to analyse adult stem cells on a single cell level is very promising. This was shown, for example, in Fucci human pluripotent stem cells. Here, the single cell analysis revealed that stem cell capacity of differentiation varies during the progression of cell cycle (Pauklin & Vallier 2013). This finding shows how important it is to understand cell cycle control and getting new insights in the mechanisms synchronizing differentiation and proliferation in stem cell populations.

4.3. Cell cycle control in HeLa cells

To address general questions of how PKD and members of the MAPK pathway control the cell cycle the more robust cell line HeLa was used. In-depth understanding of cell cycle control is not only helpful for increasing safety and efficacy of stem cell based therapies. It is also important for understanding several pathologies, most of all cancer. There even is a dual gain of insight. First, the initial changes in cell cycle regulation, which give rise to a cancerous cell, could be identified. Secondly, research on cell cycle regulation in cancer cell lines may identify new proteins that can be targeted to prevent proliferation of cancer cells in patients.

The second generation of the Fucci system uses brighter dyes. This makes it possible to use an automated detection for single images and a semi-automated approach for tracking of time series. Importantly, all cells of Fucci2-HeLa exhibit fluorescence. As no commercially available software is specialised on detection of two cycling fluorescent colours, a Mat-Lab based software tool was designed in

cooperation with Matthias Lorenzen (IST, University of Stuttgart). Given the initial conditions such as different confluences or slight variances in signal strength excellent detection rates ≥ 98% were achieved in single images. However, this detection rate is not sufficient for fully automated tracking because already 0,5 % error in detection in every single image of a time series would add up to completely incorrect tracking data. Therefore, a semi-automated approach was chosen in which the user is able to correct detection errors step-by-step resulting in a time efficient tracking result with high accuracy.

Treatment with the DNA polymerase inhibitor aphidicolin reversibly synchronizes cells at the beginning of S phase. When using synchronization methods to investigate effects of inhibitors during release of the cells it is necessary to analyze whether the synchronization method itself compromises the release behaviour. Thus, in this work an aphidicolin concentration, which did not affect the progression through S/2/M phase, was chosen for all experiments. Of note, Fucci2-HeLa cells tolerated the aphidicolin synchronization well in contrast to Fucci-BMSC. This may be explained by a greater robustness of these cells. However, genomic and transcriptomic studies showed that HeLa cells, because they are of cancer origin and/or cultured in vitro for decades, show alterations in pathways regulating the cell cycle (Landry et al. 2013). This has to be taken into account, when interpreting the results obtained with the Fucci2-HeLa cell line.

Surprisingly, a new derivate of the PKD inhibitor CID755673, kbNB142-70, induced a very strong delay and partially even a block in progression through S/G2/M phase in asynchronous and synchronous Fucci2-HeLa cell populations. Noteworthy this inhibitor possesses similar specificity characteristics but increased potency compared to CID755673 (C. LaValle et al. 2010). In line with this, Tandon and colleagues demonstrated that a new generation PKD inhibitor, 1-NA-PP1, induced a growth arrest in G2/M phase in prostate cancer cells. This growth arrest was rescued by overexpression of PKD1 or PKD3 (Tandon et al. 2013). Therefore, it is unlikely that off target effects are responsible for the delay in S/G2/M progression upon kbNB142-70 treatment of HeLa cells. Moreover, a delay specifically in G2 was verified by PI staining in this work (see Figure 29) and by Tandon and colleagues (Tandon et al. 2013).

The inhibition of MEK by the specific inhibitor UO126 induced a prolonged G1 phase in asynchronous HeLa populations. This effect is well expected as the MAPK pathway has many functions in regulating basic growth in eukaryotic cells. However, a lag in progression through S/G2/M phase was not detected, neither in asynchronous nor in synchronous populations upon treatment with UO126. On the contrary, Feinstein and Linstedt reported a delay in mitotic entry in HeLa cells synchronized with a double thymidine block and treated with UO126 (Feinstein & Linstedt 2007). However, in this work detailed single cell analysis of whole cell populations could not confirm this observation. At date, this discrepancy cannot be explained.

The in-depth single cell analysis also revealed a dose dependent delay through progression of S/G2/M phase upon treatment of HeLa cells with kbNB142-70. A similar dose dependent delay was seen in case of treatment with the RAF kinase inhibitor Sorafenib. This would support the hypothesis that mitotic entry is controlled through a RAF kinase dependent but MEK independent pathway. However, Mielgo and colleagues, who propose the existence of such a pathway in some cancer cells, showed that cells are only arrested by the allosteric RAF kinase inhibitor KG5 but not by ATP-competitive inhibitors such as Sorafenib (Mielgo et al. 2011). Additionally, recent studies demonstrated that Sorafenib also inhibits a number of receptor tyrosine kinases that possess threonine at the gatekeeper site, and that inhibition of these targets, rather than RAF kinase, is likely to underlie its clinical efficacy (Wilhelm et al. 2004). Moreover, the wide unspecific inhibition of several other kinases of which some are important for cell cycle regulation such as p38α, MAPK or Aurora kinases (Fu et al. 2007) strengthen this hypothesis (Bain et al. 2007). The delay in progression through S/G2/M in Fucci2-HeLa cells is thus more likely an off-target effect of the broadly kinase inhibiting agent Sorafenib. Therefore, future experiments with more specific inhibitors would be needed to clarify the role of RAF kinase in cell cycle control. However, alternate experimental approaches are necessary because so far RAF-inhibitory compounds without associated off-target effects have not been developed (Bain et al. 2007).

In summary, only inhibition of PKD resulted in a drastic delay in progression through S/G2/M phase in Fucci2-HeLa cells. Because this effect was also observed in other in vitro studies, PKD-specific inhibitors have been developed and were successfully

tested for their ability to treat prostate and pancreatic cancer in mice, making PKD an attractive therapeutic target (C. R. LaValle et al. 2010). However, Ellwanger et al stated that systemic inhibition of PKD in vivo can be a double-edged sword: They remarked, that inhibition of PKD activity in pancreatic beta cells will result in diminished insulin secretion and could thus aid in development of diabetes. On the other hand they proposed that PKD inhibition in the heart could reduce cardiac hypertrophy and failure. Therefore they concluded, that future strategies should focus on a local, organelle and tissue-specific PKD inhibition (Ellwanger & Hausser 2013).

4.4. Population vs single cell based analysis reveals Golgi-dependent and independent functions of PKD during cell cycle

The effect of several inhibitors on progression through G1 and S/G2/M phase was assayed on population and single cell level. HeLa cells display an inert heterogeneity in progression through these phases when single cells are analyzed (see Figure 28B). This may be explained by a finding of Landry and colleagues, who did karyotyping in single cells and found that there is a core set of structural aberrations shared between the majority of cells in this population, as well as a set of rare events only observed in single cells. They stated that rare events did not seem to manifest themselves in significant proportions of the population, since they did not find indications for the presence of subpopulations in DNA sequencing data. They propose that in HeLa cells de novo structural aberrations arise frequently, and in most cases disappear from the rapidly proliferating population because they confer a proliferative disadvantage (Landry et al. 2013). Of note, kbNB142-70 treated Fucci2-HeLa cells also showed heterogeneity concerning the time of progression through S/G2/M phase. It would be interesting to investigate in future studies if this could be correlated to different level of PKD activity in these cells.

Kienzle et al could show that depletion of PKD resulted in a delay in S/G2/M phase and they proposed, that this delay was caused by a lack of Golgi fragmentation in G2 (Kienzle et al. 2013). To test this hypothesis, Brefeldin A, a Golgi dispersing agent, was used to rescue defects in Golgi fragmentation in G2 phase. Single cell analysis revealed that BFA treatment partially rescued the delay caused by inhibition of PKD (see Figure 26A). This indicates that PKD has a Golgi dependent function in control

of cell cycle progression as well as a potential Golgi independent function explaining the residual delay in cells treated with BFA. In an initial experiment, PKD inhibited Fucci2-HeLa cells showed several diminished phosphorylation sites, when using a phospho-PKD substrates antibody, compared to control cells (data not shown). To further investigate the pathway PKD controls in a Golgi independent manner a stable-isotope-labeling-by-amino-acids-in-cell-culture (SILAC) approach would aid in identifying downstream targets of PKD.

4.5.   Quantitative analysis and modelling of heterogeneous populations and signalling pathways

To further clarify if the Golgi independent function of PKD is also dependent on members of the MAPK pathway, similar to the Golgi dependent pathway, pPKD, pMEK and pERK levels were quantified during release from an aphidicolin block in Fucci2-HeLa cells. Unfortunately, single cell analysis was not possible because the antibodies were not suitable for immunofluorescence analysis. Instead quantitative Western blot analysis using the odyssey system was performed.

In this work PKD activity was measured by the detection of activation loop phosphorylation as well as substrate phosphorylation. However, regulation of PKD activity is not trivial as several phosphorylation sites are identified. The phosphorylation of the activation loop at PKD1-Ser738/Ser742 is thought to be essential for full kinase activity as in alanine mutants of these two serine residues PKD activity is inhibited (Iglesias & Rozengurt 1998). However, some groups reasoned that Ser742 phosphorylation plays little to no role in the control of PKD1 activity, because WT-PKD1 and the PKD1-S910A mutant (which is not phosphorylated at Ser742) display similar high levels of activity toward target substrates. An explanation provided is that activation loop serine to alanine substitutions can have dual effects namely to prevent phosphorylation and to remove hydroxyl groups that may engage in structurally important electrostatic interactions (reviewed in (Steinberg 2012). Moreover PKC-independent mechanisms are not associated with, and do not require activation loop phosphorylation in bone morphogenetic protein 2-treated MC3T3-E1 osteoblast-like cells, reactive oxygen species-activated endothelial cells, and UVB-treated keratinocytes (reviewed in (Steinberg 2012). It is likely that activation loop phosphorylation or

autophosphorylation at Ser916 are not an optimal readout for PKD activity in cell cycle progression as Tandon and colleagues also could not show an effect on PKDs activation loop phosphorylation or autophosphorylation but a strong PKD dependent effect on proliferation in prostate cancer cells treated with a PKD specific inhibitor (Tandon et al. 2013). LaValle and colleagues showed that only very high concentrations of kbNB142-70 exert an effect on activation loop phosphorylation in prostate cancer cells. Moreover, this effect was only visible in PMA treated cells (C. LaValle et al. 2010). This may explain why we did not find alterations in activation loop phosphorylation states between control cells and PKD inhibitor treated cells.

The quantitative analysis of MEK and ERK phosphorylation revealed an increase and subsequent decrease in pMEK and pERK levels approximately 1 hour after aphidicolin release in control cells. Fritsche-Guenther and colleagues could show that one single feedback from ERK to RAF accounts for the observed robustness of the steady-state phosphorylation of ERK (Fritsche-Guenther et al. 2011). Indeed, analysis of pMEK and pERK levels in synchronized HeLa cells revealed that UO126 blocks the phosphorylation of ERK, thereby attenuating the negative feedback on RAF kinase. Thus, pMEK level increased because of the higher RAF Kinase activity (see Figure 31A & B). The accurate quantification of feedback loops thus requires the quantitative analysis of signalling proteins and not a qualitative detection of protein activity. Sorafenib showed a slight inhibition of both pMEK and pERK levels and inhibited the initial increase 1 hour after release from aphidicolin block. Interestingly, inhibition of PKD by kbNB142-70 did not drastically alter the levels of pMEK and pERK. Therefore, it is unlikely that PKD signals through the MAPK pathway to induce progression through S/G2/M phase. This was also verified by mathematical modelling because the model, in which these assumptions were made, showed an excellent fit with the experimental data (see Figure 32) whereas models without feedback were clearly rejected.

Mathematical modelling is a powerful tool to verify biological hypothesis based on experimental outcomes. It is used on several organizational levels of biological systems, from the cell to whole ecosystems. Moreover, it is useful to correlate biological data gained by different methodical approaches. An advantage is the fact that it is possible to correlate population and single cell analysis. For example,

Bajikar and colleagues demonstrated, that single cell characteristics in gene expression could be deconvolved from stochastic-profiling data (Bajikar et al. 2014). Mathematic is also a growing prerequisite for interpreting complex biological data gained by novel techniques. An example is the use of mathematical modelling in medical imaging of computed tomography (Fetzer et al. 2006). Furthermore basic models of physical problems in patients as for example the blood flow are developed to help doctors identifying an optimal strategy for blood vessel surgery. Alnaes and colleagues modelled the complete circle of Willis to better understand the development and treatment of cerebral aneurysms in this region (Alnaes et al. 2007). Moreover, computational approaches to investigate the electromechanics of healthy and diseased hearts are becoming essential for the comprehensive understanding of cardiac function (reviewed in Vadakkumpadan et al. 2010).

Modelling cell cycle progression of heterogeneous cell population is more challenging because of the inert biological properties of each single cell. Cell-to-cell communication and spontaneous mutations have to be taken into account. Despite these challenges initial studies show that modelling of heterogeneous populations can provide insight into clinical relevant problems. Using a systems approach Schoeberl and colleagues built a computational model of the ErbB signaling network that describes the most effective ErbB ligands. This model identified ErbB3 as the key node in response to ligands that can bind either ErbB3 or EGFR. Consequently, they described MM-121, a human monoclonal antibody that halts the growth of tumor xenografts in mice, which promises to benefit patients with combinatorial, ligand-induced activation of the ErbB signaling network that are not effectively treated by current therapies (Schoeberl et al. 2009). Mumenthaler and colleagues demonstrated in a combined experimental and mathematical approach, that low-dose sequential combination strategies of several therapeutics may lead to tumor reduction and improved survival outcome for patients with T790M-mediated resistance (Mumenthaler et al. 2011). Similarly, modelling cell cycle progression in HeLa cells and correlating this model to the signal pathway model generated in this work may lead to the analysis of combinatorial treatment. Preliminary data showed a synergistic effect of the MEK inhibitor UO126 and the PKD inhibitor kbNB142-70 in delaying the progression through S/G2/M phase in Fucci2-HeLa cells. The impact of combinations of different inhibitors can thus be optimized with the help of the model and experimentally verified.

4.6. Conclusions and perspectives

In conclusion, difficulties during in vitro cultivation of hMSC were identified and the need to use animal models and transgenic mBMSCs was shown. Problems with cultivating primary mMSC were overcome by the generation of functional mMSC lines from wild-type and Fucci mice. With the help of Fucci-mBMSCs a function of PKD in cell cycle control was identified in mouse MSC. To further analyse PKD dependent functions in cell cycle control Fucci2-HeLa cells were used. Golgi-dependent and potential Golgi-independent functions of PKD during cell cycle progression were demonstrated by single cell analysis. Quantitative analysis revealed that PKD mostly acts independent of the RAF/MEK/ERK pathway during G2 phase. This was further verified by mathematical modelling. Further experiments in single cell analysis and more data on PKD activity are necessary to correlate the proliferation data and the signal pathway data.

Apart from the G2 phase, a potential role of PKD in mitosis was investigated. Indeed, kbNB142-70 treated cells were delayed in progression through mitosis compared to control cells. Notably, kbNB142-70 treated cells displayed insufficient cytokinesis. Here, the cofilin signaling pathway could be identified as a promising candidate regulating cytokinesis downstream of PKD. Detailed live cell imaging and quantification of actin dynamics in general and specifically in mitosis is needed to gain further insight in the potential role of PKD in late mitosis.

5. References

Albeck, J.G., Mills, G.B. & Brugge, J.S., 2013. Frequency-modulated pulses of ERK activity transmit quantitative proliferation signals. *Molecular cell*, 49(2), pp.249–261.

Allan, E.H. et al., 2003. Differentiation potential of a mouse bone marrow stromal cell line. *Journal of cellular biochemistry*, 90(1), pp.158–169.

Alnaes, M.S. et al., 2007. Computation of hemodynamics in the circle of Willis. *Stroke; a Journal of Cerebral Circulation*, 38(9), pp.2500–2505.

In 't Anker, P.S. et al., 2003. Nonexpanded primary lung and bone marrow-derived mesenchymal cells promote the engraftment of umbilical cord blood-derived CD34(+) cells in NOD/SCID mice. *Experimental Hematology*, 31(10), pp.881–889.

Arakawa, E. et al., 2000. A mouse bone marrow stromal cell line, TBR-B, shows inducible expression of smooth muscle-specific genes. *FEBS letters*, 481(2), pp.193–196.

Aubin, J.E. et al., 1995. Osteoblast and chondroblast differentiation. *Bone*, 17(2 Suppl), p.77S–83S.

Böhrnsen, F. et al., 2009. Murine mesenchymal progenitor cells from different tissues differentiated via mesenchymal microspheres into the mesodermal direction. *BMC Cell Biology*, 10(1), p.92.

Bain, J. et al., 2007. The selectivity of protein kinase inhibitors: a further update. *The Biochemical journal*, 408(3), pp.297–315.

Bajikar, S.S. et al., 2014. Parameterizing cell-to-cell regulatory heterogeneities via stochastic transcriptional profiles. *Proceedings of the National Academy of Sciences of the United States of America*, 111(5), pp.E626–635.

Barr, F.A. et al., 2001. Golgi matrix proteins interact with p24 cargo receptors and aid their efficient retention in the Golgi apparatus. *The Journal of cell biology*, 155(6), pp.885–891.

Barr, F.A. et al., 1997. GRASP65, a protein involved in the stacking of Golgi cisternae. *Cell*, 91(2), pp.253–262.

Bartholomew, A. et al., 2002. Mesenchymal stem cells suppress lymphocyte proliferation in vitro and prolong skin graft survival in vivo. *Experimental Hematology*, 30(1), pp.42–48.

Bellantuono, I., Aldahmash, A. & Kassem, M., 2009. Aging of marrow stromal (skeletal) stem cells and their contribution to age-related bone loss. *Biochimica et Biophysica Acta (BBA) - Molecular Basis of Disease*, 1792(4), pp.364–370.

Beltrami, A.P. et al., 2007. Multipotent cells can be generated in vitro from several adult human organs (heart, liver, and bone marrow). *Blood*, 110(9), pp.3438–3446.

Bernardo, M.E., Locatelli, F. & Fibbe, W.E., 2009. Mesenchymal Stromal Cells. *Annals of the New York Academy of Sciences*, 1176(1), pp.101–117.

Bianco, P. et al., 2001. Bone marrow stromal stem cells: nature, biology, and potential applications. *Stem cells*, 19(3), pp.180–192.

Bianco, P., Barker, R., et al., 2013. Regulation of stem cell therapies under attack in Europe: for whom the bell tolls. *The EMBO Journal*, 32(11), pp.1489–1495.

Bianco, P. et al., 1998. Reproduction of human fibrous dysplasia of bone in immunocompromised mice by transplanted mosaics of normal and Gsalpha-mutated skeletal progenitor cells. *The Journal of clinical investigation*, 101(8), pp.1737–1744.

Bianco, P., Cao, X., et al., 2013. The meaning, the sense and the significance: translating the science of mesenchymal stem cells into medicine. *Nature Medicine*, 19(1), pp.35–42.

Bianco, P., Robey, P.G. & Simmons, P.J., 2008. Mesenchymal stem cells: revisiting history, concepts, and assays. *Cell Stem Cell*, 2(4), pp.313–319.

Boregowda, S.V. et al., 2012. Atmospheric Oxygen Inhibits Growth and Differentiation of Marrow-Derived Mouse Mesenchymal Stem Cells via a p53-Dependent Mechanism: Implications for Long-Term Culture Expansion. *STEM CELLS*, 30(5), pp.975–987.

Boxall, S.A. & Jones, E., 2012. Markers for characterization of bone marrow multipotential stromal cells. *Stem cells international*, 2012, p.975871.

Capes-Davis, A. et al., 2010. Check your cultures! A list of cross-contaminated or misidentified cell lines. *International journal of cancer. Journal international du cancer*, 127(1), pp.1–8.

Caplan, A.I., 2007. Adult mesenchymal stem cells for tissue engineering versus regenerative medicine. *Journal of Cellular Physiology*, 213(2), pp.341–347.

Chambard, J.-C. et al., 2007. ERK implication in cell cycle regulation. *Biochimica et Biophysica Acta (BBA) - Molecular Cell Research*, 1773(8), pp.1299–1310.

Chan, C.K.F. et al., 2013. Clonal precursor of bone, cartilage, and hematopoietic niche stromal cells. *Proceedings of the National Academy of Sciences of the United States of America*, 110(31), pp.12643–12648.

Chan, C.K.F. et al., 2009. Endochondral ossification is required for haematopoietic stem-cell niche formation. *Nature*, 457(7228), pp.490–494.

Chen, M.-Y. et al., 2009. Endothelial differentiation of Wharton's jelly–derived mesenchymal stem cells in comparison with bone marrow–derived mesenchymal stem cells. *Experimental Hematology*, 37(5), pp.629–640.

Cheng, H. et al., 2010. Replicative senescence of human bone marrow and umbilical cord derived mesenchymal stem cells and their differentiation to adipocytes and osteoblasts. *Molecular Biology Reports*, 38(8), pp.5161–5168.

Colanzi, A. et al., 2007. The Golgi mitotic checkpoint is controlled by BARS-dependent fission of the Golgi ribbon into separate stacks in G2. *The EMBO journal*, 26(10), pp.2465–2476.

Colanzi, A. & Sütterlin, C., 2013. Signaling at the Golgi during mitosis. *Methods in cell biology*, 118, pp.383–400.

Corda, D. et al., 2012. Golgi complex fragmentation in G2/M transition: An organelle-based cell-cycle checkpoint. *IUBMB life*, 64(8), pp.661–670.

Czondor, K. et al., 2009. Protein Kinase D Controls the Integrity of Golgi Apparatus and the Maintenance of Dendritic Arborization in Hippocampal Neurons. *Molecular Biology of the Cell*, 20(7), pp.2108–2120.

Dennis, J.E. et al., 1999. A quadripotential mesenchymal progenitor cell isolated from the marrow of an adult mouse. *Journal of Bone and Mineral Research*, 14(5), pp.700–709.

Diduch, D.R. et al., 1993. Two cell lines from bone marrow that differ in terms of collagen synthesis, osteogenic characteristics, and matrix mineralization. *The Journal of bone and joint surgery. American volume*, 75(1), pp.92–105.

Dominici, M. et al., 2006. Minimal criteria for defining multipotent mesenchymal stromal cells. The International Society for Cellular Therapy position statement. *Cytotherapy*, 8(4), pp.315–317.

Eilken, H.M., Nishikawa, S.-I. & Schroeder, T., 2009. Continuous single-cell imaging of blood generation from haemogenic endothelium. *Nature*, 457(7231), pp.896–900.

Eiseler, T. et al., 2009. Protein kinase D1 regulates cofilin-mediated F-actin reorganization and cell motility through slingshot. *Nature Cell Biology*, 11(5), pp.545–556.

Ellwanger, K. & Hausser, A., 2013. Physiological functions of protein kinase D in vivo. *IUBMB life*, 65(2), pp.98–107.

Feinstein, T.N. & Linstedt, A.D., 2008. GRASP55 regulates Golgi ribbon formation. *Molecular biology of the cell*, 19(7), pp.2696–2707.

Feinstein, T.N. & Linstedt, A.D., 2007. Mitogen-activated protein kinase kinase 1-dependent Golgi unlinking occurs in G2 phase and promotes the G2/M cell cycle transition. *Molecular biology of the cell*, 18(2), pp.594–604.

Fetzer, D.T., Green, C. & West, O.C., 2006. Mathematical modeling improves computed tomography diagnosis of traumatic aortic injury. *Academic Radiology*, 13(10), pp.1244–1253.

Fibbe, W.E., Dazzi, F. & LeBlanc, K., 2013. MSCs: science and trials. *Nature Medicine*, 19(7), pp.812–813.

Friedenstein, A.Y. & Lalykina, K.S., 1970. Lymphoid cell populations are competent systems for induced osteogenesis. *Calcified Tissue Research*, pp.Suppl:105–106.

Fritsche-Guenther, R. et al., 2011. Strong negative feedback from Erk to Raf confers robustness to MAPK signalling. *Molecular Systems Biology*, 7. Available at: http://msb.embopress.org/cgi/doi/10.1038/msb.2011.27 [Accessed January 21, 2014].

Fu, J. et al., 2007. Roles of Aurora kinases in mitosis and tumorigenesis. *Molecular cancer research: MCR*, 5(1), pp.1–10.

Fuchs, Y.F. et al., 2009. A Golgi PKD Activity Reporter Reveals a Crucial Role of PKD in Nocodazole-Induced Golgi Dispersal. *Traffic*, 10(7), pp.858–867.

Fujiwara, T. et al., 1988. Brefeldin A causes disassembly of the Golgi complex and accumulation of secretory proteins in the endoplasmic reticulum. *The Journal of biological chemistry*, 263(34), pp.18545–18552.

Giel-Moloney, M. et al., 2007. Ubiquitous and uniform in vivo fluorescence in ROSA26-EGFP BAC transgenic mice. *Genesis (New York, N.Y.: 2000)*, 45(2), pp.83–89.

H. Akaike, 1973. Information theory and an extension of the maximum likelihood principle. *Proceedings of the 2nd International Symposium on Information Theory*, pp.1:267–281.

Hahn, W.C. & Weinberg, R.A., 2002. Modelling the molecular circuitry of cancer. *Nature reviews. Cancer*, 2(5), pp.331–341.

Hartwell, L.H. & Weinert, T.A., 1989. Checkpoints: controls that ensure the order of cell cycle events. *Science (New York, N.Y.)*, 246(4930), pp.629–634.

Harvey, D.M. & Levine, A.J., 1991. p53 alteration is a common event in the spontaneous immortalization of primary BALB/c murine embryo fibroblasts. *Genes & development*, 5(12B), pp.2375–2385.

Hausser, A. et al., 2005. Protein kinase D regulates vesicular transport by phosphorylating and activating phosphatidylinositol-4 kinase IIIbeta at the Golgi complex. *Nature Cell Biology*, 7(9), pp.880–886.

Hollinger, J.O. & Kleinschmidt, J.C., 1990. The critical size defect as an experimental model to test bone repair materials. *The Journal of craniofacial surgery*, 1(1), pp.60–68.

Hornsby, P.J., 2003. Replicative senescence of human and mouse cells in culture: significance for aging research. *Mechanisms of ageing and development*, 124(8-9), pp.853–855.

Horwitz, E.M. et al., 2002. Isolated allogeneic bone marrow-derived mesenchymal cells engraft and stimulate growth in children with osteogenesis imperfecta: Implications for cell therapy of bone. *Proceedings of the National Academy of Sciences of the United States of America*, 99(13), pp.8932–8937.

Horwitz, E.M. et al., 1999. Transplantability and therapeutic effects of bone marrow-derived mesenchymal cells in children with osteogenesis imperfecta. *Nature Medicine*, 5(3), pp.309–313.

Hsiao, F.S.. et al., 2010. Isolation of therapeutically functional mouse bone marrow mesenchymal stem cells within 3 h by an effective single-step plastic-adherent method. *Cell Proliferation*, 43(3), pp.235–248.

Hudak, C.S. & Sul, H.S., 2013. Pref-1, a gatekeeper of adipogenesis. *Frontiers in endocrinology*, 4, p.79.

Iglesias, T. & Rozengurt, E., 1998. Protein kinase D activation by mutations within its pleckstrin homology domain. *The Journal of biological chemistry*, 273(1), pp.410–416.

Imoto, Y. et al., 2011. The cell cycle, including the mitotic cycle and organelle division cycles, as revealed by cytological observations. *Journal of electron microscopy*, 60 Suppl 1, pp.S117–136.

Itahana, K., Itahana, Y. & Dimri, G.P., 2013. Colorimetric detection of senescence-associated β galactosidase. *Methods in molecular biology (Clifton, N.J.)*, 965, pp.143–156.

Jadali, A. & Ghazizadeh, S., 2010. Protein Kinase D Is Implicated in the Reversible Commitment to Differentiation in Primary Cultures of Mouse Keratinocytes. *Journal of Biological Chemistry*, 285(30), pp.23387–23397.

Javazon, E.H., Beggs, K.J. & Flake, A.W., 2004. Mesenchymal stem cells: paradoxes of passaging. *Experimental hematology*, 32(5), pp.414–425.

Jiang, Y. et al., 2002. Multipotent progenitor cells can be isolated from postnatal murine bone marrow, muscle, and brain. *Experimental Hematology*, 30(8), pp.896–904.

Jones, E. & Yang, X., 2011. Mesenchymal stem cells and bone regeneration: Current status. *Injury*, 42(6), pp.562–568.

Josse, C. et al., 2010. Systematic chromosomal aberrations found in murine bone marrow-derived mesenchymal stem cells. *Stem Cells and Development*, 19(8), pp.1167–1173.

Juffroy, O. et al., 2009. Subcutaneous graft of D1 mouse mesenchymal stem cells leads to the formation of a bone-like structure. *Differentiation*, 78(4), pp.223–231.

Kaji, N., 2003. Cell Cycle-associated Changes in Slingshot Phosphatase Activity and Roles in Cytokinesis in Animal Cells. *Journal of Biological Chemistry*, 278(35), pp.33450–33455.

Karsenty, G., 2008. Transcriptional control of skeletogenesis. *Annual review of genomics and human genetics*, 9, pp.183–196.

Kern, S. et al., 2006. Comparative Analysis of Mesenchymal Stem Cells from Bone Marrow, Umbilical Cord Blood, or Adipose Tissue. *Stem Cells*, 24(5), pp.1294–1301.

Kienzle, C. et al., 2013. PKD controls mitotic Golgi complex fragmentation through a Raf–MEK1 pathway. *Molecular biology of the cell*, 24(3), pp.222–233.

Kleinschmidt, J.C. et al., 1993. A multiphase system bone implant for regenerating the calvaria. *Plastic and reconstructive surgery*, 91(4), pp.581–588.

Kon, E. et al., 2000. Autologous bone marrow stromal cells loaded onto porous hydroxyapatite ceramic accelerate bone repair in critical-size defects of sheep long bones. *Journal of biomedical materials research*, 49(3), pp.328–337.

Krebsbach, P.H. et al., 1997. Bone formation in vivo: comparison of osteogenesis by transplanted mouse and human marrow stromal fibroblasts. *Transplantation*, 63(8), pp.1059–1069.

Krebsbach, P.H. et al., 1998. Repair of craniotomy defects using bone marrow stromal cells. *Transplantation*, 66(10), pp.1272–1278.

Krishnappa, V., Boregowda, S.V. & Phinney, D.G., 2013. The peculiar biology of mouse mesenchymal stromal cells—oxygen is the key. *Cytotherapy*, 15(5), pp.536–541.

Kumar, S. & Ponnazhagan, S., 2012. Mobilization of bone marrow mesenchymal stem cells in vivo augments bone healing in a mouse model of segmental bone defect. *Bone*, 50(4), pp.1012–1018.

Kunter, U. et al., 2006. Transplanted mesenchymal stem cells accelerate glomerular healing in experimental glomerulonephritis. *Journal of the American Society of Nephrology: JASN*, 17(8), pp.2202–2212.

Kurz, D.J. et al., 2004. Chronic oxidative stress compromises telomere integrity and accelerates the onset of senescence in human endothelial cells. *Journal of Cell Science*, 117(Pt 11), pp.2417–2426.

Kuznetsov, S. & Gehron Robey, P., 1996. Species differences in growth requirements for bone marrow stromal fibroblast colony formation In vitro. *Calcified tissue international*, 59(4), pp.265–270.

Kuznetsov, S.A. et al., 1997. Single-colony derived strains of human marrow stromal fibroblasts form bone after transplantation in vivo. *Journal of bone and mineral research: the official journal of the American Society for Bone and Mineral Research*, 12(9), pp.1335–1347.

Landry, J.J.M. et al., 2013. The genomic and transcriptomic landscape of a HeLa cell line. *G3 (Bethesda, Md.)*, 3(8), pp.1213–1224.

Latzinic, N V., Sidorowich, S U. & Friedenstein, A J., 1979. Formation of hemopoietic territories by heterotopic trans- plantation of bone marrow cell suspensions. *Exp Hematol 1979; 7, suppl: 6, p. 26.*

LaValle, C. et al., 2010. Novel protein kinase D inhibitors cause potent arrest in prostate cancer cell growth and motility. *BMC chemical biology*, 10(1), p.5.

LaValle, C.R. et al., 2010. Protein kinase D as a potential new target for cancer therapy. *Biochimica et biophysica acta*, 1806(2), pp.183–192.

Lee, R.H. et al., 2006. Multipotent stromal cells from human marrow home to and promote repair of pancreatic islets and renal glomeruli in diabetic NOD/scid mice. *Proceedings of the National Academy of Sciences of the United States of America*, 103(46), pp.17438–17443.

Liu, H. et al., 2009. A subpopulation of mesenchymal stromal cells with high osteogenic potential. *Journal of cellular and molecular medicine*, 13(8B), pp.2436–2447.

Ma, H.T. & Poon, R.Y.C., 2011. Synchronization of HeLa cells. *Methods in molecular biology (Clifton, N.J.)*, 761, pp.151–161.

Marcacci, M. et al., 1999. Reconstruction of extensive long-bone defects in sheep using porous hydroxyapatite sponges. *Calcified tissue international*, 64(1), pp.83–90.

Martinez, C. et al., 2007. Human bone marrow mesenchymal stromal cells express the neural ganglioside GD2: a novel surface marker for the identification of MSCs. *Blood*, 109(10), pp.4245–4248.

Méndez-Ferrer, S. et al., 2010. Mesenchymal and haematopoietic stem cells form a unique bone marrow niche. *Nature*, 466(7308), pp.829–834.

Mielgo, A. et al., 2011. A MEK-independent role for CRAF in mitosis and tumor progression. *Nature Medicine*, 17(12), pp.1641–1645.

De la Morena, M.T. & Gatti, R.A., 2011. A History of Bone Marrow Transplantation. *Hematology/Oncology Clinics of North America*, 25(1), pp.1–15.

Morgan, D.O., 1995. Principles of CDK regulation. *Nature*, 374(6518), pp.131–134.

Morikawa, S. et al., 2009. Prospective identification, isolation, and systemic transplantation of multipotent mesenchymal stem cells in murine bone marrow. *The Journal of Experimental Medicine*, 206(11), pp.2483–2496.

Mumenthaler, S.M. et al., 2011. Evolutionary modeling of combination treatment strategies to overcome resistance to tyrosine kinase inhibitors in non-small cell lung cancer. *Molecular Pharmaceutics*, 8(6), pp.2069–2079.

Nauta, A.J. et al., 2006. Donor-derived mesenchymal stem cells are immunogenic in an allogeneic host and stimulate donor graft rejection in a nonmyeloablative setting. *Blood*, 108(6), pp.2114–2120.

Negishi, Y. et al., 2000. Multipotency of a bone marrow stromal cell line, TBR31-2, established from ts-SV40 T antigen gene transgenic mice. *Biochemical and biophysical research communications*, 268(2), pp.450–455.

Noort, W.A. et al., 2002. Mesenchymal stem cells promote engraftment of human umbilical cord blood-derived CD34(+) cells in NOD/SCID mice. *Experimental Hematology*, 30(8), pp.870–878.

Novák, B., Sible, J.C. & Tyson, J.J., 2003. Checkpoints in the cell cycle. *eLS*. Available at: http://onlinelibrary.wiley.com/doi/10.1038/npg.els.0001355/full [Accessed March 13, 2014].

Okabe, M. et al., 1997. "Green mice" as a source of ubiquitous green cells. *FEBS letters*, 407(3), pp.313–319.

Oki, T. et al., 2014. A novel cell-cycle-indicator, mVenus-p27K–, identifies quiescent cells and visualizes G0–G1 transition. *Scientific Reports*, 4. Available at: http://www.nature.com/doifinder/10.1038/srep04012 [Accessed May 21, 2014].

Olayioye, M.A., Barisic, S. & Hausser, A., 2013. Multi-level control of actin dynamics by protein kinase D. *Cellular Signalling*, 25(9), pp.1739–1747.

Ortiz, L.A. et al., 2007. Interleukin 1 receptor antagonist mediates the antiinflammatory and antifibrotic effect of mesenchymal stem cells during lung injury. *Proceedings of the National Academy of Sciences of the United States of America*, 104(26), pp.11002–11007.

Owen, M. & Friedenstein, A.J., 1988. Stromal stem cells: marrow-derived osteogenic precursors. *Ciba Foundation Symposium*, 136, pp.42–60.

Papazyan, R. et al., 2008. Protein kinase D isozymes activation and localization during mitosis. *Experimental Cell Research*, 314(16), pp.3057–3068.

Park, D. et al., 2012. Endogenous bone marrow MSCs are dynamic, fate-restricted participants in bone maintenance and regeneration. *Cell stem cell*, 10(3), pp.259–272.

Parrinello, S. et al., 2003. Oxygen sensitivity severely limits the replicative lifespan of murine fibroblasts. *Nature cell biology*, 5(8), pp.741–747.

Pauklin, S. & Vallier, L., 2013. The cell-cycle state of stem cells determines cell fate propensity. *Cell*, 155(1), pp.135–147.

Pedrali-Noy, G. et al., 1980. Synchronization of HeLa cell cultures by inhibition of DNA polymerase alpha with aphidicolin. *Nucleic Acids Research*, 8(2), pp.377–387.

Peister, A. et al., 2004. Adult stem cells from bone marrow (MSCs) isolated from different strains of inbred mice vary in surface epitopes, rates of proliferation, and differentiation potential. *Blood*, 103(5), p.1662.

Peterburs, P. et al., 2009. Protein kinase D regulates cell migration by direct phosphorylation of the cofilin phosphatase slingshot 1 like. *Cancer research*, 69(14), pp.5634–5638.

Phillips, J.A. et al., 2012. Advances in Single-cell Tracking of Mesenchymal Stem Cells (MSCs) During Musculoskeletal Regeneration. *The orthopaedic journal at Harvard Medical School*, 14, pp.22–28.

Phinney, D.G., 2012. Functional heterogeneity of mesenchymal stem cells: Implications for cell therapy. *Journal of Cellular Biochemistry*, 113(9), pp.2806–2812.

Phinney, D.G. et al., 2013. MSCs: science and trials. *Nature Medicine*, 19(7), pp.812–812.

Phinney, D.G. et al., 1999. Plastic adherent stromal cells from the bone marrow of commonly used strains of inbred mice: variations in yield, growth, and differentiation. *Journal of cellular biochemistry*, 72(4), pp.570–585.

Pittenger, M.F., 2013. MSCs: science and trials. *Nature Medicine*, 19(7), pp.811–811.

Preisinger, C. et al., 2005. Plk1 docking to GRASP65 phosphorylated by Cdk1 suggests a mechanism for Golgi checkpoint signalling. *The EMBO journal*, 24(4), pp.753–765.

Prouty, S.M. et al., 1993. A cell culture model system for genetic analyses of the cell cycle by targeted homologous recombination. *Oncogene*, 8(4), pp.899–907.

Rasini, V. et al., 2013. Mesenchymal stromal/stem cells markers in the human bone marrow. *Cytotherapy*, 15(3), pp.292–306.

Ravin, R. et al., 2008. Potency and fate specification in CNS stem cell populations in vitro. *Cell stem cell*, 3(6), pp.670–680.

Rosen, E.D. et al., 1999. PPAR gamma is required for the differentiation of adipose tissue in vivo and in vitro. *Molecular cell*, 4(4), pp.611–617.

Rosen, E.D. et al., 2000. Transcriptional regulation of adipogenesis. *Genes & development*, 14(11), pp.1293–1307.

Rosen, E.D. & Spiegelman, B.M., 2000. Molecular regulation of adipogenesis. *Annual review of cell and developmental biology*, 16, pp.145–171.

Rozengurt, E. et al., 1995. Protein kinase D (PKD): a novel target for diacylglycerol and phorbol esters. *Mutation research*, 333(1-2), pp.153–160.

Rozengurt, E., 2011. Protein Kinase D Signaling: Multiple Biological Functions in Health and Disease. *Physiology*, 26(1), pp.23–33.

Rozengurt, E., Rey, O. & Waldron, R.T., 2005. Protein kinase D signaling. *The Journal of biological chemistry*, 280(14), pp.13205–13208.

Sacchetti, B. et al., 2007. Self-Renewing Osteoprogenitors in Bone Marrow Sinusoids Can Organize a Hematopoietic Microenvironment. *Cell*, 131(2), pp.324–336.

Sakaue-Sawano, A. et al., 2011. Drug-induced cell cycle modulation leading to cell-cycle arrest, nuclear mis-segregation, or endoreplication. *BMC cell biology*, 12(1), p.2.

Sakaue-Sawano, A. et al., 2008. Visualizing spatiotemporal dynamics of multicellular cell-cycle progression. *Cell*, 132(3), pp.487–498.

Sato, M. et al., 1998. Transcriptional regulation of osteopontin gene in vivo by PEBP2alphaA/CBFA1 and ETS1 in the skeletal tissues. *Oncogene*, 17(12), pp.1517–1525.

Satomura, K. et al., 2000. Osteogenic imprinting upstream of marrow stromal cell differentiation. *Journal of cellular biochemistry*, 78(3), pp.391–403.

SCHERER, W.F., SYVERTON, J.T. & GEY, G.O., 1953. Studies on the propagation in vitro of poliomyelitis viruses. IV. Viral multiplication in a stable strain of human malignant epithelial cells (strain HeLa) derived from an epidermoid carcinoma of the cervix. *The Journal of experimental medicine*, 97(5), pp.695–710.

Schieker, M. et al., 2007. Human mesenchymal stem cells at the single-cell level: simultaneous seven-colour immunofluorescence. *Journal of anatomy*, 210(5), pp.592–599.

Schoeberl, B. et al., 2009. Therapeutically targeting ErbB3: a key node in ligand-induced activation of the ErbB receptor-PI3K axis. *Science Signaling*, 2(77), p.ra31.

Schwarz, G., 1978. Estimating the Dimension of a Model. *The Annals of Statistics*, 6(2), pp.461–464.

Shaul, Y.D. et al., 2009. Specific phosphorylation and activation of ERK1c by MEK1b: a unique route in the ERK cascade. *Genes & Development*, 23(15), pp.1779–1790.

Sinnett-Smith, J. et al., 2009. Protein kinase D mediates mitogenic signaling by Gq-coupled receptors through protein kinase C-independent regulation of activation loop Ser744 and Ser748 phosphorylation. *The Journal of biological chemistry*, 284(20), pp.13434–13445.

Sinnett-Smith, J. et al., 2004. Protein kinase D potentiates DNA synthesis induced by Gq-coupled receptors by increasing the duration of ERK signaling in swiss 3T3 cells. *The Journal of biological chemistry*, 279(16), pp.16883–16893.

Skloot, R., 2010. *The immortal life of Henrietta Lacks*, New York: Crown Publishers.

Soleimani, M. & Nadri, S., 2009. A protocol for isolation and culture of mesenchymal stem cells from mouse bone marrow. *Nature Protocols*, 4(1), pp.102–106.

Steinberg, S.F., 2012. Regulation of Protein Kinase D1 Activity. *Molecular Pharmacology*, 81(3), pp.284–291.

Sütterlin, C. et al., 2002. Fragmentation and dispersal of the pericentriolar Golgi complex is required for entry into mitosis in mammalian cells. *Cell*, 109(3), pp.359–369.

Takeshita, S., Arai, S. & Kudo, A., 2001. Identification and characterization of mouse bone marrow stromal cell lines immortalized by temperature-sensitive SV40 T antigen: supportive activity for osteoclast differentiation. *Bone*, 29(3), pp.236–241.

Tandon, M. et al., 2013. New pyrazolopyrimidine inhibitors of protein kinase d as potent anticancer agents for prostate cancer cells. *PloS one*, 8(9), p.e75601.

Tare, R.S. et al., 2010. Skeletal stem cells and bone regeneration: translational strategies from bench to clinic. *Proceedings of the Institution of Mechanical Engineers. Part H, Journal of engineering in medicine*, 224(12), pp.1455–1470.

Tasso, R. et al., 2013. In vivo implanted bone marrow-derived mesenchymal stem cells trigger a cascade of cellular events leading to the formation of an ectopic bone regenerative niche. *Stem cells and development*, 22(24), pp.3178–3191.

Uccelli, A., Pistoia, V. & Moretta, L., 2007. Mesenchymal stem cells: a new strategy for immunosuppression? *Trends in immunology*, 28(5), pp.219–226.

Vadakkumpadan, F. et al., 2010. Image-based models of cardiac structure in health and disease. *Wiley Interdisciplinary Reviews. Systems Biology and Medicine*, 2(4), pp.489–506.

Vassilev, L.T., 2006. Cell cycle synchronization at the G2/M phase border by reversible inhibition of CDK1. *Cell Cycle (Georgetown, Tex.)*, 5(22), pp.2555–2556.

Wang, Y. et al., 2003. A direct role for GRASP65 as a mitotically regulated Golgi stacking factor. *The EMBO journal*, 22(13), pp.3279–3290.

Wilhelm, S.M. et al., 2004. BAY 43-9006 exhibits broad spectrum oral antitumor activity and targets the RAF/MEK/ERK pathway and receptor tyrosine kinases involved in tumor progression and angiogenesis. *Cancer research*, 64(19), pp.7099–7109.

Wilson, A. et al., 2010. Age-related molecular genetic changes of murine bone marrow mesenchymal stem cells. *BMC Genomics*, 11, p.229.

Wu, M. et al., 2007. Imaging hematopoietic precursor division in real time. *Cell stem cell*, 1(5), pp.541–554.

Xu, J. et al., 2009. Neural ganglioside GD2 identifies a subpopulation of mesenchymal stem cells in umbilical cord. *Cellular physiology and biochemistry: international journal of experimental cellular physiology, biochemistry, and pharmacology*, 23(4-6), pp.415–424.

Xu, S. et al., 2010. An improved harvest and in vitro expansion protocol for murine bone marrow-derived mesenchymal stem cells. *Journal of Biomedicine & Biotechnology*, 2010, p.105940.

Yan, Y. et al., 2005. BRCA1-mediated G2/M cell cycle arrest requires ERK1/2 kinase activation. *Oncogene*, 24(20), pp.3285–3296.

Yañez, R. et al., 2006. Adipose tissue-derived mesenchymal stem cells have in vivo immunosuppressive properties applicable for the control of the graft-versus-host disease. *Stem Cells (Dayton, Ohio)*, 24(11), pp.2582–2591.

Zindy, F. et al., 1998. Myc signaling via the ARF tumor suppressor regulates p53-dependent apoptosis and immortalization. *Genes & development*, 12(15), pp.2424–2433.

6. Supplements

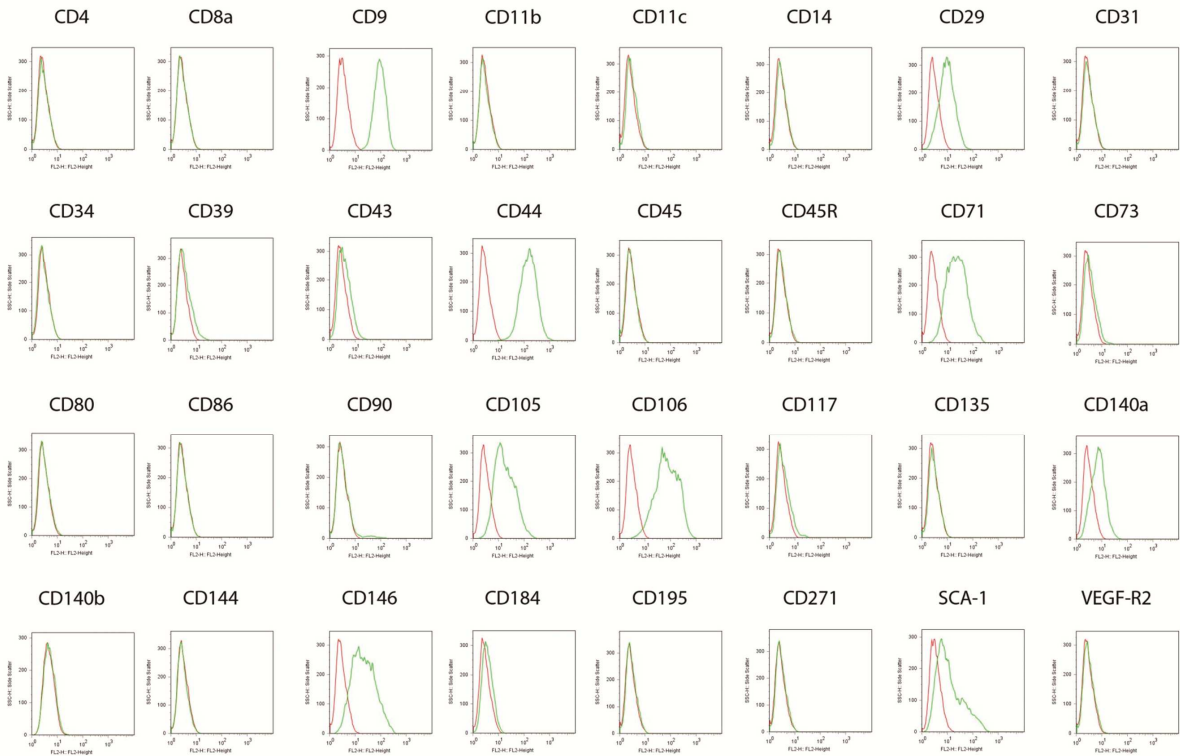## 6.1.   Flow cytometry analysis hMSC

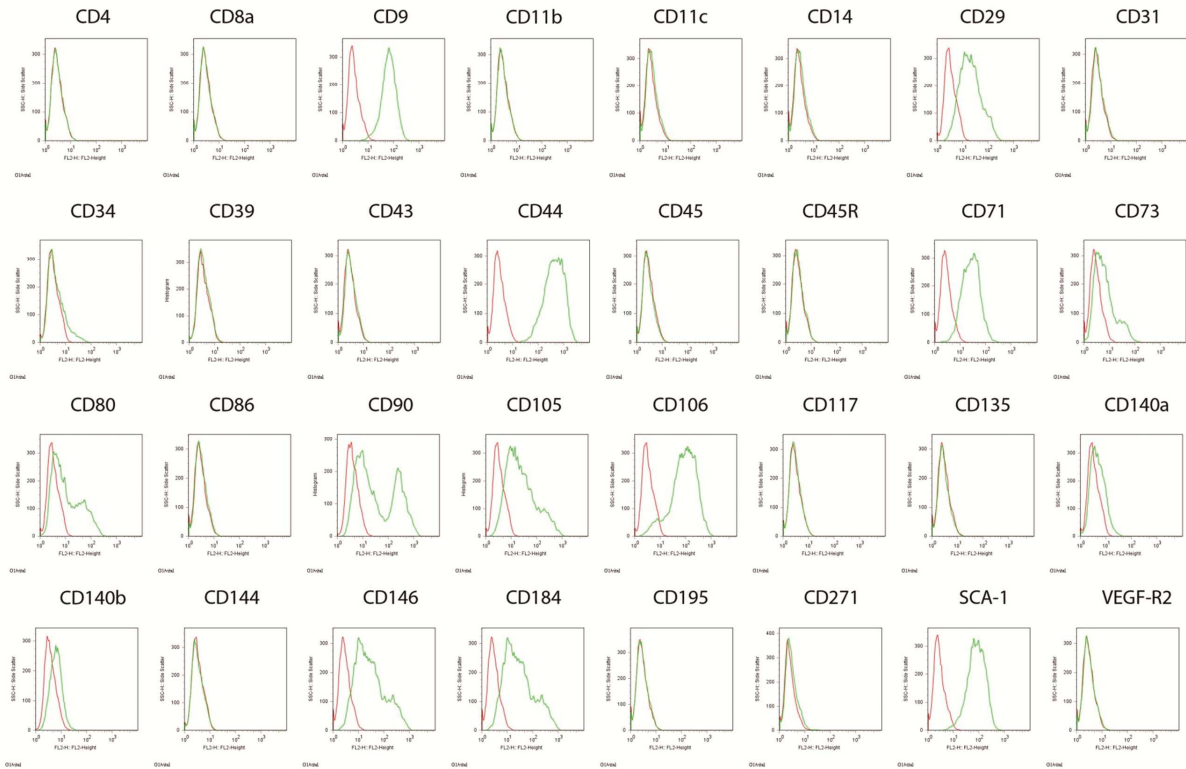UC162

UC163

UC165

D6

D7

D8

6.2. Flow cytometry analysis mBMSC

M7

CD4 CD8a CD9 CD11b CD11c CD14 CD29 CD31

CD34 CD39 CD43 CD44 CD45 CD45R CD71 CD73

CD80 CD86 CD90 CD105 CD106 CD117 CD135 CD140a
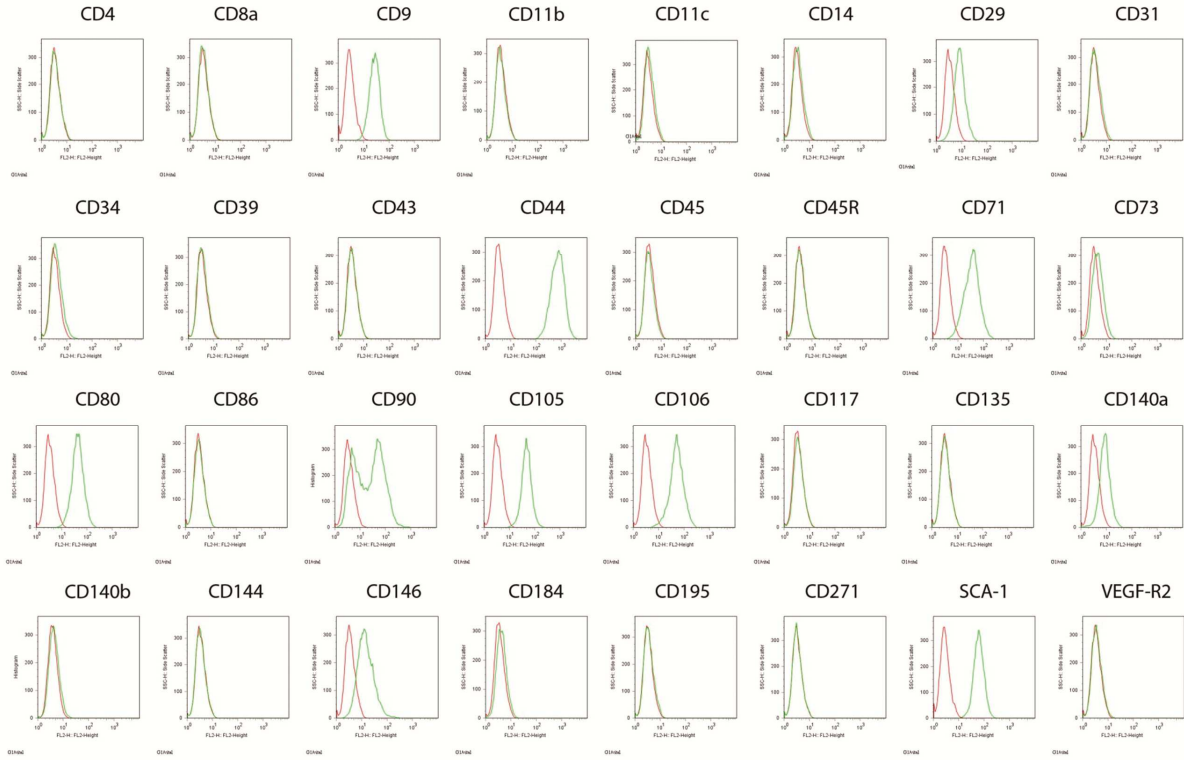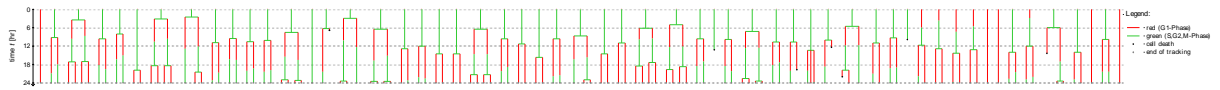
CD140b CD144 CD146 CD184 CD195 CD271 SCA-1 VEGF-R2

6.3. Tracking Data Fucci2-HeLa

Acknowledgements

First of all I would like to express my sincere thanks to Dr Angelika Hausser for her excellent supervision! She always found the right balance between independent working and guidance. Our discussions were very productive and spot on and she always motivated and encouraged me in my ideas. Finally I want to thank her for carefully revising my publication and this manuscript. Furthermore I thank Prof Klaus Pfizenmaier for the opportunity to perform this research at the IZI and for being the reviewer of this thesis. I would also like to thank Prof Peter Scheurich for sorting the HeLa-Liveact cells and for being co-reviewer of this thesis.

Thanks to the BMBF for funding parts of this interesting project.

I would like to thank my colleagues from the Hausser Lab for the pleasant working atmosphere. Special thanks Dr Kornelia Ellwanger and Dr Sandra Barisic, the two post docs in my laboratory, who were always open for questions, specifically I want to thank Dr Kornelia Ellwanger for isolating the Fucci-MEFs. Many thanks to Dr. Georg Siegel for his constant support with characterizing BMSC and performing the flow cytometry analysis of MSC. Thank you, Jan Hansmann for the good collaboration during the Systec project. I would also like to thank Benedetto Sacchetti for performing the M2 in-vivo experiment. Thanks to Helena Schnell for her excellent work during the time of her bachelor thesis. She was involved in the generation of the data concerning the Fucci BMSCs. I would like to say a big thank you to Dr Krisztian Tarnok and Dr Stephan Eisler for teaching me a lot about life cell imaging and working with the microscope in general. Thank you, Matthias Lorenzen for the great collaboration in generating the Fucci analysis software. Moreover I wish to express my gratitude to Dr Jan Hasenauer for the inspiring collaboration and discussions and helpful hints for the modeling part of this manuscript.

I am very grateful that I had the opportunity to work in such an interesting interdisciplinary project, where I had the chance to gain so much knowledge in different areas of research.

Last but not least I want to thank my friends and family for always being supportive and much else; however I prefer to tell them in person.

CV

Curriculum vitae

Persönliche Daten

Name: Sebastian Räth
Adresse: Schwarenbergstrasse 157
                         70184 Stuttgart
Email Adresse: sebastian.raeth@gmail.com

Geburtsdatum: 28. März 1985
Geburtsort: Kempten
Staatsangehörigkeit: deutsch
Familienstand: ledig

Studium

05/2011 - aktuell   Promotion am Institut für Zellbiologie und Immunologie der Universität Stuttgart

10/2004 – 04/2011   Studium der Technischen Biologie an der Universität Stuttgart
Abschluss: Diplom Biologe t.o.

Berufserfahrung

10/2010 – 12/2010   Wissenschaftlicher Angestellter am Institut für Zellbiologie und Immunologie der Universität Stuttgart

04/2007 – 09/2007   Praktikum bei Andiatec GmbH in Stuttgart, Kornwestheim.

Schulbildung

09/1995 – 06/2004   Gymnasium in Immenstadt im Allgäu
Abschluss: Abitur

09/1991 – 08/1995   Grundschule in Stein im Allgäu

Publikationen

Stem Cells and Development   Sebastian Raeth, Benedetto Sacchetti, Georg Siegel, Ulrike A. Mau-Holzmann, Jan Hansmann, Gabriele Vacun, Thomas G. Hauk, Klaus Pfizenmaier, and Angelika Hausser: **A Mouse Bone Marrow Stromal Cell Line with Skeletal Stem Cell Characteristics to Study Osteogenesis In Vitro and In Vivo.**

Journal of Biological Chemistry   Tan SX, Greetham D, Raeth S, Grant CM, Dawes IW, Perrone GG: **The thioredoxin-thioredoxin reductase system can function in vivo as an alternative system to reduce oxidized glutathione in Saccharomyces cerevisiae**.

Stuttgart, 28.06.2014